SPAWAR

Systems Center PACIFIC

TECHNICAL REPORT 3028
September 2016

Radio Frequency Performance Prediction in the North Sea

Analysis of the U.S.-NL
Phase 1 Campaign

Amalia Barrios
Ted Rogers
Rick Navarro
Dr. Earl Williams
SSC Pacific

Katherine Horgan
Victor Wiss
Stephanie Billingsley
Naval Surface Warfare Center

Dr. Robert Marshall
Mount Pleasant Meteorology

Dr. Vincent Van Leijen
Tjarda Wilbrink
Defense Materiel Organisation

Fok Bolderheij
Joris Derksen
Netherlands Defense Academy

Approved for public release.

SSC Pacific
San Diego, CA 92152-5001

**SSC Pacific
San Diego, California 92152-5001**

K. J. Rothenhaus, CAPT, USN
Commanding Officer

C. A. Keeney
Executive Director

ADMINISTRATIVE INFORMATION

The work described in this report was performed by the Atmospheric Propagation Branch (Code 55280) of the Networks Division (Code 55200), Space and Naval Warfare Systems Center Pacific (SSC Pacific), San Diego, CA; Naval Surface Warfare Center, Port Hueneme, CA; Mount Pleasant Bureau of Meteorology Mount Pleasant, Australia; Defense Material Organization, The Hague, Netherlands; and Netherlands Defense Academy, Naaldwijk, Netherlands. This cooperative effort was jointly funded by the Space and Naval Warfare Systems Command (SPAWAR) Program Executive Office C4I/Battlespace Awareness and Information Operations Program Office (PMW 120), the Office of the Secretary of Defense, and the Netherlands Ministry of Defense.

Released by
D. Tsintikidis, Head
Atmospheric Propagation Branch

Under authority of
P. Juarez, Head
Networks Division

The citation of trade names and names of names of manufacturers is not to be construed as official government endorsement or approval of commercial products or services referenced in this report.

Page Pelican case™ is a trademark of Pelican Products, Inc.
LORD MicroStrain 3DM-GX4-45™ is a trademark of Lord Sensing MicroStrain
Tektronix TEK-3408A spectrum analyzer is a registered trademark of Tektronix, Inc.
MATLAB® is a registered trademark of MathWorks®
Rohde & Schwartz FSW26 spectrum analyzer is a registered trademark of Rohde & Schwartz
Python™ is a registered trademark of Python Software Foundation
Vaisala DigiCORA SPS220 receiver is a software solution of Vaisala
ThermoWorks (electronic) thermometer by ThermoWorks
DigiCORA® software is a registered trademark of Vaisala
Rohde & Schwarz® spectrum analyzer is a registered trademark of Rohde & Schwarz
AI Page Tecom 201822 is a registered trademark of Tecom Industries Inc.
Ethernet is a registered trademark of Xerox.

SB

EXECUTIVE SUMMARY

This report presents a summary of the technical analysis of meteorological and radio-frequency (RF) propagation data collected during the Phase 1 field trial conducted as part of a joint U.S.-Netherlands (NL) project of the Coalition Warfare Program (CWP). The CWP effort is jointly funded by the U.S. (PEO C4I/PMW-120 and the Office of the Secretary of Defense (OSD)) and the Netherlands Ministry of Defense (MoD). The objective of the CWP effort is to enhance radar modeling to enable improved situational awareness of the detection capability of phased array radars, as affected by current meteorological and oceanographic (METOC) conditions.

ACRONYMS

AMSL	Above Mean Sea Level
AOI	Area of Interest
APAR	Advanced Phased Array Radar
APM	Advanced Propagation Model
AREPS	Advanced Refractive Effects Prediction System
ASL	Actual Sea Level
ASTD	Air-sea Temperature Difference
C2	Command and Control
CDF	Cumulative Distribution Function
COAMPS	Coupled Ocean/Atmospheric Mesoscale Prediction System
CWP	Coalition Warfare Program
DMO	Defense Materiel Organization
ECMWF	European Centre for Medium-Range Weather Forecasting
EDH	Evaporation Duct Height
ERP	Effective Radiated Power
EW	Electronic Warfare
FoV	Field of View
FRISC	Fast Raiding Interceptor and Special Forces Craft
GDAS	Global Data Assimilation System
HARMONIE - AROME	High Resolution Limited Area Model (HiRLAM) Aladin Research On Meso-scale Operational NWP In Euromed - Applications of Research to Operations at Mesoscale
IOP	Intensive Observation Period
KNMI	Royal Netherlands Meteorological Institute
LBTS	Land Based Test Site
METOC	Meteorology and Oceanographic
MoD	Ministry of Defense
MSL	Mean Sea Level
NAVSLaM	Navy Atmospheric Vertical Surface Layer Model
NCODA	Navy Coupled Ocean Data Assimilation
NLDA	Netherlands Defense Academy
NSWC DD	Naval Surface Warfare Center, Dahlgren Division
NWP	Numerical Weather Prediction
OSD	Office of the Secretary of Defense
PMW-120	Program Manager, Warfare - 120
RF	Radio Frequency
RMSE	root mean squared error
RNLN	Royal Netherlands Navy
RPM	Radio Propagation Model

RTM	Radar Threshold Model
SSC Pacific	Spae and Naval Warfare Systems Center, Pacific
TACMET	Tactical Meteorological Equipment
VRPBA	Vertical Refractivity Profile Blending Algorithm

CONTENTS

Figures

Tables

1. INTRODUCTION

Offensive and defensive operations require a valid and detailed understanding of how far and high a radar can detect targets in all directions. A nominal circular radius based on single-point meterological and oceanographic (METOC) measurements is insufficient, not only for open-ocean conditions, but primarily in littoral regions where refractive conditions vary much more drastically spatially and temporally.

Interoperability in electronic warfare (EW) is a key enabling capability for the U.S. military and its allies, particularly in the use of radars. Radar can be a highly effective tool for identifying the distance, direction, and height of targets and threats. However, its performance is not uniform; numerous factors cause its effectiveness to vary significantly by distance/direction/height at a given location and time. Among these factors, METOC parameters and phenomena are of particular interest, such as sea surface temperature, sea surface roughness, and atmospheric ducting. Radar propagation modeling (RPM) and radar threshold modeling (RTM) play an important role in our U.S. and coalition command and control (C2) by helping us understand the limits and blind spots of our radars' ability to detect adversaries, and conversely, of adversary radars' ability to detect us.

The Advanced Refractive Effects Prediction System (AREPS) is a U.S. Navy RPM/RTM tactical decision aid. It allows users to visualize a radar's performance at various distances, directions, and heights from a given location, under a given set of METOC conditions. The research conducted under this CWP is a collaboration between U.S. and Netherlands radar engineers and meteorologists, investigating radar modeling and visualization concepts, using the AREPS and an analogous system employed by the Royal Netherlands Navy (RNLN). The research involves laboratory analyses and information exchanges regarding U.S. and NL technical and algorithmic approaches to the RPM/RTM. Two data collection campaigns to aid in validation of the models are part of the research effort. This report describes the first campaign (Phase 1) and summarizes the data collected and analyzed.

This research effort includes participants from the Space and Naval Warfare System Center Pacific (SSC Pacific), Naval Surface Warfare Center, Dahlgren Division (NSWC DD), Defense Materiel Organisation (DMO), and the Netherlands Defense Academy (NLDA).

2. PHASE 1 EXPERIMENT

The main purpose for the Phase 1 experiment is to collect meteorological data and RF propagation data, specifically from a phased array radar to support the validation of the enhanced RTM.

Methods used to investigate the quality of performance predictions obtained include the following:

1. In-situ meteorological measurements only, consisting of upper air radiosonde observations and surface layer (bulk) measurements
2. Numerical weather prediction (NWP) forecasts obtained from the coupled ocean/atmospheric mesoscale prediction system (COAMPS) (Hodur, 1997), and the high resolution limited area model (HiRLAM) aladin research on meso-scale operational NWP in euromed–applications of research to operations at mesoscale (HARMONIE-AROME) (Seity et al., 2011)
3. Data assimilation provided by a combination of (a) and (b)

2.1 DATA COLLECTION PLAN

The Phase 1 experiment was conducted at the Land Based Test Site (LBTS) facility in Den Helder, The Netherlands, during 9–12 Sep 2014. The Salamander building at the LBTS offered a unique location as there are two primary radars installed on the building rooftop (L-band and X-Band). Their locations relative to each other are configured to be representative of sensor positions on board a RNLN frigate-class ship. The radar used during Phase 1 is the Advanced Phased Array Radar (APAR), which operates at a center frequency of 10 GHz (X-band). The APAR normally utilizes four phased array antenna "faces" on ship; however, the land-based APAR at the LBTS consists of one antenna face directed toward the North Sea for coastal surveillance. The antenna has a 90° field of view (FoV). The LBTS facility and Salamander building are shown in Figure 1.

Figure 1. LBTS facility. Salamander building is in the foreground, indicated by the yellow box. The APAR antenna is indicated by the red circle.

Two vessels were provided by the Royal Netherlands Navy (RNLN), a Fast Raiding Interceptor and Special Forces Craft (FRISC) and the Rotte tug. The FRISC was used as the primary "target" for the APAR, with RF receivers and meteorological equipment installed on board the Rotte tug. The daily concept of operations is illustrated in Figure 2 and is described in the remainder of this section.

Figure 2. Phase 1 concept of operations.

2.1.1 RF Measurements

Radar returns were collected and logged from the APAR as it tracked the FRISC outfitted with two corner reflectors, directed forward and aft, mounted 4.0 m above the waterline (Figure 3).

Figure 3. FRISC with fore and aft corner reflectors.

Parameters recorded during each event include the following:

- Sensor track ID (an enumeration by APAR)
- Radar cross section (RCS) (m^2, as assessed by the APAR)
- Calculated bearing (radians relative to true north)
- Calculated range (m)
- Calculated speed (m/s)
- Calculated course (radians relative to true north)
- Plot position x (m, relative to radar reference point)
- Plot position y (m, relative to radar reference point)
- Time of measurement relative (sec, since start of the event)

Positional data for the FRISC was also collected using a custom instrument assembly. Mounted in a small Pelican case™, a single-board computer initializes and queries a LORD MicroStrain 3DM-GX4-45™ Global Positioning System (GPS)-aided Inertial Navigation System (GPS-INS). At the maximum rate of 4 Hz, GPS position, altitude, heading, and Euler angles were recorded. The box was mounted at the bow of the FRISC, with a GPS patch antenna elevated on the existing forward gun mount (Figure 4).

Figure 4. Docked FRISC showing the GPS custom assembly Pelican case, indicated by the yellow circle, being removed from near its front location.

An S-band CW emitter (3.7 GHz) was located near the APAR antenna on the lower rooftop of the Salamander building, shown in Figure 5.
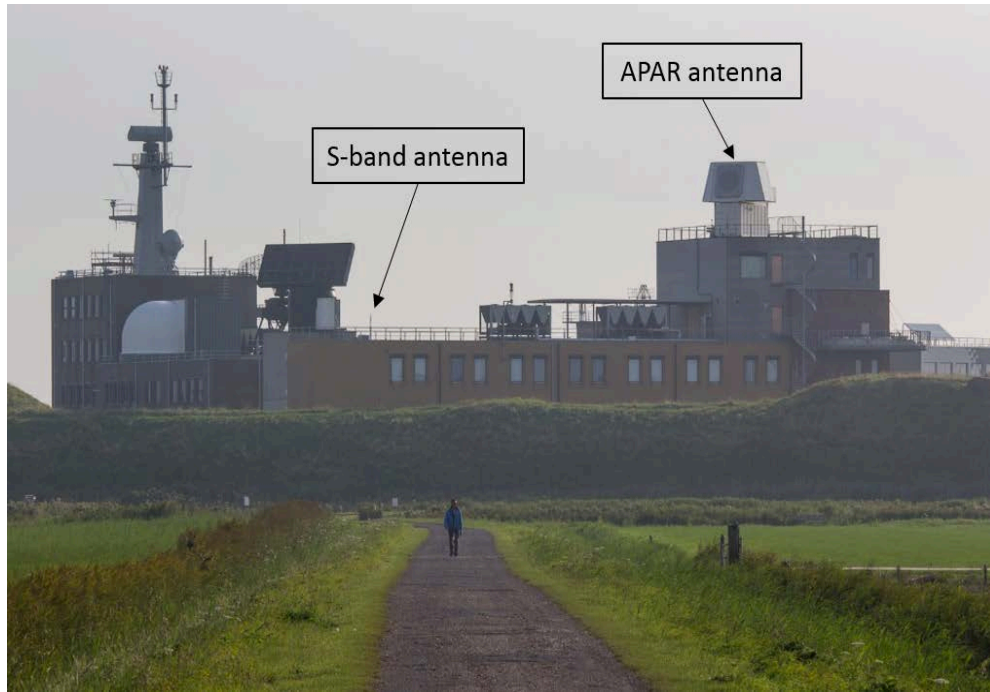
Figure 5. APAR and S-band antenna at the Salamander building.

The S-band transmitter and antenna, from the vantage point of the rooftop location, is shown in Figure 6, with the antenna pointed at an azimuth of 260°. It is apparent that a small portion of the propagation path is over land, which will be discussed in Section 5.4. An S-band emitter was employed for this trial to obtain a secondary means of determining an "effective" evaporation duct along the path using the RF inversion technique described in Rogers, Hattan, and Stapleton, 2000. The basic premise of this technique is that there is a unique correspondence, at S-band, between the evaporation duct height and the variability of propagation loss as a function of range for the same duct height. This allows the determination of a unique "effective" evaporation duct height, and subsequent vertical profile, by observation of the propagation loss as a function of range along the path. While the same inversion technique can be applied at X-band (APAR frequency), results here are highly ambiguous due to the multimodal propagation effects from the evaporation duct at this frequency and geometry, which is illustrated in Figure 7.

Propagation loss was computed based on neutral profiles (ASTD = 0.0) using 0-, 5-, 10-, 15-, and 20-m evaporation duct heights. Loss as a function of range is shown relative to the loss at mid-path for both S-band and X-band at the various evaporation duct heights. The shaded range interval roughly corresponds to the ranges at which RF propagation data were collected along the path during the Phase 1 trial. The ambiguity in the predicted loss at X-band are clearly seen.

Figure 6. S-band transmitter and antenna on the rooftop of the Salamander building.
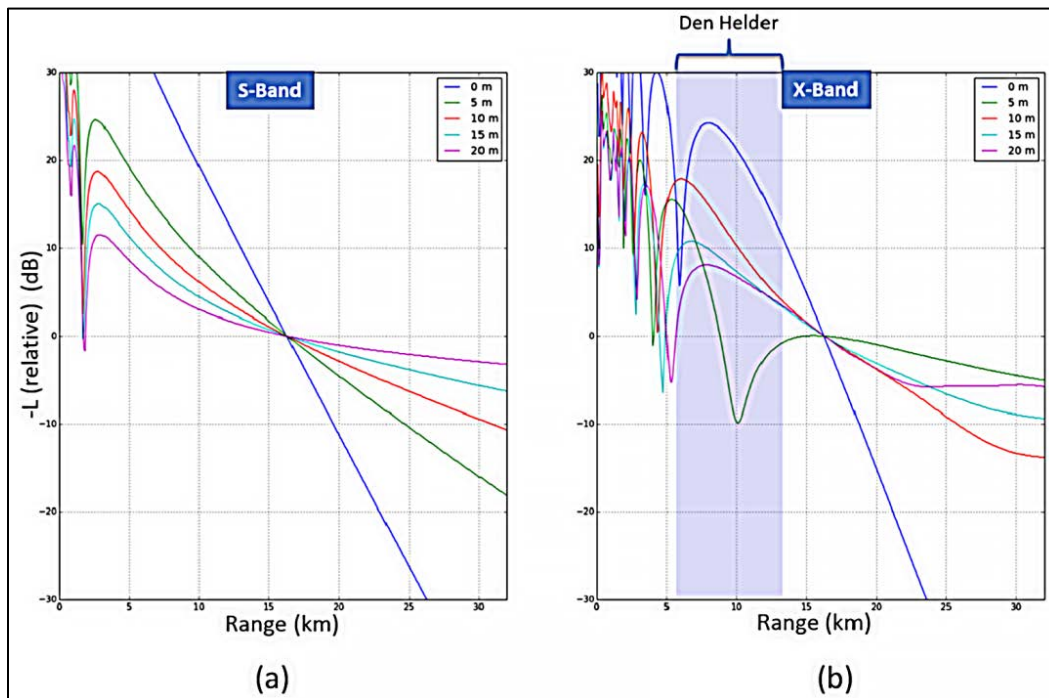
Figure 7. Propagation loss relative to the loss at mid-path for various neutral evaporation duct profiles at (a) S-band, and (b) X-band.

RF receive antennas were located on board the Rotte tug, mounted at 8.25 m above waterline, to record one-way S-band and X-band signals while the tug traversed outbound, as shown in Figure 8. S-Band signals were collected using a custom 2.4 to 3.4-GHz horn antenna connected using low-loss cables to a Tektronix TEK-3408A spectrum analyzer. MATLAB®-based control code operated on a laptop connected by a General Purpose Interface Bus (GPIB) cable. The setup, shown in Figure 9, measured and recorded signal power directly at approximately 1-min intervals throughout the day. The GPS system is the same as that used for collection of the FRISC position data.
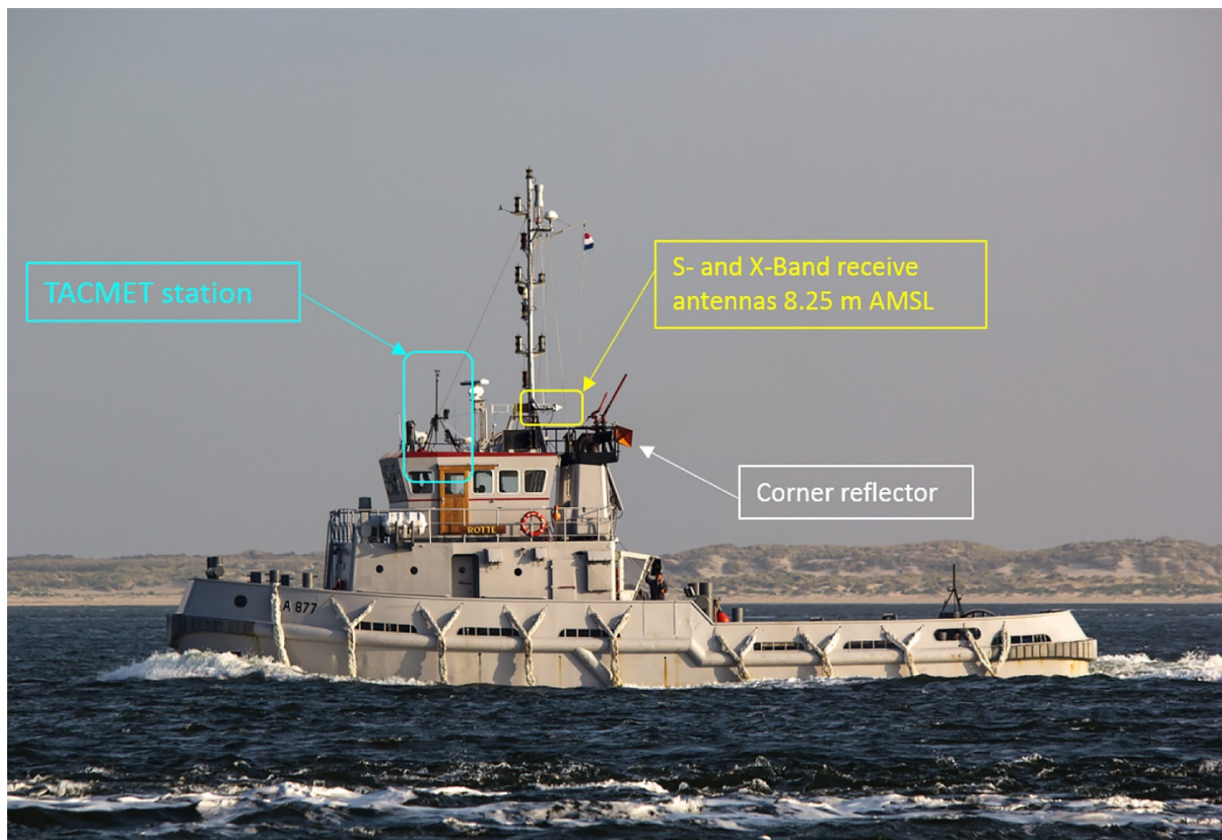
Figure 8. Rotte tug with RF receiver and TACMET station.

One-way X-band data collection used a custom log-periodic antenna connected directly to a Rohde&Schwartz® FSW26 spectrum analyzer using low-loss cables. The setup was controlled over gigabit Ethernet® by a laptop computer running custom Python™-based control software (Figure 10). The FSW with its frequency range of 2 Hz to 26.5 GHz allowed us to take and store 5 to 10-msec packets of raw IQ data each time a potential radar pulse was received. Due to the on board processing limits of the spectrum analyzer, we acquired only a few packets each minute. This data was evaluated in post-processing to determine average signal power and individual pulse characteristics and is described in Section 5.3.
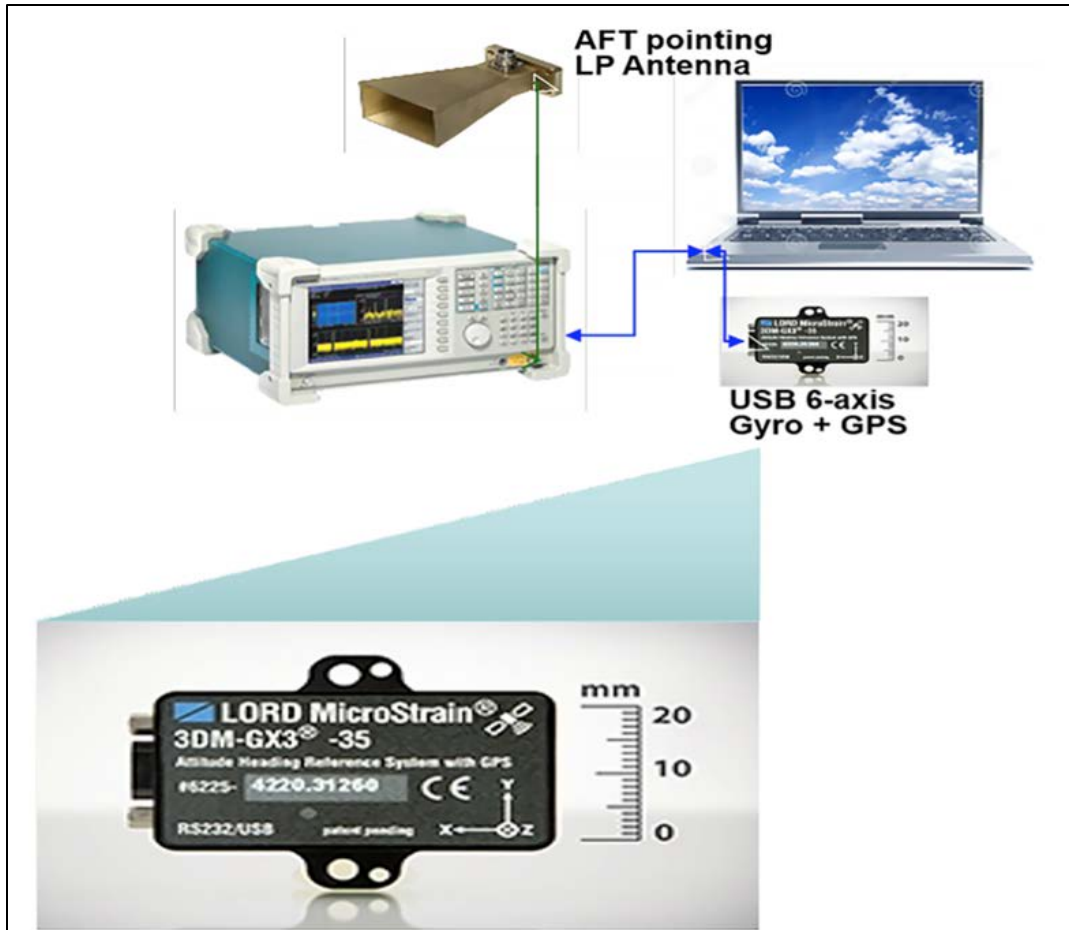
Figure 9. S-band CW receiver and GPS system.

The transmitter frequencies, heights, and locations are provided in Table 1 for use in calculating propagation loss. The transmitter height is converted to height above actual sea level (ASL) by taking into account the difference between mean sea level (MSL) and the tide height.

Table 1. Transmitter characteristics.

Parameter	APAR	S-band CW
Frequency (GHz)	10.0 (center)	3.7
Height AMSL (m)	~25	14.55
Location (latitude, longitude)	52.958^0 N, 4.736^0 E	Same

2.1.2 Meteorological Measurements

Surface observations were made from two Tactical Meteorological Equipment (TACMET) Weather Stations (MAWS201M), one located onshore near the LBTS and one located on the Rotte tug (Figure 8). Near-surface measurements include:

1. 2- and 10-min averages of wind speed (m/s).
2. 2- and 10-min averages of wind direction (degrees).
3. 1-min relative humidity (%).
4. 1-min air temperature (C).
5. Barometric pressure.

The sensor heights for each TACMET station are provided in Table 2.

Table 2. Sensor heights for the TACMET stations shore-side and on the Rotte tug.

Sensor	Shore (m) (AMSL)	Rotte tug (m) (ASL)
Air temperature	7.98	8.23
Humidity	7.98	8.23
Wind	9.93	9.49
Pressure	7.54	7.79

Figure 10 shows the connectivity configuration for the 10X-band pulse capture system.
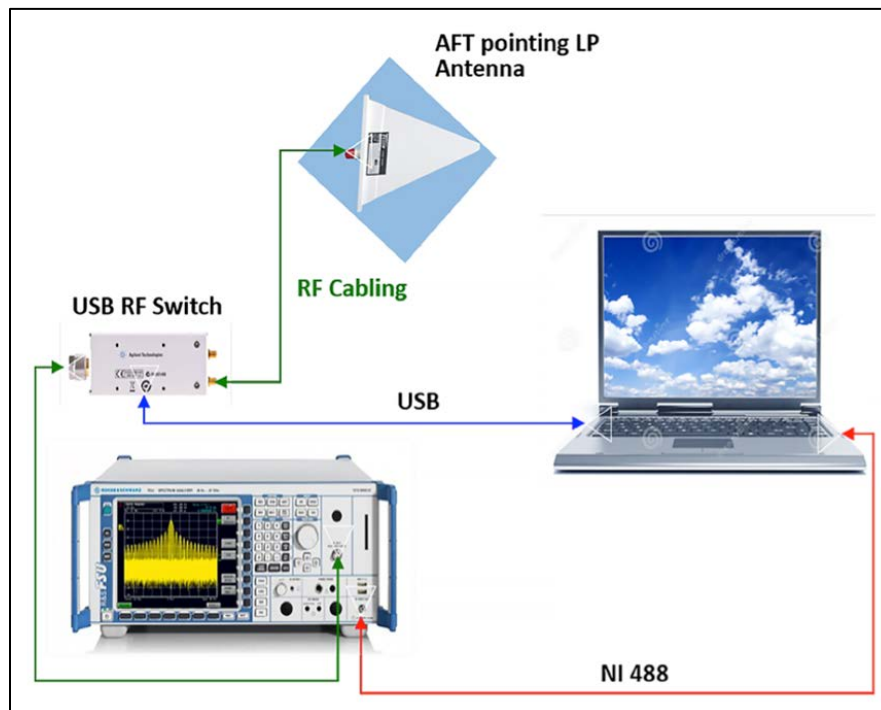
Figure 10. X-band pulse-capture system.

Note that the sensor heights for the onshore TACMET station include the height of the mound (6.24 m above waterline) on which the station was located (Figure 11).

Figure 11. Shore-site TACMET station and radiosonde launch site.

Upper air radiosonde measurements were also obtained from both locations: (1) near the shore-site TACMET station, and (2) from on board the Rotte tug, using a Vaisala DigiCORA SPS220 receiver system along with RS92SGP radiosondes. We employed a "slow-leak" technique developed by Naval Surface and Warfare Center (NSWC) Dahlgren Division (Horgan et al., 2014), where a syringe is inserted into the throat of the balloon and the plunger is removed before launch to allow the helium to slowly leak from the balloon (see Figure 12). This allows measurements of two vertical profiles, one on ascent and one on descent, where the more favorable profile is assumed to be that taken on descent as the ascent profile will most likely contain contaminated heat or cross wind effects from a boat launch station.
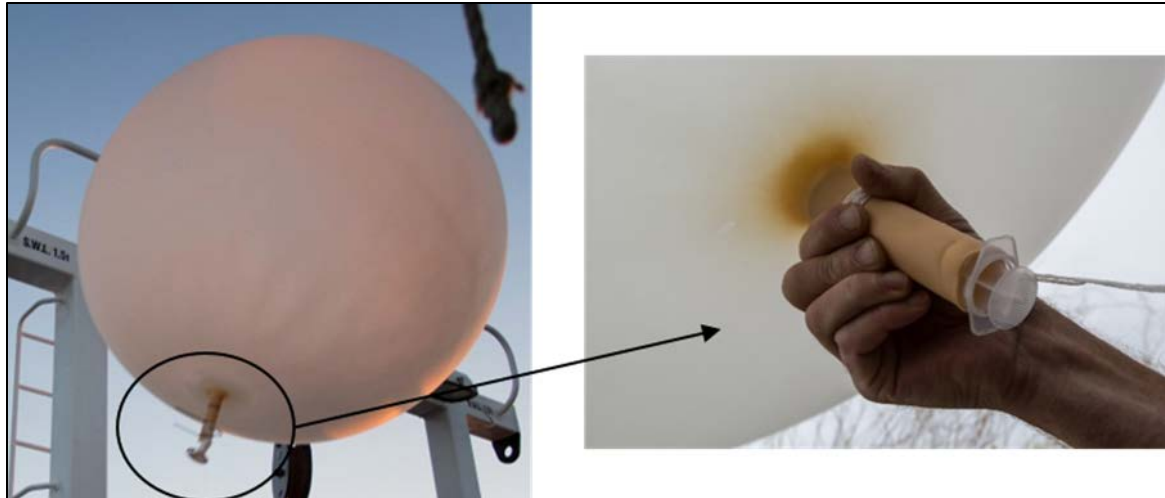
Figure 12. Balloon with syringe.

Several radiosondes were launched each day of the intensive observation period (IOP) during the morning and afternoon. Sea surface temperature was obtained from the Rotte tug using "bucket" temperature measurements and a thermistor. As indicated, the bucket temperatures were obtained by lowering a bucket over the side of the Rotte tug and filling it with water from no deeper than a few inches below the surface. A ThermoWorks (electronic) thermometer with ±0.2 °C accuracy was then used to take the temperature of the water in the bucket. This was performed at least twice at each sampling time to prevent operator error from contaminating the Sea Surface Temperature (SST) measurements. SST measurements were performed each time the Rotte tug slowed to facilitate balloon launches.

All meteorological measurements, both surface and upper air, collected during the IOP are shown in Table 3.

Table 3. Surface and upper air measurements collected.

Met Observations	Sep 9	Sep 10	Sep 11	Sep 12
Near-surface, TACMET	2- and 10-min. average of wind direction, wind speed; 1-min Rh% and pressure			
Number of radiosondes (RMTS)	5	5	11	4
Number of radiosondes (Tug)	6	6	11	4

2.1.3 Radiosonde Quality Assurance/Quality Control (QA/QC) Issues and Process to Rectify Data

The Quality Assurance/Quality Control (QA/QC) process began during the test event. During or immediately prior to launch, metadata were logged concerning system configuration, sensor performance, surface observations, and other considerations of the test environment. The metadata were logged via both electronic spreadsheet and paper notebook. The logs informed both on-site sounding system configuration adjustments as well as post-event QA/QC decisions. Logged metadata included sounding identifiers (launch time, serial number, and purpose), sensor ground check data, transmission frequency, balloon mass and helium fill, sea surface description, cloud coverage,

surface wind observations, operator names, and any operator comments. During each sounding, operators monitored and noted meteorological data to check for telemetry issues, sensor failures, adequate balloon ascent rates, and other sounding system data issues. Attempts to correct for such issues were performed and logged for subsequent launches. After each measurement, data from the sounding database file (*.db3db) was converted into a Vaisala standard form known as FLEDT.

At the conclusion of the field test, the FLEDT files were parsed and loaded into MATLAB®. An initial data issue was then handled programmatically. The issue occurred during times when the weather balloon rose too slowly at some height in the atmosphere. Low balloon ascent rates can cause spurious humidity and temperature readings due to insufficient sensor ventilation. For this reason, all data collected when the ascent rate was less than 2 m s-1 were reassigned to the missing value (i.e., "NaN").

Next, profiles of the following variables were plotted and visually inspected as a function of measurement height (z):

- Temperature
- Pressure
- Relative Humidity (RH)
- Horizontal range from launch site
- Geographic coordinates
- Horizontal wind speed and direction
- Ascent rate ($\Delta z/\Delta t$, discretely calculated)
- Potential temperature (calculated)
- Modified refractivity (calculated)

Some common data issues were then noted and flagged, as shown in Table 4.

Occasionally, RH profiles had quick increases up or down in humidity values, with little height increase. "These jumps are referenced as "sawtooth RH." Figure 13 shows a profile with the sawtooth RH issue. When the sawtooth RH issue is present, the analyst checks the FRAWPTU file to determine if the large switches in RH are due to sensor switching issues. The sonde's two RH sensors take turns making the RH measurements and occasionally there is a correlation in heights between the RH jumps occurring in the profiles with RH from the sensors switching and needing to acclimate once it is activated to take measurements. After viewing the raw data from the FRAWPTU file, we determined that all the sawtooth RH issues were valid measurements because the jumps in the profiles occurred at heights when the RH sensors were not switching.
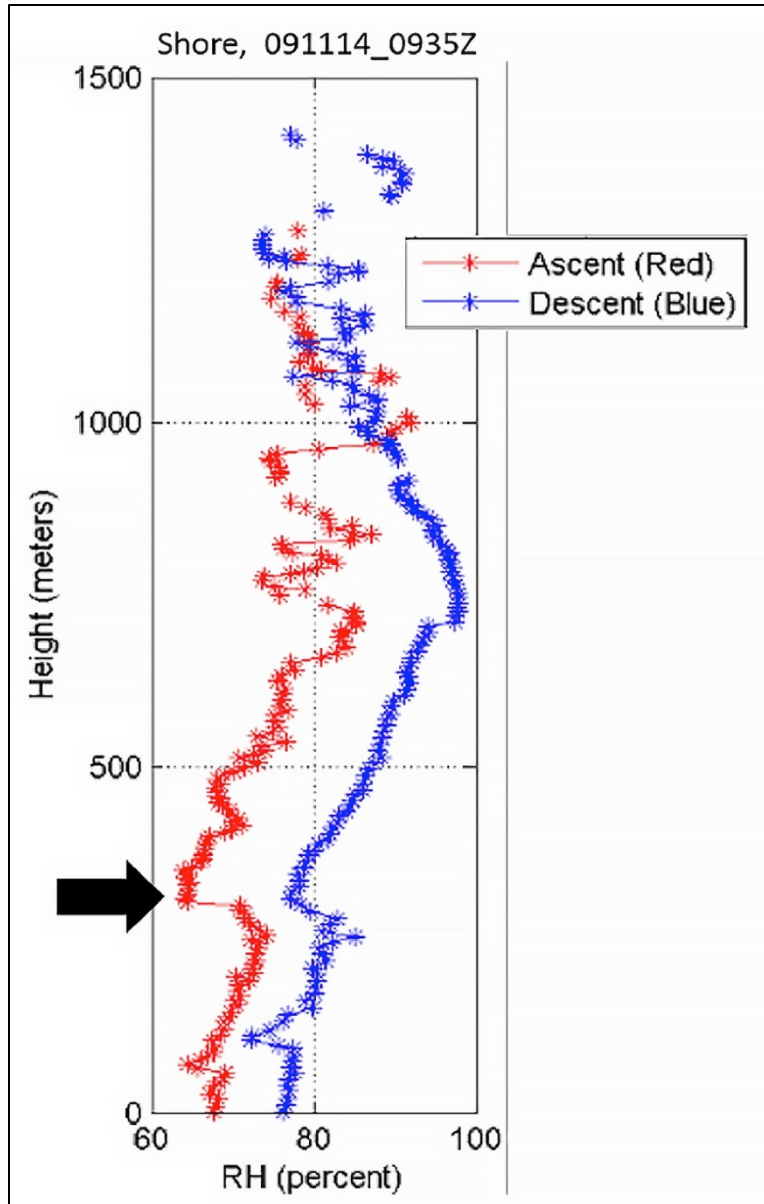
Figure 13. Profile displaying the sawtooth RH issue.

Some of the profiles had a Wind Speed Ramp Up issue, where the wind speed increases quickly with height. For these profiles, the flagged file's surface wind value was compared to the corresponding 15-sec TACMET data and the 5-min discretely averaged TACMET data. Figure 14 shows an example of Wind Speed Ramp Up. Wind Speed Ramp Up occurred for the Rotte tug. The QA/QC team did not think the wind speeds were accurate in the time immediately after launch due to unspooling issues; therefore, the team decided to remove the wind speed measurement values between the initial surface value and a height of 150 m from all of the ascending profiles. The initial surface wind speeds were kept. Wind speed values between the surface value and 150 m of the atmosphere are only available from the descending data.
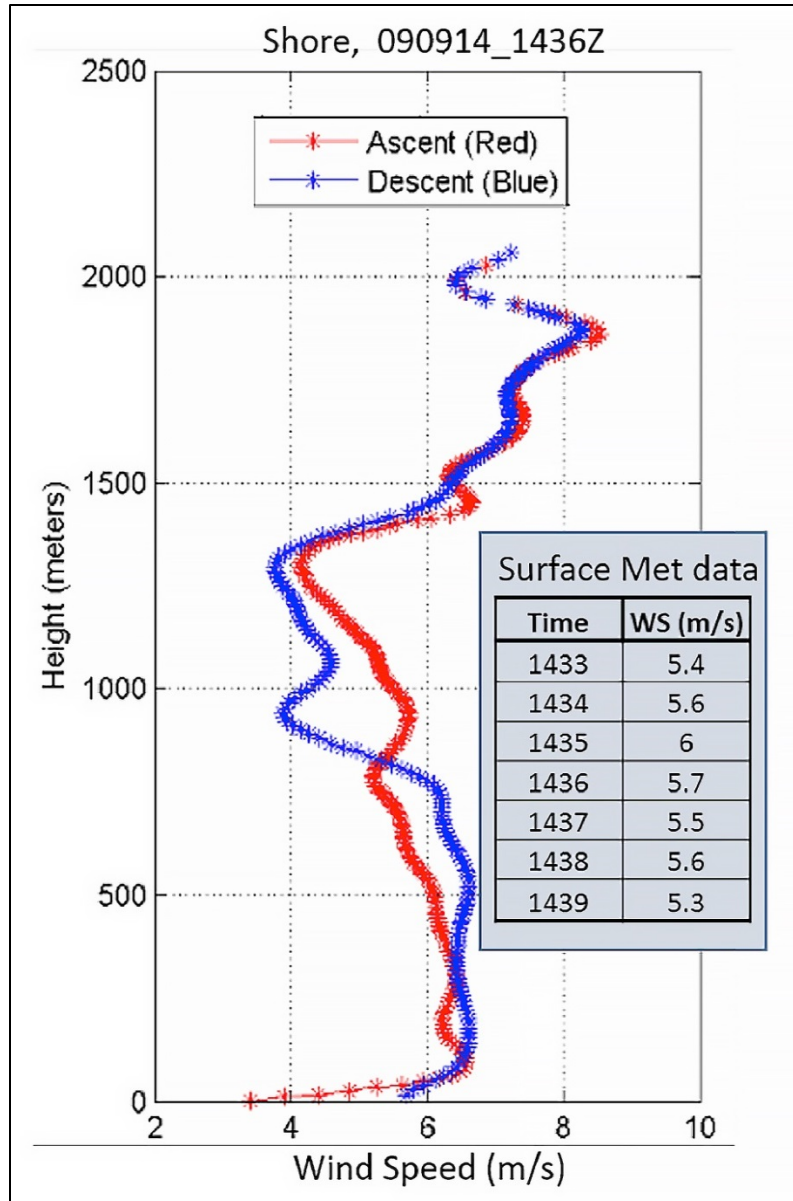
Figure 14. Wind Speed profile compared to the surface met wind speed data.

Some of the surface pressure values during the trial were lower than the software's standard input range; therefore, a higher pressure value was entered in the pressure field before launch, resulting in less than zero height values. Figure 15 shows a profile with a negative height value. After the field trial, the pressure input range was modified and resimulation with the correct surface pressure values eliminated the negative height values and calculated the correct height values.

h(m)
3
-5.53
-2.96
-6.65
-5.01
-5.93
-6.68
-5.98
-5.39
-4.45
-1.44
12.3
20.65
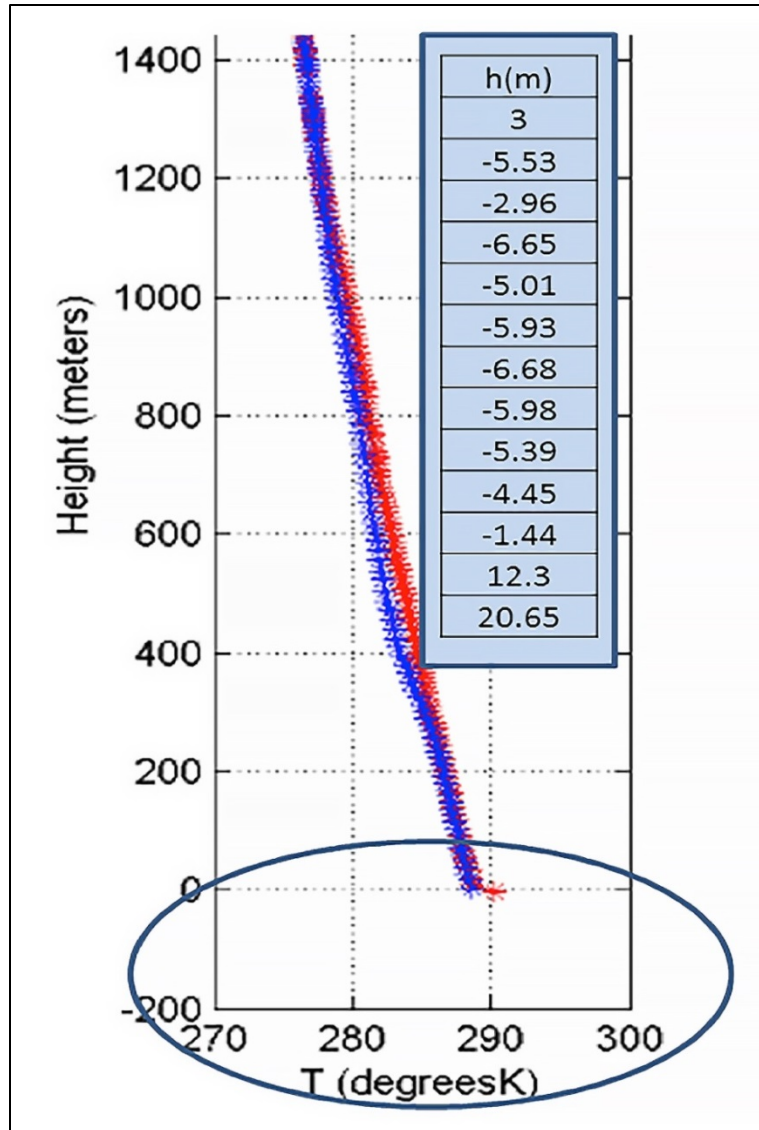
Figure 15. Example of negative height values due to incorrect pressure initialization.

After sondes were flagged by the criteria listed in Table 4, the analyst/group reviewed the profiles and determined if the surface point could be inaccurate. A spreadsheet was created to compare available data collected immediately prior to each flagged sonde launch by the TACMET station. The TACMET is shown in Figure 16. The time series of sonde measurements of pressure, temperature, and humidity were examined for the 10 to 30 secs when clear air was observed prior to launch. If the time series average prior to launch disagreed with the sounding surface observation, the time series average was used.

Table 4. QA/QC flags determined by visually inspecting sounding profiles.

QC Issue	Associated Data Issues
Partial or total loss of position/wind data	Telemetry failure
Sawtooth RH	Error in internal humidity sensor cycling
Wind speed ramp up	Pendulum effect of sonde as it stabilizes under the balloon
Pressure initialization limitation	Produces negative height values
Software in "research mode"	Greater than 100% relative humidity

Figure 16. TACMET measuring surface values at the shore station launch.

During the resimulation with the DigiCORA® software for surface pressures, any other necessary corrections for surface observations were input prior to resimulation. After resimulation, we then performed a QA/QC check for each resimulated sounding in the same way as the first version until agreement was reached that the data was valid.

The profile data had other issues that were corrected using MATLAB® scripts. While using Digicora's research mode, the software allows RH measurements to be greater than 100%. The standard mode of the software auto-corrects this output. Figure 17 shows an example profile of the RH greater than 100%. Fourteen sondes out of the total of 54 displayed this issue. The QA/QC MATLAB® code was used to limit the RH measurement to 100% to be consistent with typical Vaisala processing.
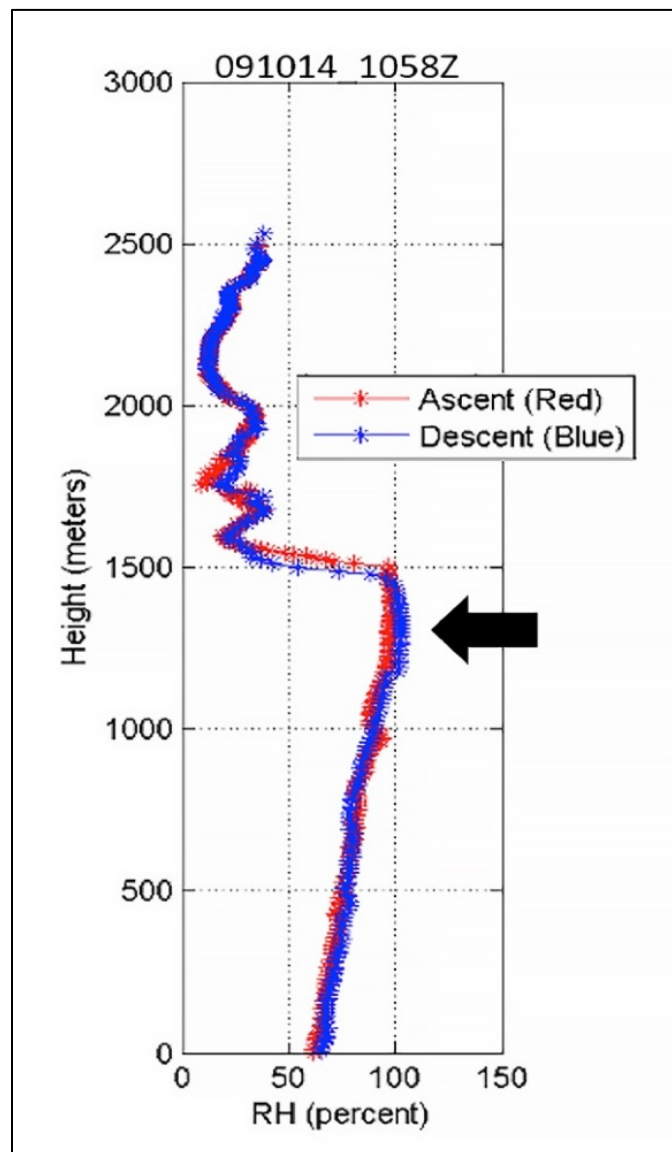
Figure 17. A profile displaying the greater than 100% RH issue.

17

For the shore radiosondes, the radiosondes were released on the top of a berm. Figure 18, Figure 19, and Figure 20 show the shore-site release location. The height of the berm and the person was not accounted for at the time of the test event. Therefore, MATLAB® code was used to add 7.74 m to the radiosonde initial height, 6.24 m height of dike, and 1.5 m height of a person.

Figure 18. The shore-site features.

Figure 19. Radiosonde release from on top of the berm.

Figure 20. Radiosonde release from on top of the berm.

The product of the review of collected data and processing through quality control algorithms thus provides a ground truth set of vertical soundings of the atmosphere taken on the Rotte tug and at the shore site. Each of the soundings now reflects the best measurement that could be made with the systems utilized while considering as many error sources as were known.

3. NUMERICAL WEATHER PREDICTION MODELS

As part of the overall RF propagation, analysis includes comparisons of RF predictions based on each country's NWP model forecasts. A brief description of each model is given provided in the following subsections.

3.1 COUPLED OCEAN ATMOSPHERE MESOSCALE PREDICTION SYSTEM (COAMPS)

COAMPS is the U.S. Navy's operational mesoscale NWP model in support of the fleet, run at Fleet Numerical Meteorological and Oceanographic Center. NSWCDD maintains a separate instance of COAMPS to support radar test and evaluation events for the acquisition community. During the Phase I trial, the NSWCDD team provided COAMPS forecasts. To maintain the required NWP delivery schedule, COAMPS was initialized every 12 hrs for a 36-hr forecast cycle. To minimize model differences, the COAMPS grid was set up on 60 vertical levels, with a horizontal resolution of roughly 2.5 km using a Lambert Conformal projection. The SST analyses used to initialize the ocean surface were provided from the Navy Coupled Ocean Data Assimilation (NCODA) system (Smith, Allard and Carrol, 2014). The COAMPS grid is shown in Figure 21.
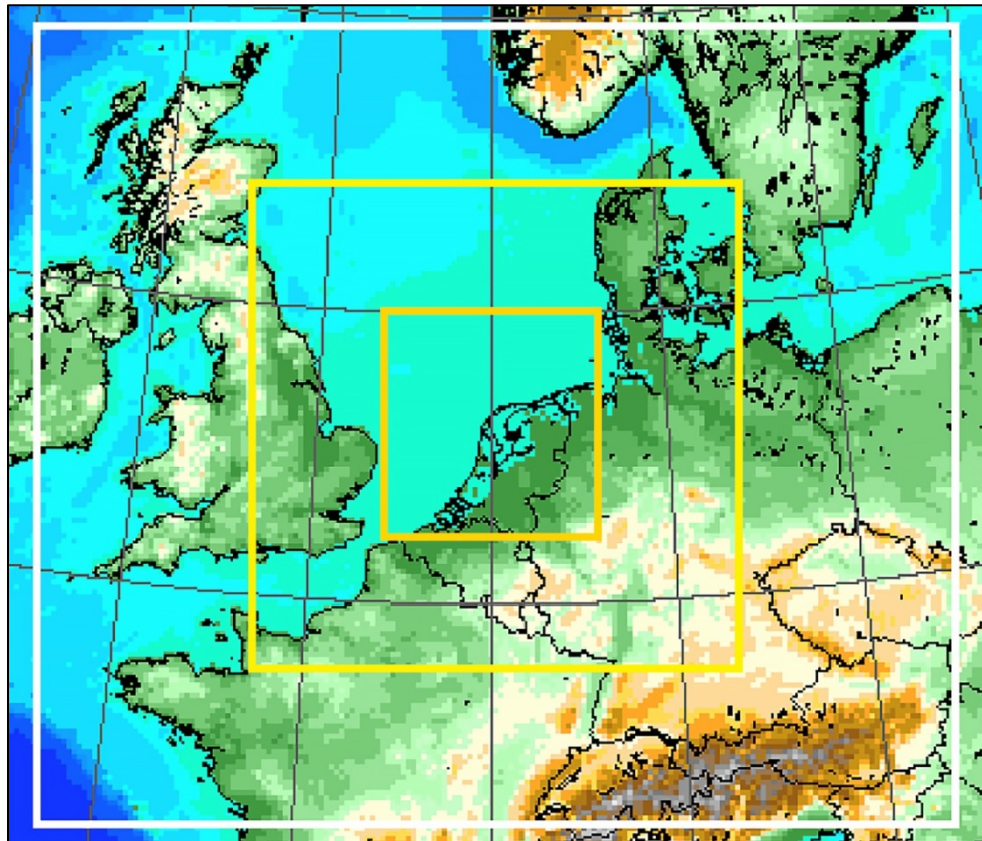
Figure 21. COAMPS grid used for the Phase 1 test.

3.2 HIGH-RESOLUTION LIMITED AREA MODEL (HIRLAM) ALADIN RESEARCH ON MESO-SCALE OPERATIONAL NWP IN EUROMED - APPLICATIONS OF RESEARCH TO OPERATIONS AT MESOSCALE (HARMONIE-AROME)

The NL-based NWP model forecasts were provided by the Royal Netherlands Meteorological Institute (KNMI). A similar 60-level vertical resolution was used for the forecasts; however, the vertical grid differed from COAMPS. Both models have at least 20 levels in the lowest 2000 m, with COAMPS having 27 levels and HARMONIE-AROME having 21 levels, and both models have at least 10 levels in the lowest 500 m, with COAMPS having 13 and HARMONIE-AROME having 10. The vertical heights used for both COAMPS and HARMONIE-AROME for the lowest 2000 m are shown in Figure 22. A horizontal resolution of 2.5 km was also used to minimize model differences, with a LatLon projection. Hourly forecasts were also generated with HARMONIE-AROME; however, these were produced with 3-hr reinitialization times. The SST analyses used to initialize the ocean surface were provided by the European Centre for Medium-Range Weather Forecasting (ECMWF) model. The HARMONIE-AROME grid is shown in Figure 23.
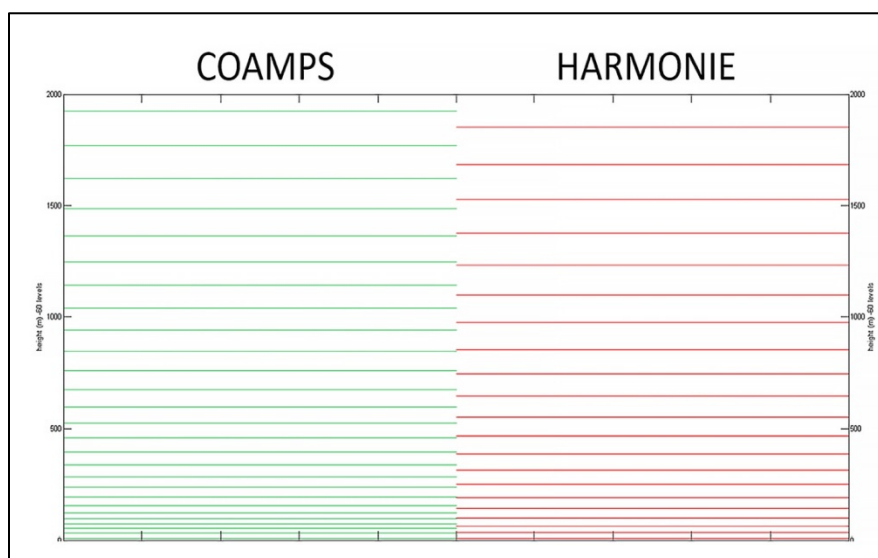
Figure 22. COAMPS and HARMONIE-AROME vertical grid resolution below 2000 m
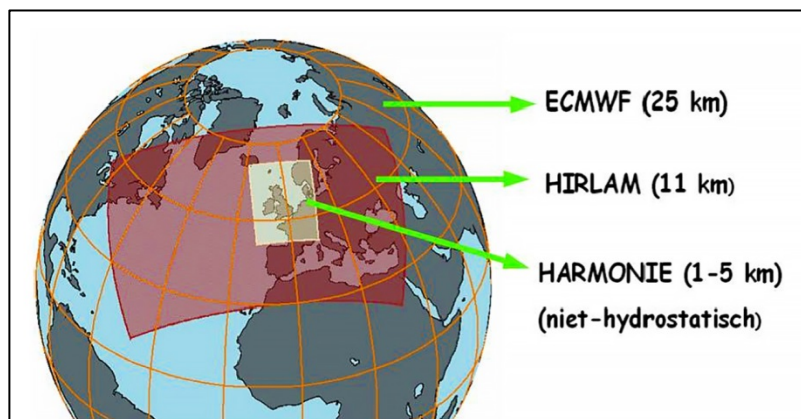
Figure 23. The HARMONIE-AROME grid used during the Phase 1 test.

3.3 INITIAL RESULTS

When comparing COAMPS and HARMONIE-AROME SSTs, it was determined that several degrees of temperature difference exists between the NCODA and ECMWF analyses throughout the test event. An example of the comparison is shown in Figure 24. KNMI and NSWCDD are currently investigating these differences. During the test event, atmospheres close to standard were measured with some elevated ducting or super-refraction present.
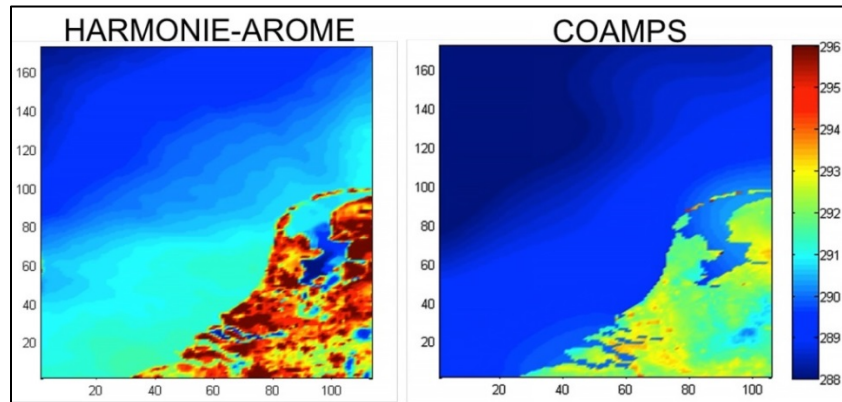
Figure 24. SST comparisons between COAMPS and HARMONIE-AROME on 2014 Sep 11 1200Z.

Comparisons among COAMPS, HARMONIE-AROME, and the radiosonde data were made for potential temperature, water vapor mixing ratio, and modified refractivity. This comparison allows evaluation of the thermodynamics to determine the differences in refractivity predictions. Sonde comparisons in potential temperature varied with some matching COAMPS and others matching HARMONIE-AROME. An example of the potential temperature comparison is shown in Figure 25. Both models under-predicted potential temperature in the boundary layer and over predicted it in the free atmosphere. Figure 26 shows the mean bias of potential temperature for COAMPS and HARMONIE-AROME.
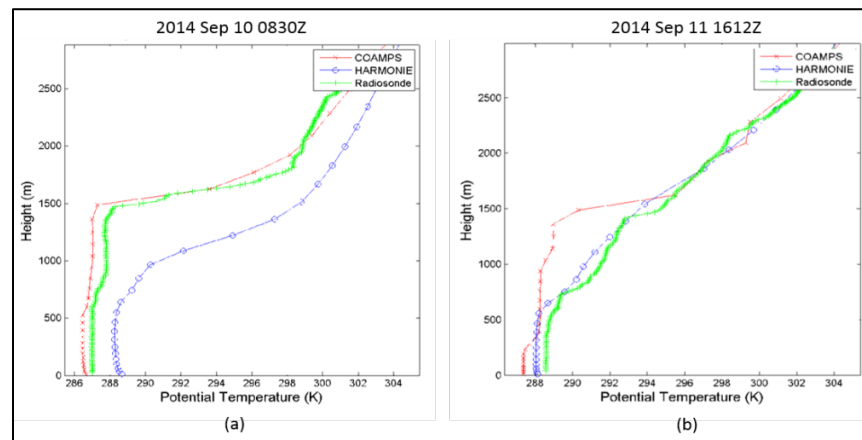
Figure 25. Example of the potential temperature comparison between COAMPS and HARMONIE-AROME and the measured radiosonde. (a) COAMPS matching; and (b) HARMONIE-AROME matching.

Water vapor mixing ratio comparisons varied significantly with COAMPS and HARMONIE-AROME matching the radiosonde profiles well at some heights and not at others. An example of this comparison is shown in Figure 27. In general, models under-predicted WVMR at the surface and then diverged aloft. The mean bias for COAMPS and HARMONIE-AROME is shown in Figure 28. The largest RMSE was noted near the inversion; however, the value of RMSE was relatively small, less than 1g/kg. Figure 29 shows the WVMR RMSE.

During the field testing, the environment was close to standard atmosphere, with some elevated ducting or super refraction present periodically. Figure 30 shows the comparison of calculated modified refractivity from the radiosonde and COAMPS and HARMONIE-AROME. The bias profile statistics show similar trends to the WMVR results, models under predict modified refractivity at the surface and then they diverged aloft. Figure 31 shows the modified refractivity bias profile statistics for COAMPS and HARMONIE-AROME. Similar to RMSE for WVMR, the largest modified refractivity RMSEs occurred above the inversion. Figure 32 shows the RMSE for modified refractivity.
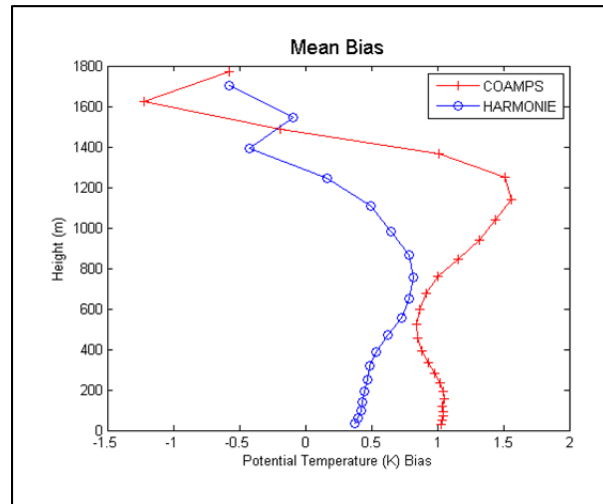
Figure 26. The mean bias of potential temperature for COAMPS and HARMONIE-AROME.
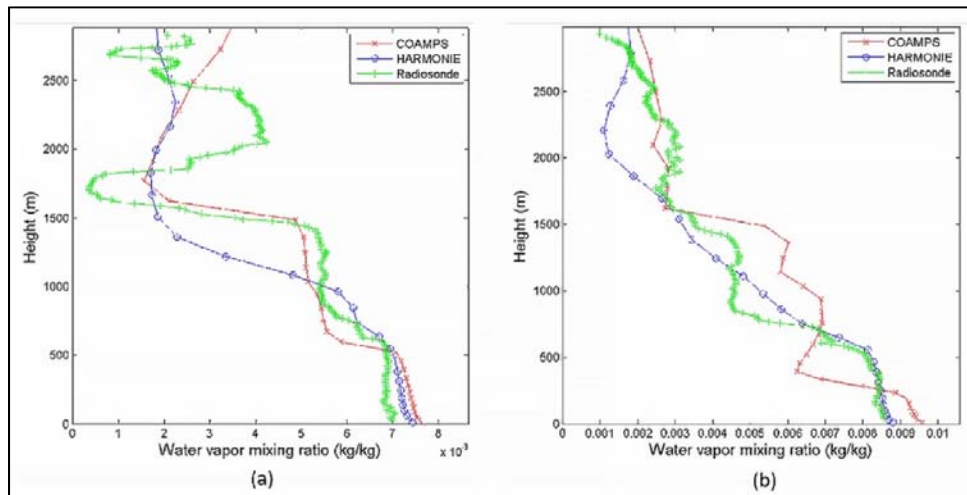
Figure 27. (a) Example of the water vapor mixing ratio comparison between COAMPS and HARMONIE-AROME, and (b) the calculation from the measured radiosonde data.

23
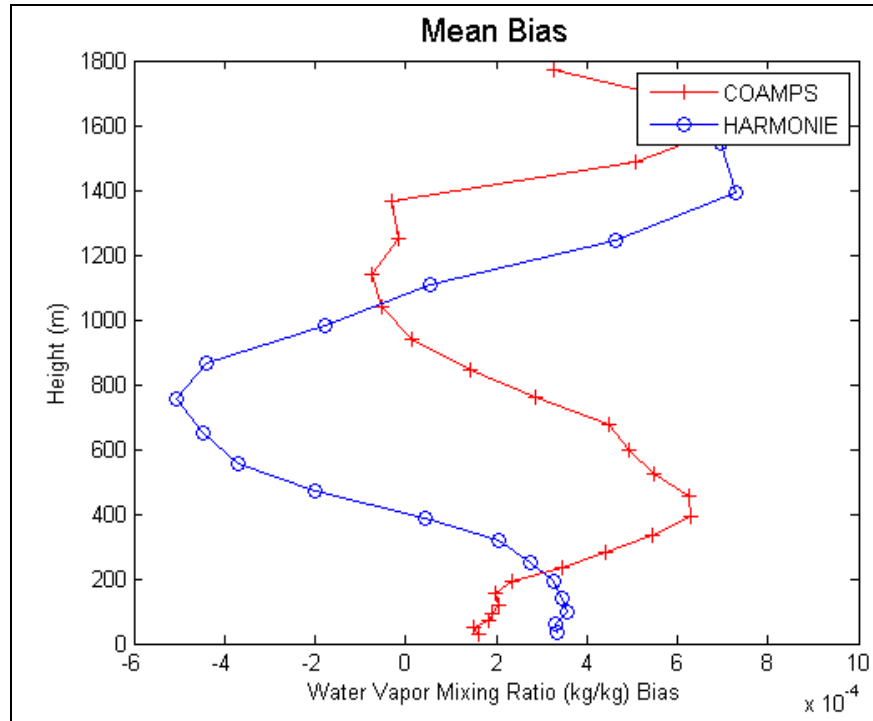
Figure 28. The WVMR mean bias for COAMPS and HARMONIE-AROME.
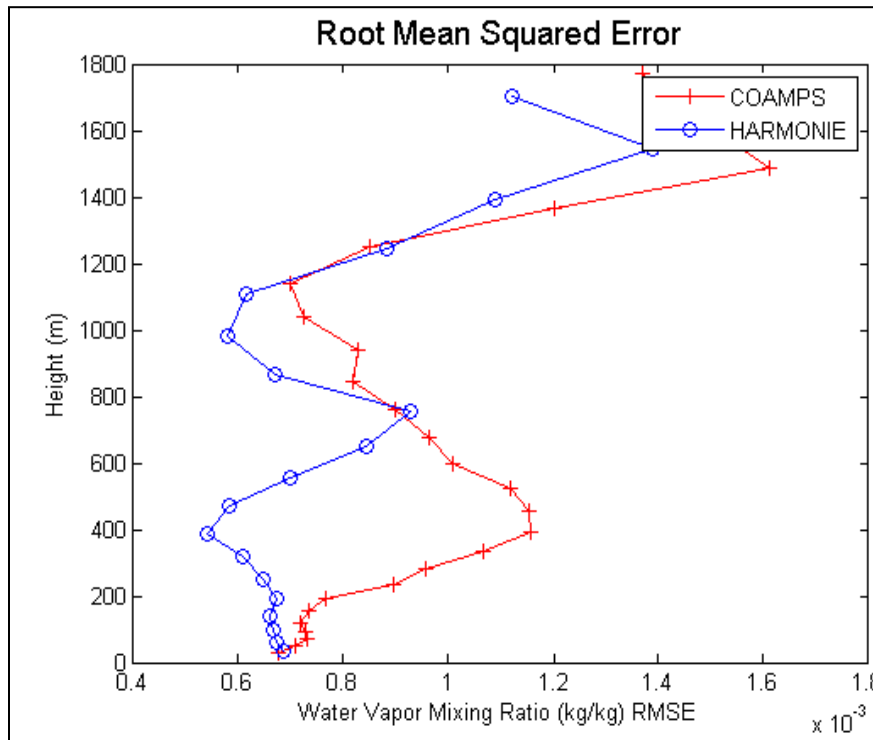
Figure 29. WVMR RMSE for COAMPS and HARMONIE-AROM.

24
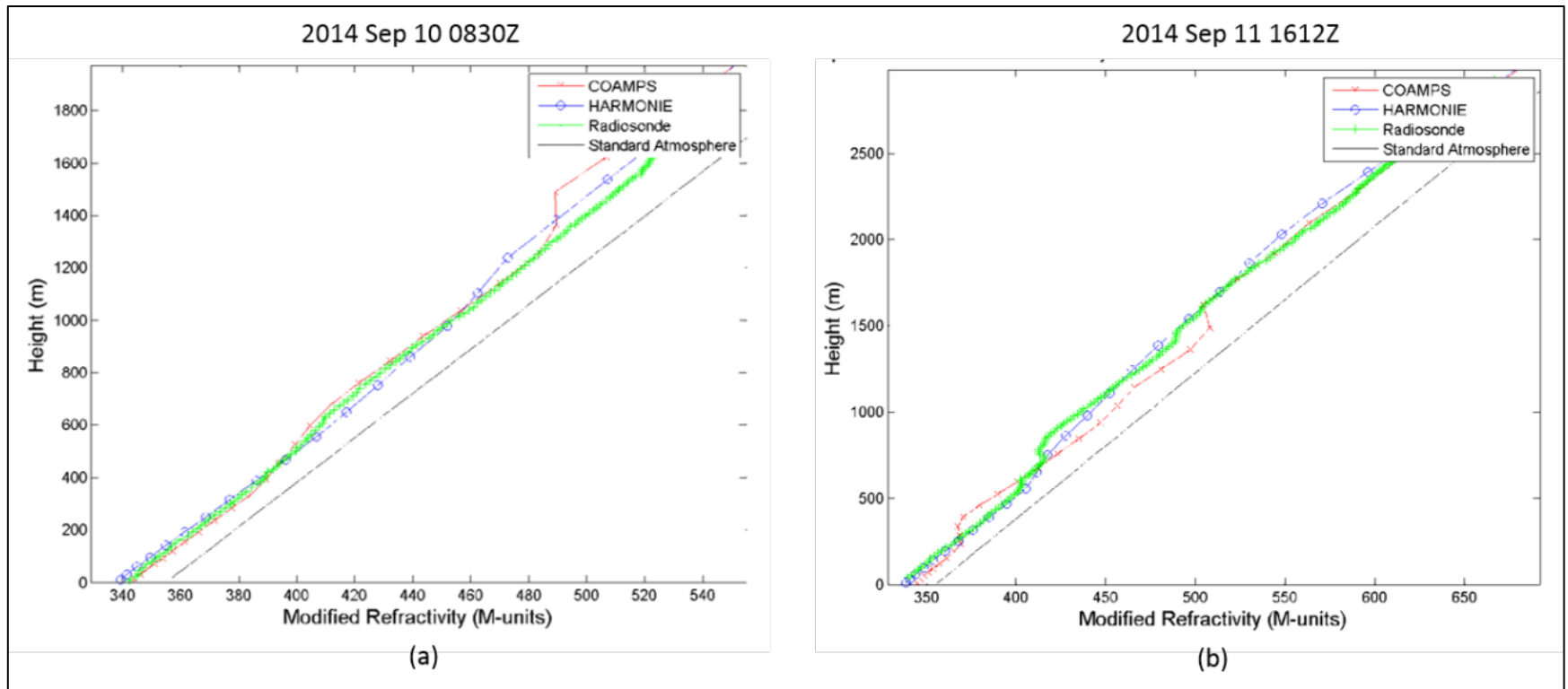
Figure 30. Example of the modified refractivity comparison between COAMPS and HARMONIE-AROME and the calculation from the measured radiosonde data: (a) elevated ducting, and (b) super-refraction.
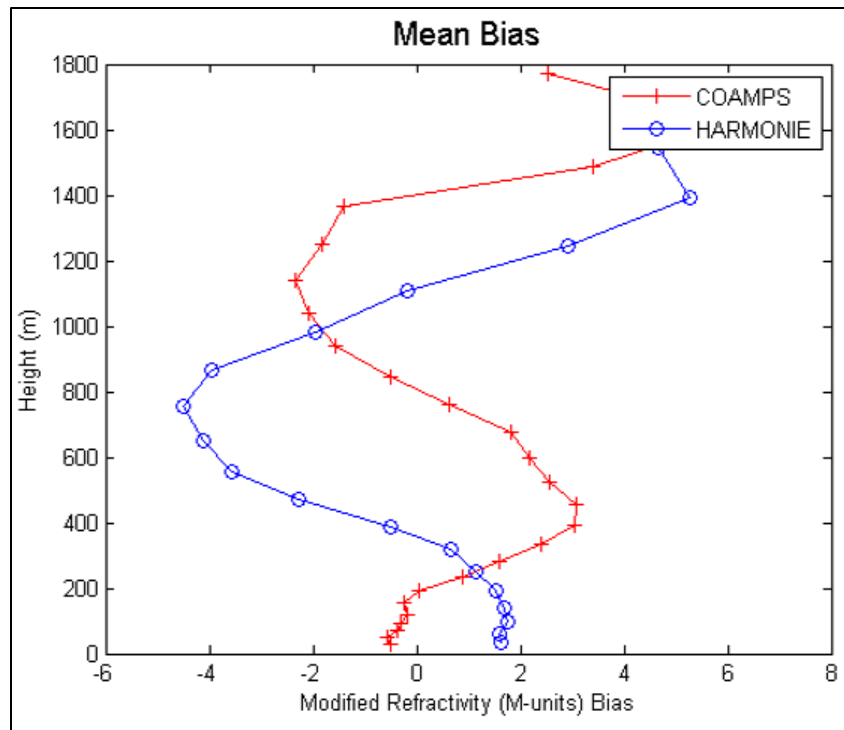
Figure 31. Modified refractivity bias profile statistics for COAMPS
and HARMONIE-AROME.
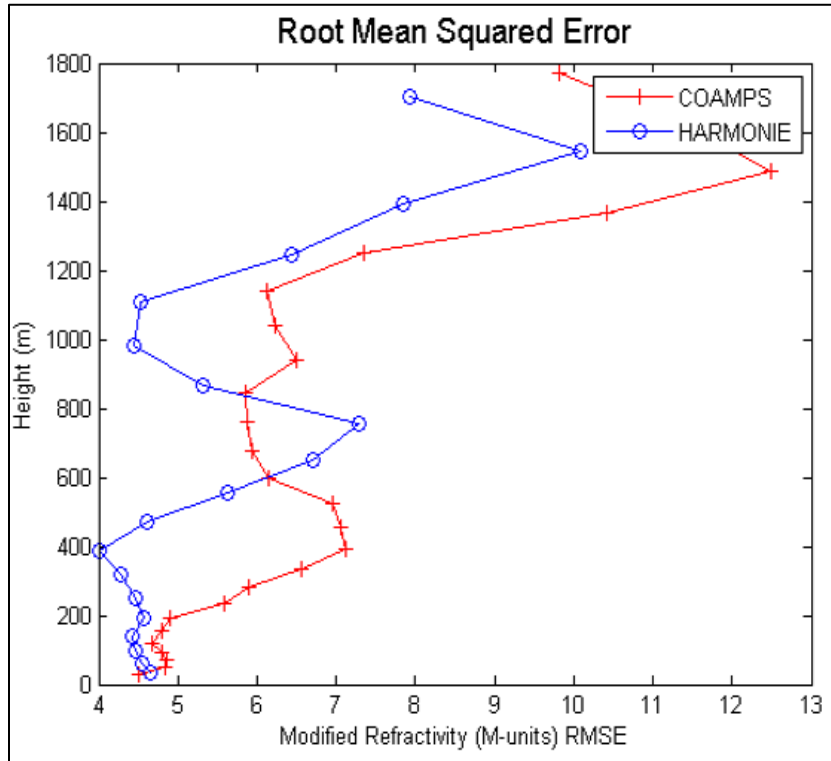
Figure 32. RMSE for modified refractivity.

These small differences in modified refractivity can be significant in propagation space. Figure 33 shows how these small differences manifest in propagation space by moving the nulls several miles, potentially creating significantly different results for the radar. Two examples are shown, 2014 Sep 10 at 0830Z and 2014 Sep 11 at 1612Z.

In summary, the overall thermodynamic profile bias and RMSE was low for both models, the largest RMSE errors were near the inversion and had a relatively small value, less than 2 °K in potential temperature and less than 1g/kg in mixing ratio. At the surface, HARMONIE-AROME had a small cold bias with a larger dry bias, while COAMPS had a larger cold bias with a smaller dry bias. Significant sea surface temperature differences were observed which may have led to the surface temperature and moisture errors. In propagation loss, due to lack of large-scale ducting features, differences in the gradient of M caused the nulls between 10–15 km to move in range by only a few miles.
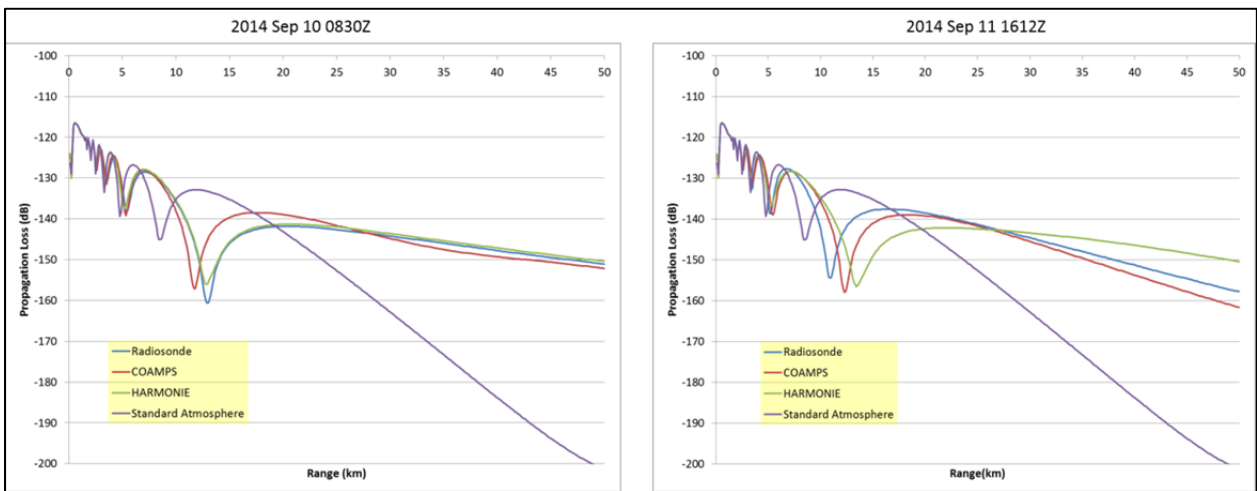
Figure 31. Notional X-band radar with a target at 10 m and the propagation loss comparison from standard atmosphere.

4. OBSERVATIONS

During the IOP, the area was dominated by a high-pressure system, with winds coming from the NW on 9 Sep 2014 but shifting to a NE direction by the end of the IOP on 12 Sep 2014. This is evident by the GPS tracks of the radiosondes taken during this time period. Winds in the area, as well as the radiosonde and FRISC tracks for each day, are shown in Figures 34 to 37. Figures 34(a) to 37(a) are provided by the Global Data Assimilation System (GDAS) (Smith,,Allard, and Caroll, 2016) . Note that on 9 Sep 2014, one of the Rotte tug-based radiosondes was launched without the plunger removed, resulting in the unusually long GPS track.
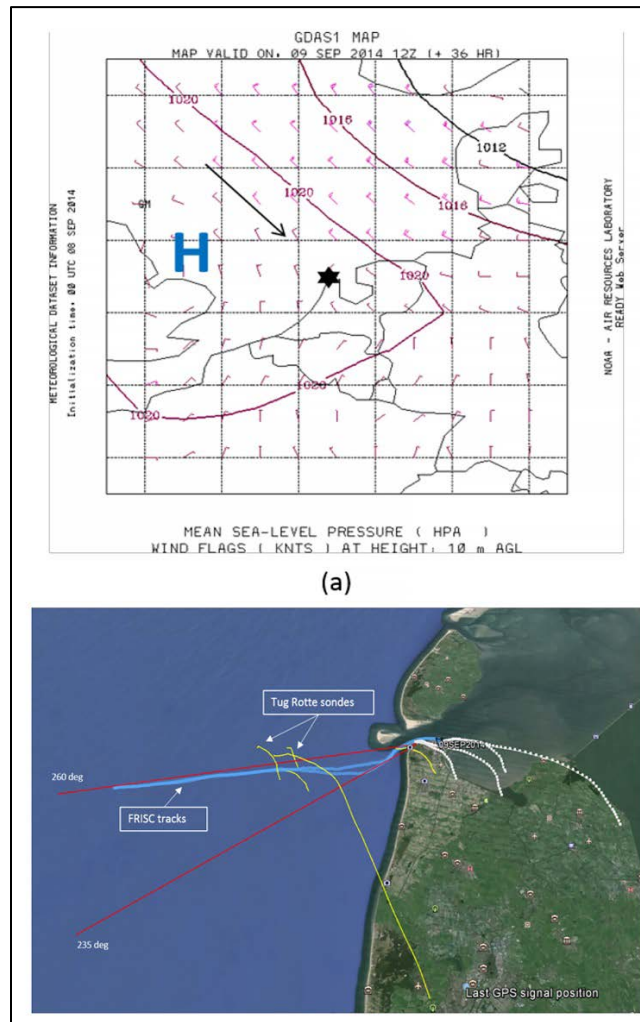
Figure 34. (a) Winds in the Den Helder area (Den Helder indicated by ✶), and (b) radiosonde and FRISC observation tracks on 9 Sep 2014.
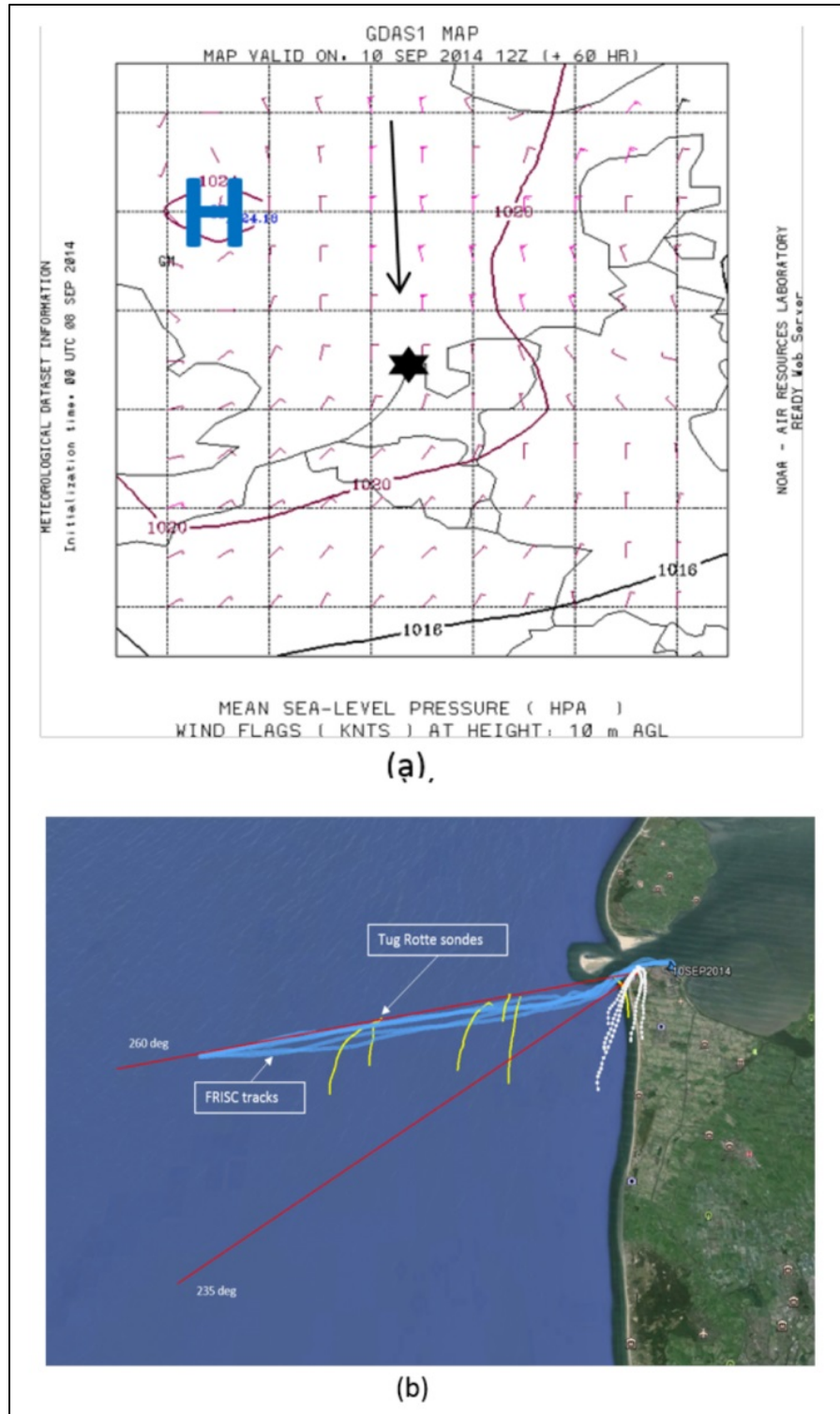
Figure 35. (a) Winds in the Den Helder area (Den Helder indicated by ✦), and (b) radiosonde and FRISC observation tracks on 10 Sep 2014.
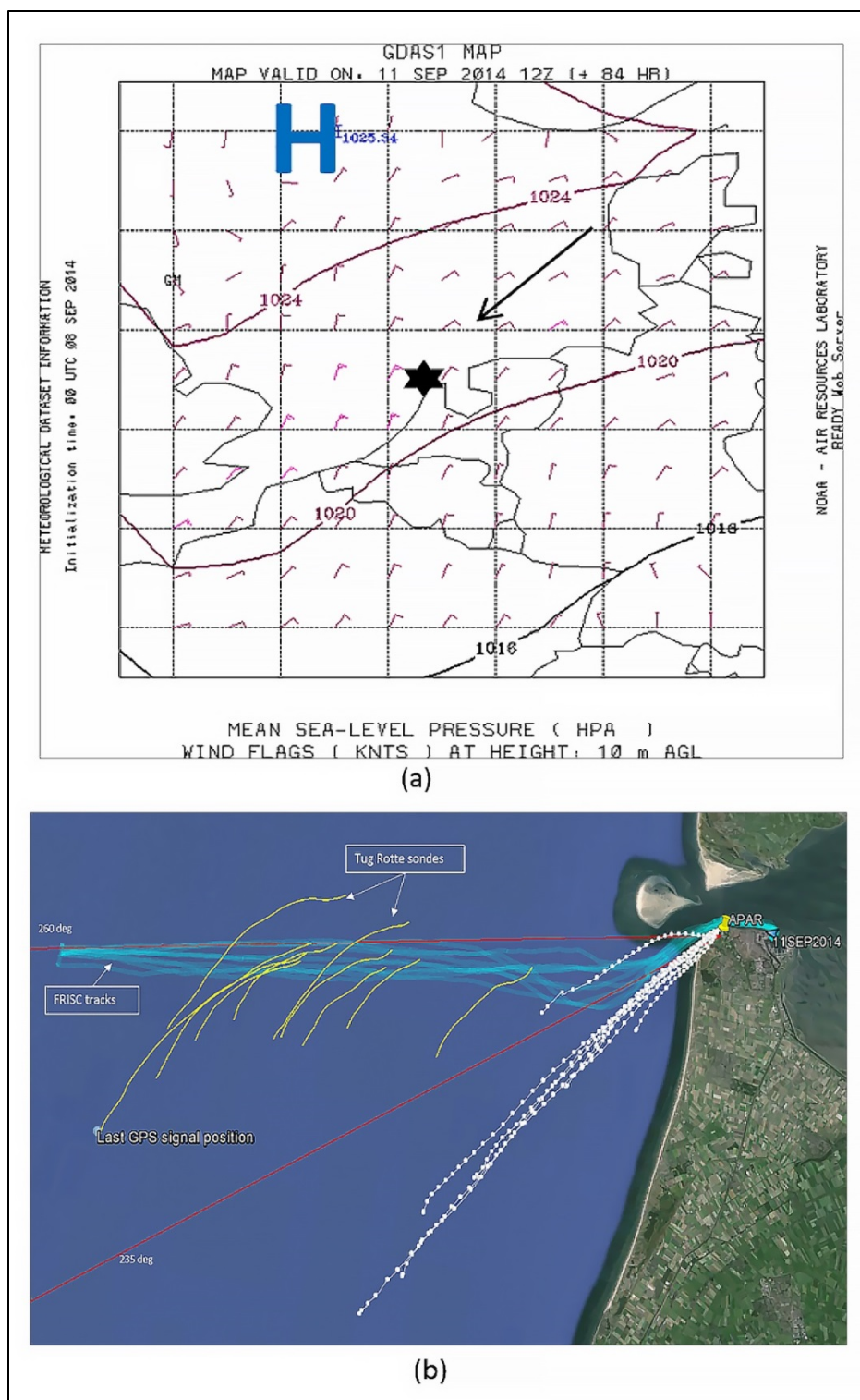
Figure 36. (a) Winds in the Den Helder area (Den Helder indicated by ✶), and (b) radiosonde and FRISC observation tracks on 11 Sep 2014.
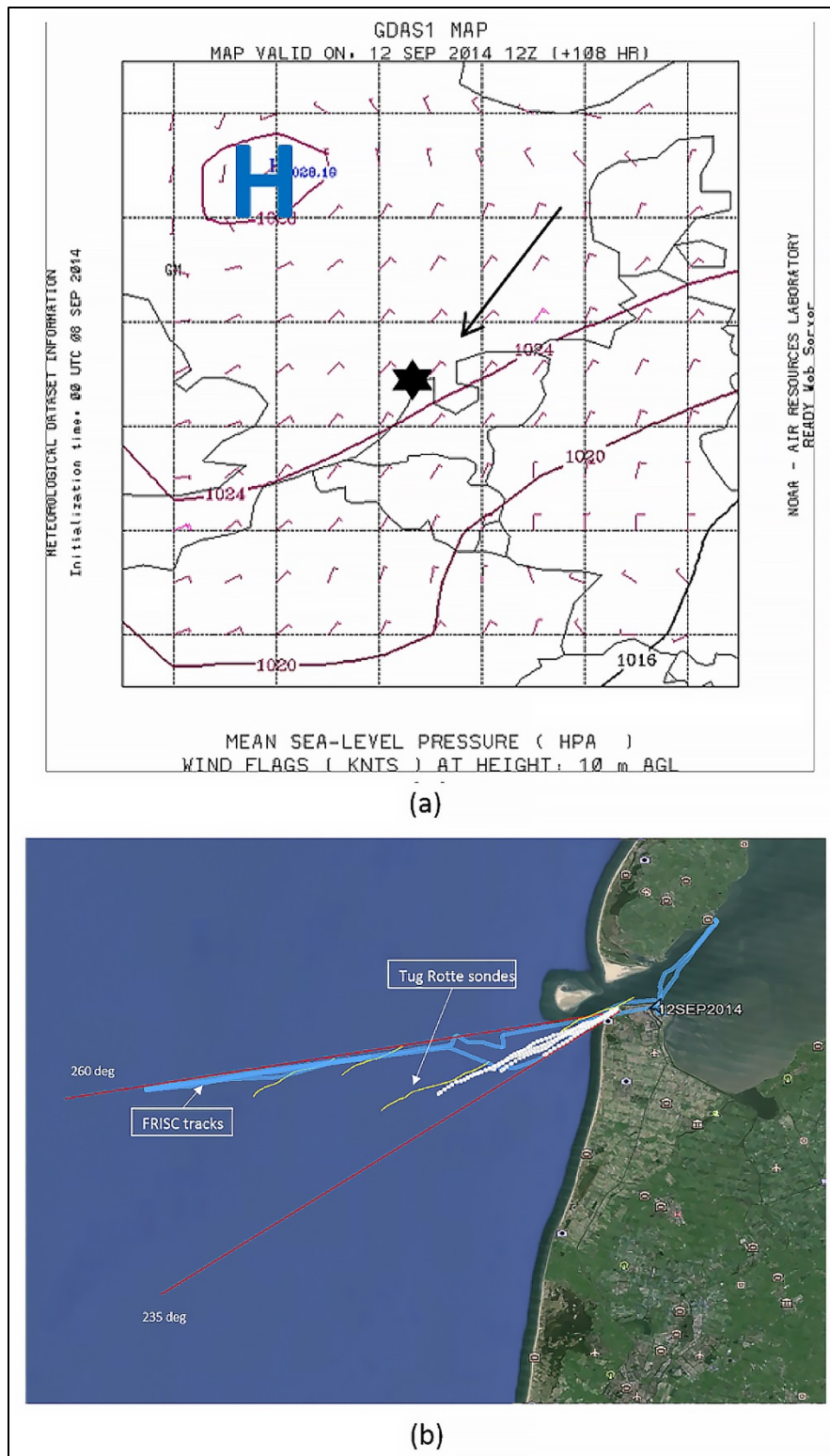
Figure 37. (a) Winds in the Den Helder area (Den Helder indicated by ✶), and (b) radiosonde and FRISC observation tracks on 12 Sep 2014.

Several outbound and inbound tracks, or "runs," of the FRISC were logged each day during the IOP. The start times for each outbound and inbound run are listed chronologically in Table 5. All times are in UTC.

Table 5. FRISC outbound and inbound start times in UTC.

Day (Sep)	Run 1		Run 2		Run 3		Run 4		Run 5	
	Out	In	Out	In	Out	In	Out	In	Out	In
9	12:36	13:42	14:11	15:00						
10	07:10	08:12	09:22	10:17	11:18	12:12	13:20	14:12		
11	07:27	08:26	09:24	10:24	11:33	12:28	13:25	14:09	15:16	16:02
12	07:33	08:10	08:27	08:57						

Tidal information was obtained from the Dutch Ministry of Infrastructure and the Environment (http://www.rijkswaterstaat.nl/kaarten/waterstand-tov-nap.aspx). In this area, tides varied between ±1.0 m. Transmitter antenna heights ASL were corrected for tide heights; however, the maximum tidal variation during any one FRISC run varied by no more than approximately 0.4 m. Tide height as a function of time for each day, relative to 1 Sep 2014 00:00Z, is shown in Figure 38. The time duration for each outbound and inbound interval are indicated by the blue and red shading, respectively. Notice that on 12 Sep 2014, the final inbound FRISC run contains a time gap due to the FRISC maneuvering outside the lower FoV of the APAR, but subsequently returning within its FoV as it neared the LBTS.
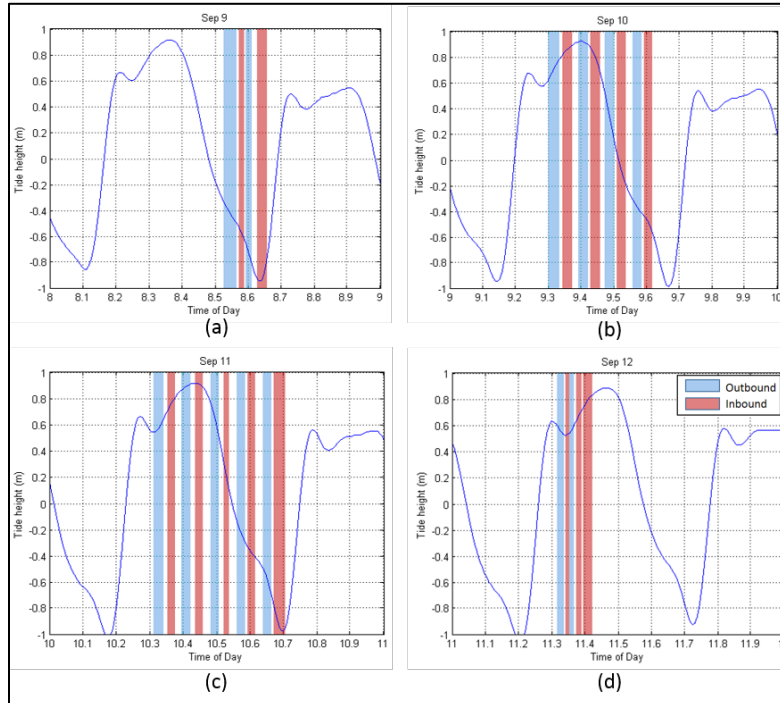
Figure 38. Tide height vs. time of day, along with FRISC outbound and inbound run times for (a) Sep 9, (b) Sep 10, (c) Sep 11, and (d) Sep 12.

4.1 UPPER AIR MEASUREMENTS

As mentioned previously, radiosondes were launched from near the LBTS and the Rotte tug at near-simultaneous times. The launch times for all radiosondes are listed in Table 6 in HH:MM:SS (UTC) format.

Vertical profiles of pressure in hPa, temperature in Kelvin, relative humidity (%), refractivity in M-units, and gaseous attenuation rate (dB/km) from both the Rotte tug and the onshore site are provided in Figures A-1 to A-26 in the Appendix. Note that for several soundings, measurements were available only on the ascent trajectory.

Table 6. Radiosonde launch times (UTC).

Sep 9		Sep 10		Sep 11		Sep 12	
Rotte tug	Shore	Rotte tug	Shore	Rotte tug	Shore	Rotte tug	Shore
07:58:11	07:58:00	07:09:46	07:10:00	07:14:52	07:13:00	07:02:45	07:01:00
07:58:30		08:30:11	08:28:00	08:31:34	08:29:00	08:03:20	08:03:00
09:59:10	10:00:00	09:51:27	09:44:00	09:33:57	09:35:00	08:45:45	08:46:00
12:37:29	13:12:00	11:01:41	10:58:00	10:29:03	10:28:00	09:29:36	09:30:00
13:50:56	13:50:00	12:16:55	12:15:00	11:15:56	11:14:00		
14:38:54	14:36:00	13:31:08	13:29:00	12:18:47	12:18:00		
				13:00:00	13:01:00		
				13:45:05	13:45:00		
				14:24:50	14:25:00		
				15:15:49	15:17:00		
				16:12:15	16:13:00		

4.2 TACMET (NEAR-SURFACE) MEASUREMENTS

The surface layer, or "bulk" measurements, collected from both TACMET stations (shore-side and on the Rotte tug) are shown in Figures 39 to 42. Unfortunately, equipment issues with the shore-side TACMET station prevented data collection for the morning of the last day on Sep 12, so only data collected from the Rotte tug is shown for this day. Wind speed is shown for both the 2- and 10-min averages. Air temperature measurements from the TACMET are shown in blue, for both the Rotte tug and shore-side stations; however, shown in red are point SST values, which represent the bucket measurements from the Rotte tug (bottom plots). Since there were no shore-side SST measurements during the IOP, what is used for the analysis described in Section 5.4.2 are mean SST values based on climatology at the nearest latitude/longitude for the month and hour nearest each FRISC start time. The source of the climatology is a surface layer database developed by the NPS, and is based on the Climate Forecast System Reanalysis dataset from 1979–2009 (Frederickson, Murphee, Twigg, and Barrios, 2008).

The time of day shown is relative to 1 Sep 2014 00:00:00 UTC for all figures and the time interval (x-axis) for each plot represents the time span between 30 min prior to the start of the first FRISC track to 30 min after the last FRISC track.
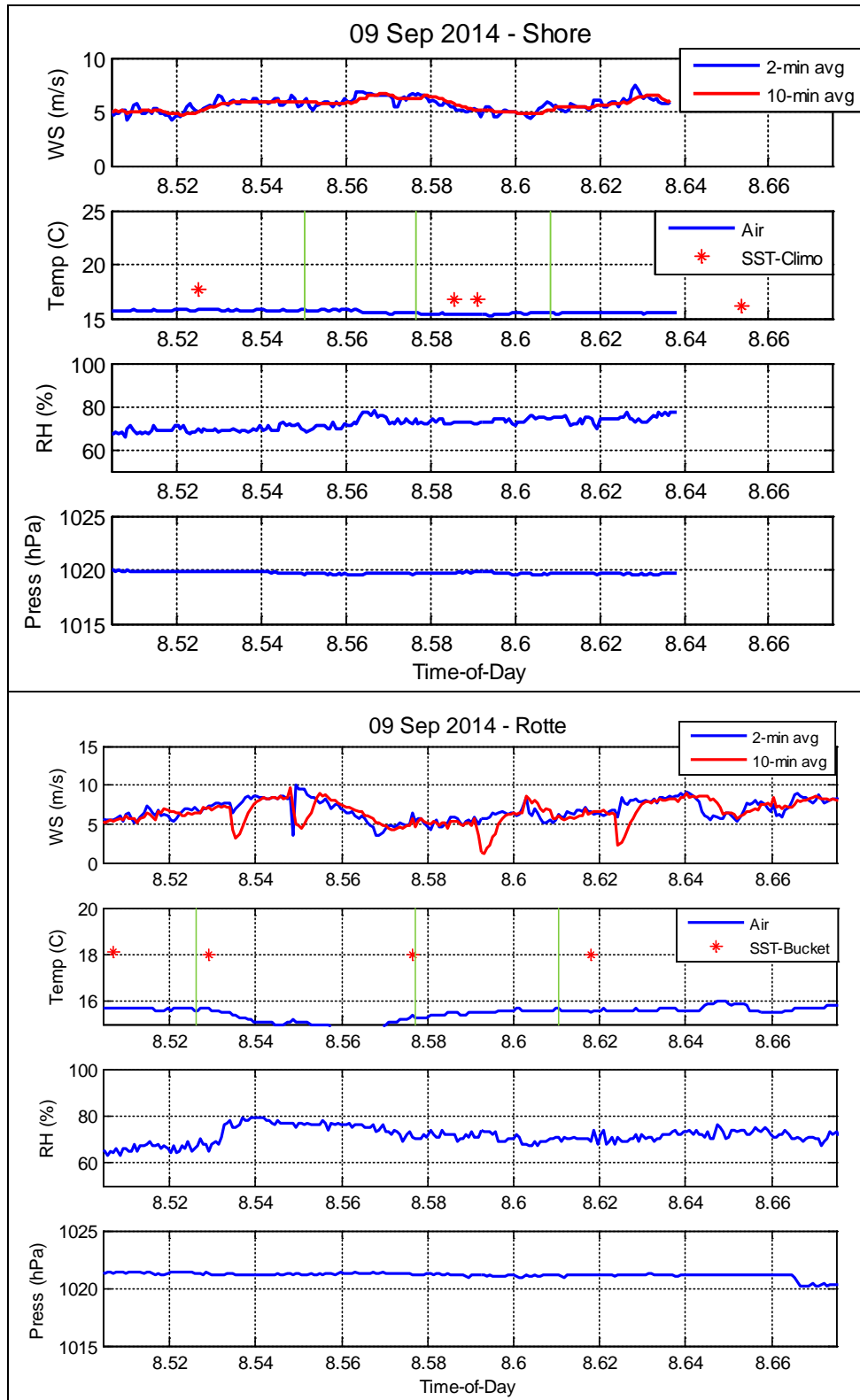
Figure 39. 09 Sep 2014 TACMET near-surface measurements from shore-side near the LBTS (top), and from the Rotte tug (bottom). The green vertical lines in the temperature graphic indicate radiosonde launch times.
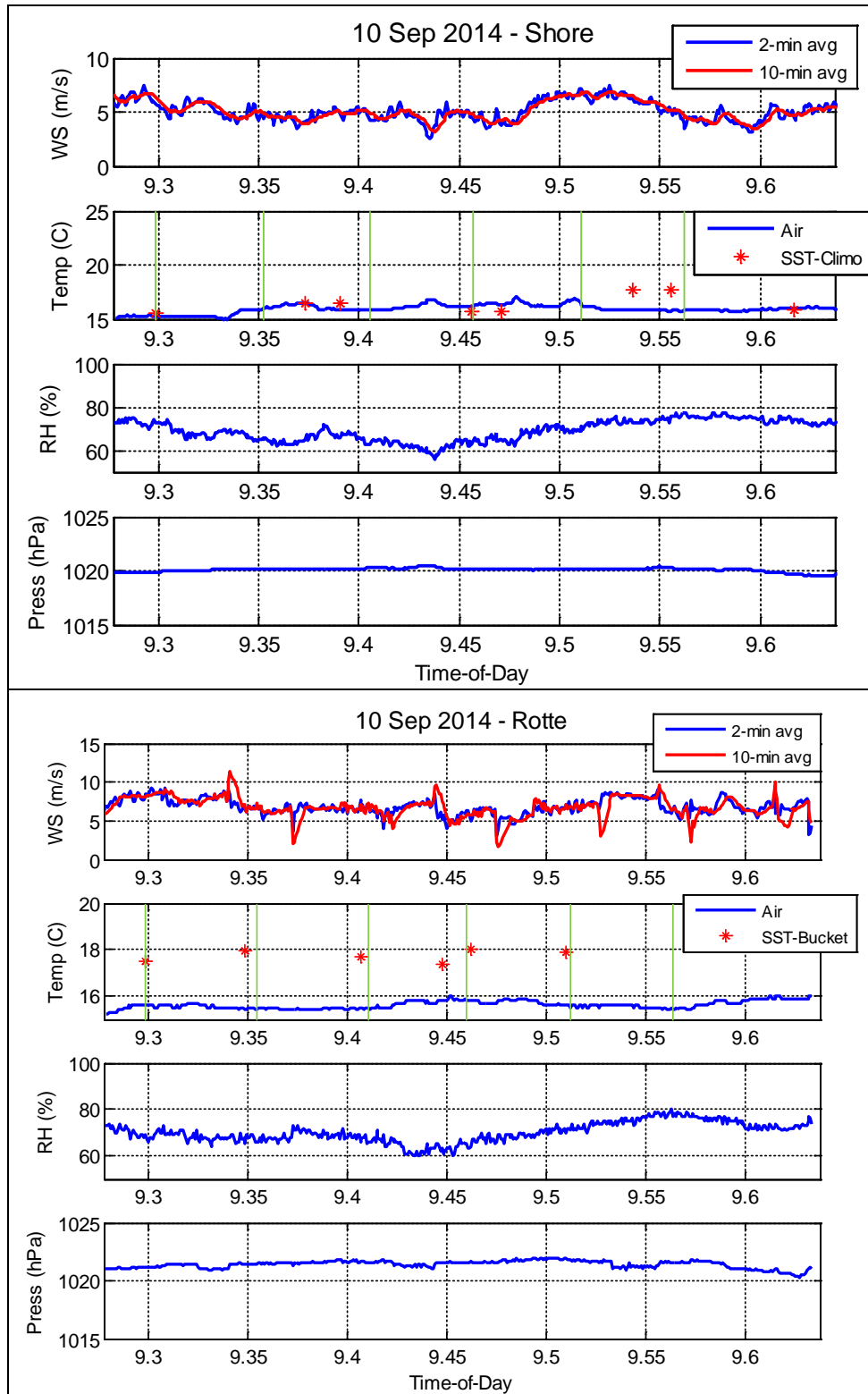
Figure 40. 10 Sep 2014 TACMET near-surface measurements from shore-side near the LBTS (top), and from the Rotte tug (bottom). The green vertical lines in the temperature graphic indicate radiosonde launch times.
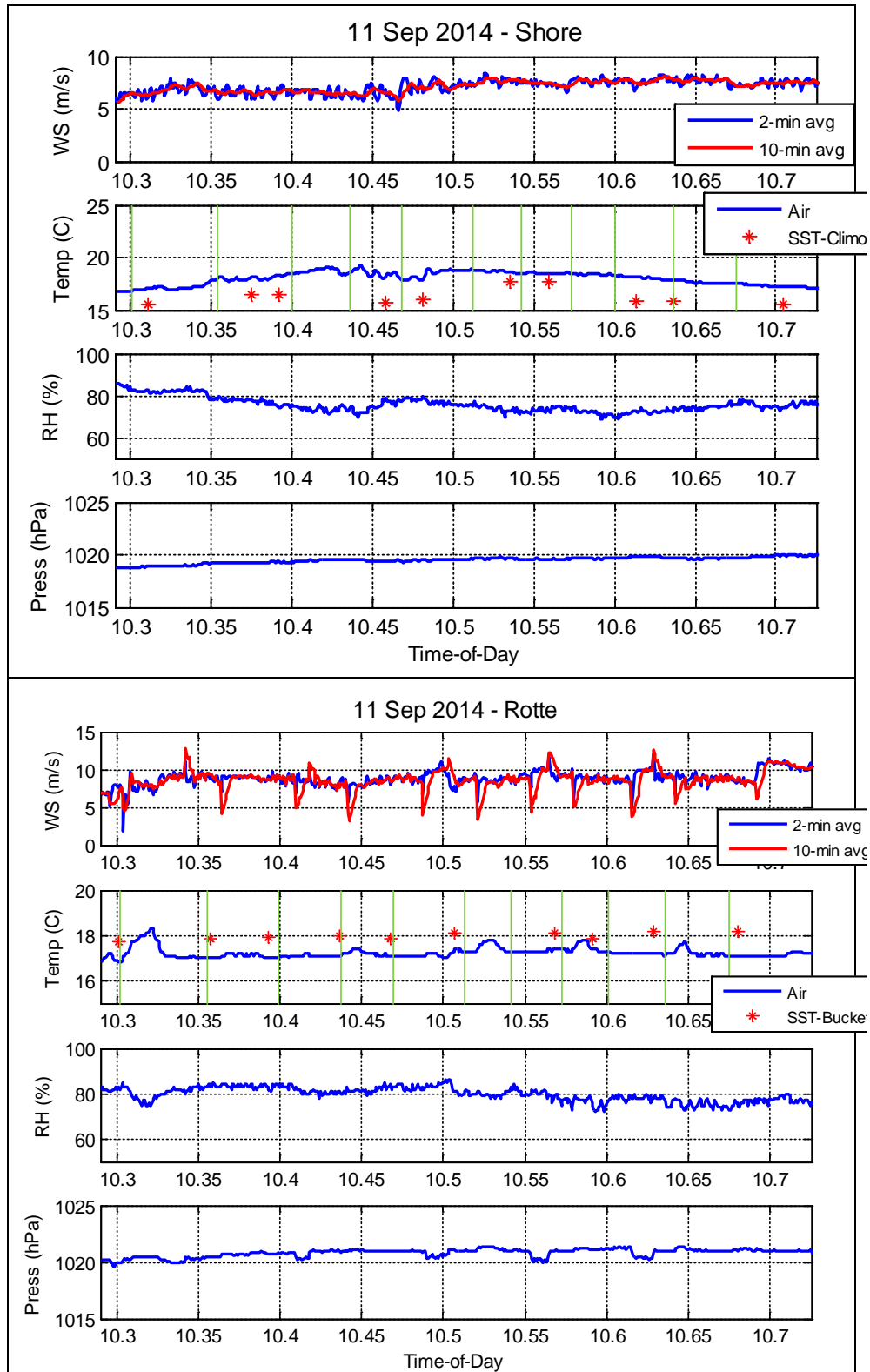
Figure 41. 11 Sep 2014 near-surface measurements from shore-side near the LBTS (top), and from the Rotte tug (bottom). The green vertical lines in the temperature graphic indicate radiosonde launch times.
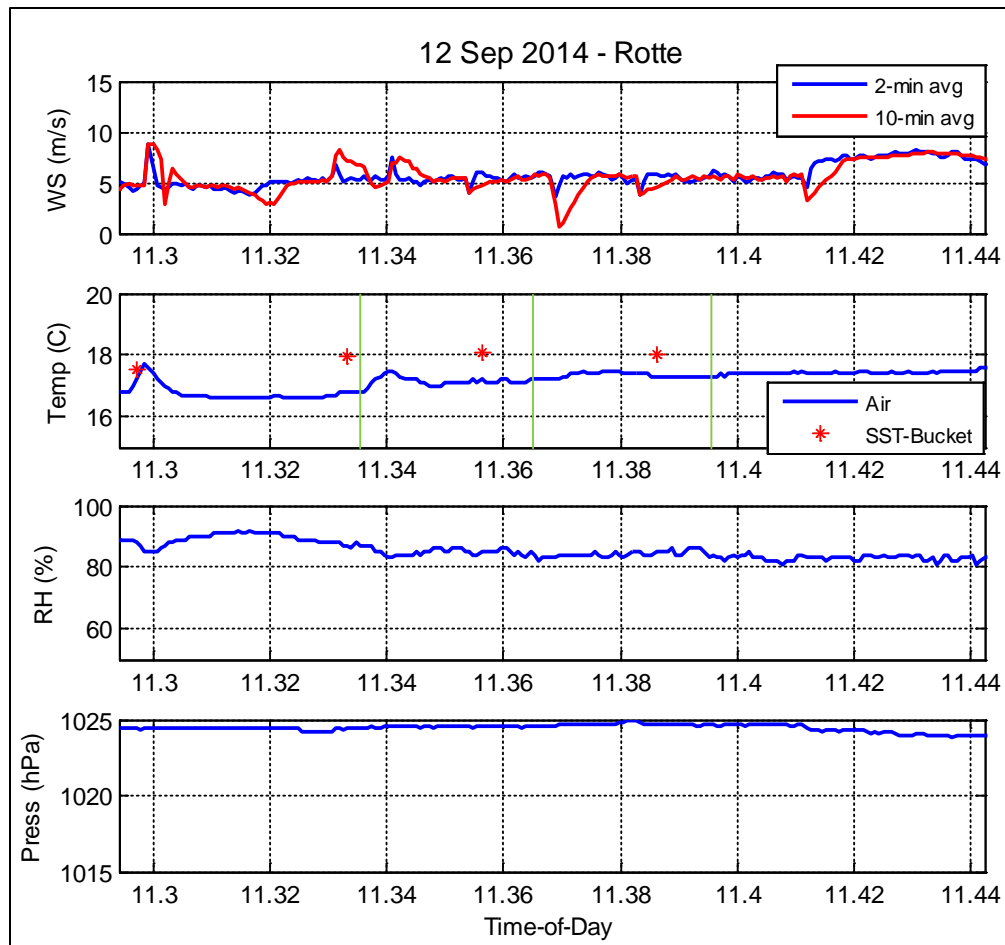
Figure 42. 12 Sep 2014 near-surface measurements from the Rotte tug. The green vertical lines in the temperature graphic indicate radiosonde launch times.

5. DATA ANALYSIS

5.1 NWP MODELS

A general "look" at the overall differences in the COAMPS and HARMONIE NWP models is provided here, particularly for their subsequent influence on the propagation predictions discussed in the Section. However, our intent is not to investigate in detail the underlying mesoscale methods and algorithms between the models discussed in this report, but to simply provide the observed differences, relevant to the Phase 1 geographic area, at the time of the IOP.

No upper air surface-based ducting conditions were forecast from either model, and indeed, none were observed based on refractivity profiles computed from the radiosonde measurements in Figures A-1 to A-26. Because of the low-altitude propagation path for the IOP, we expected some influence from the presence of evaporation ducts along the path, and both COAMPS and HARMONIE did predict a highly variable evaporation duct environment in this region. An example of this is shown in Figure 43 where evaporation duct height contours are displayed over the region from both (a) COAMPS, and (b) HARMONIE for 11 Sep 2014 at 1200Z re-initialization and forecast time. The evaporation duct heights were computed using the Navy Atmospheric Vertical Surface Layer Model (NAVSLaM) Version 1.1, developed by the Naval Postgraduate School (NPS) (Frederickson, 2010) based on the surface layer parameters forecast from both models. The NAVSLaM was used throughout the analysis in this report. For this particular day and time, the evaporation duct heights differ anywhere from 1.0 to 5.0 m.
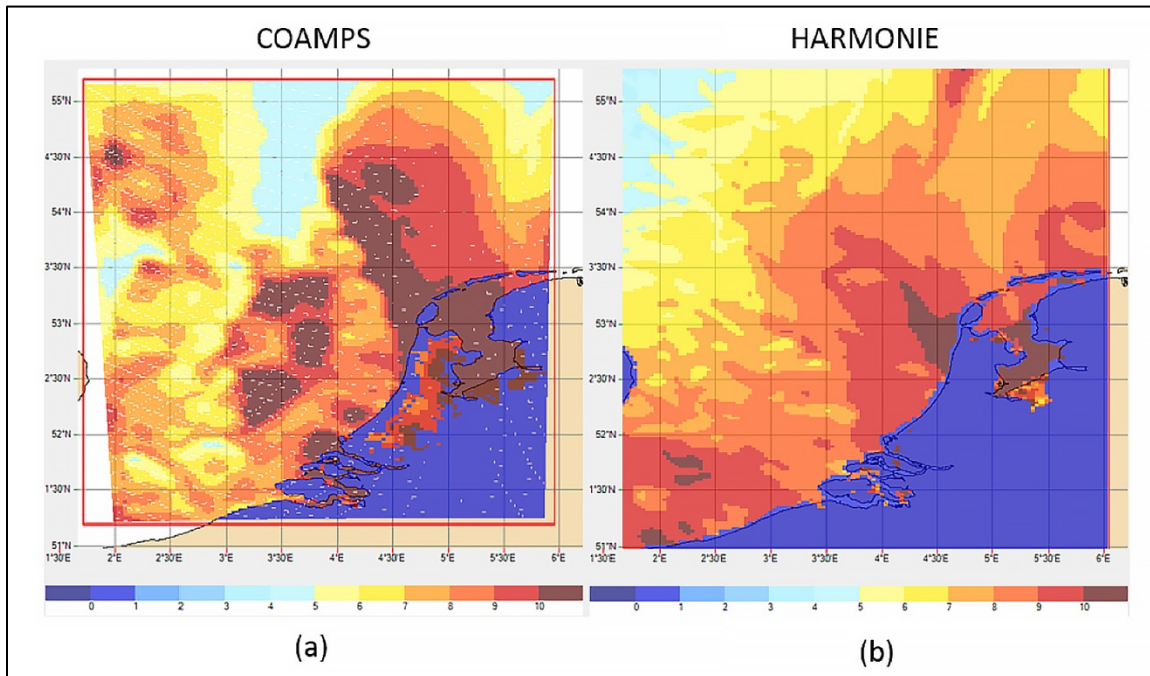
Figure 43. Evaporation duct height contours for 11 Sep 2014, 1200Z forecast and initialization times, from (a) COAMPS, and (b) HARMONIE NWP models.

However, comparing duct height alone does not give a complete picture of the overall propagation effects. Another refractivity-related, or diagnostic, parameter is M-unit deficit, or M-deficit, illustrated in Figure 44(a), where two evaporation duct profiles are shown with identical duct heights, but differ in the refractive gradients below and above the duct height. Previous work by Gerstoft et al. (2003) has shown the M-deficit to be one of the driving factors that influence the overall propagation. In Figure 44(a), the M-deficit is quite different for the profile in red (-11.3 M-units) than that shown in blue (-39.9 M-units, entire profile at 0.0 height not shown), although both profiles appear very similar. The resulting difference in propagation loss computed based on these two profiles is shown in Figure 44(b). Here the frequency and emitter parameters correspond to the APAR parameters in Table 1. Notice that differences can arise by as much as 20 dB or more, particularly at the low receiver altitudes below 10.0 m beyond approximately 35 km, the geometries of interest in this study. The corresponding M-deficit contours from evaporation duct profiles computed using both COAMPS and HARMONIE parameters in Figure 43 are shown in Figure 45.

In focusing primarily on the region where the Phase 1 data collection took place, Figure 46 shows a histogram of all evaporation duct heights determined for each day from both COAMPS and HARMONIE models at NWP grid points along the 260° radial out to 45 km in range only. The histograms are based on all forecast and re-initialization times from each model, for the entire day. The mean evaporation duct height for each day is indicated by the red dashed line. The mean duct heights based on the COAMPS model were consistently lower than the mean based on the HARMONIE model for each day, with the exception of 12 Sep 2014. For this day only the mean duct height from COAMPS is larger, and provides the greatest difference from the HARMONIE mean by 1.74 m.
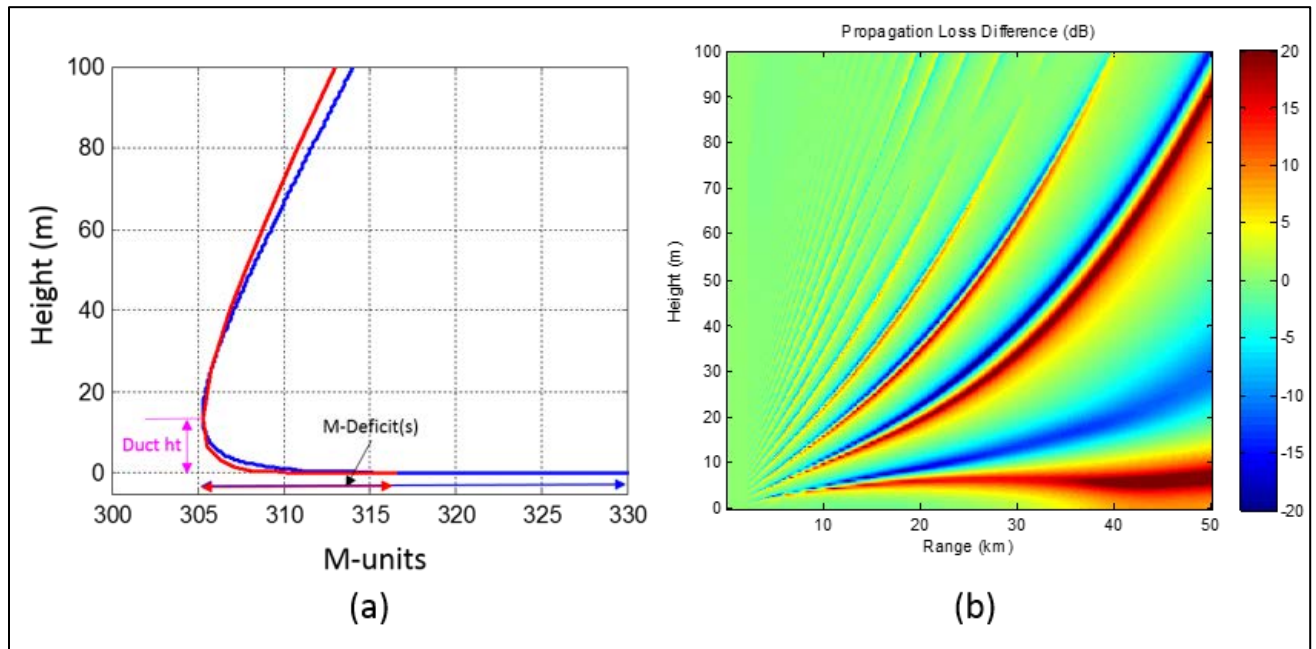
Figure 44. (a) Two evaporation duct profiles with equal duct heights of 14 m but significantly different M-deficits, and (b) the resulting difference in propagation loss based on the two range-independent profiles for an X-band emitter.
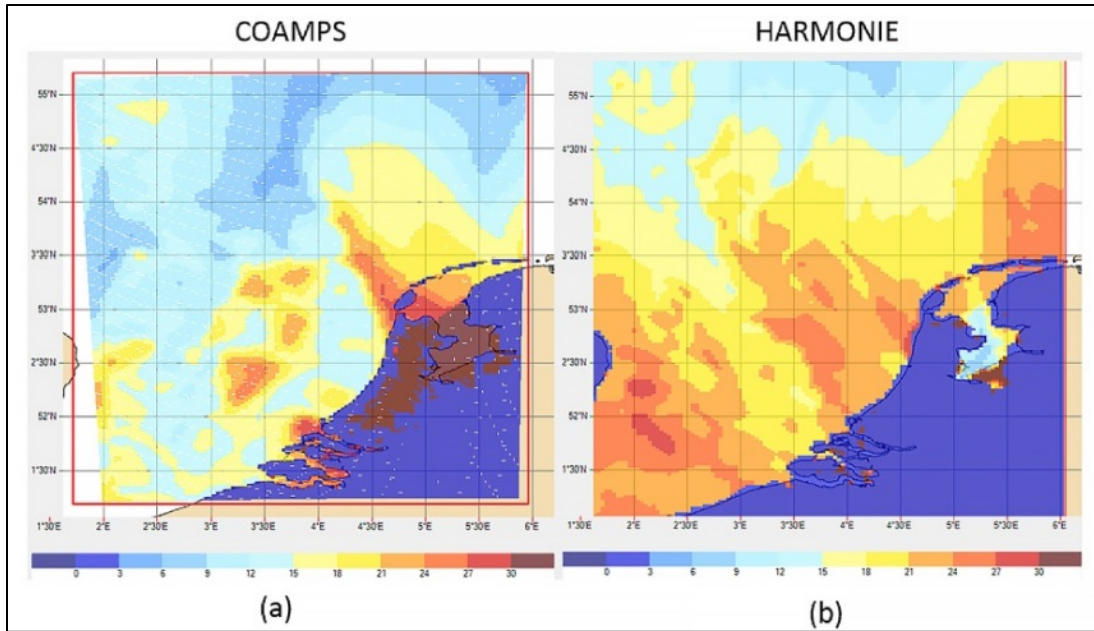
Figure 45. M-deficit contours of evaporation duct profiles computed from surface parameter forecasts for 11 Sep 2014, 1200Z forecast and initialization times, from (a) COAMPS, and (b) HARMONIE NWP models.
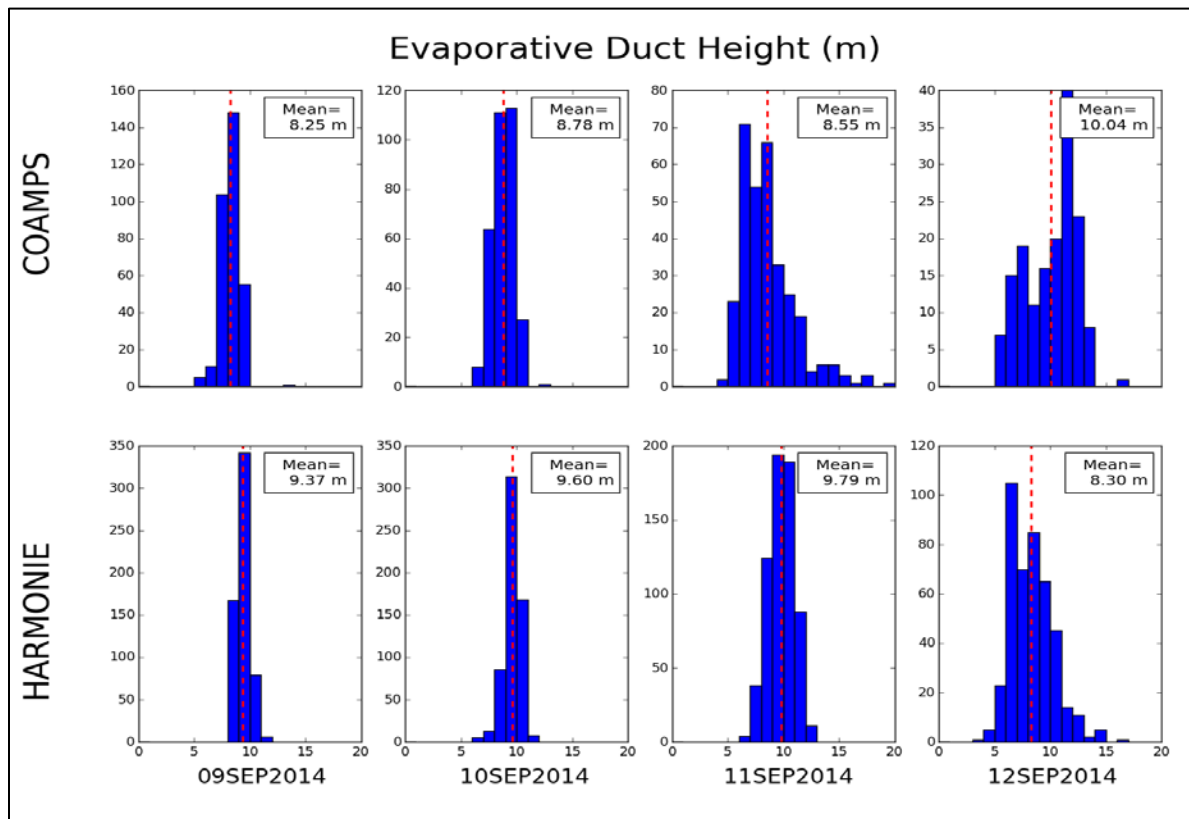
Figure 46. Histograms of evaporation duct height for COAMPS (top) and HARMONIE (bottom) models along a 260° radial out to 45 km in range.

5.2 S-BAND LINK

NSWC-DD provided a continuous wave (CW) S-Band transmitter with a nominal effective radiated power (ERP) of 26 dBm. Note that the methodology used in this report is to use relative power. Relative power is calculated by subtracting observed power at range r from observed power at a reference range r0. The slope of power versus range is a type of relative power comparison. The rationale for using such measurements is that referencing an observed power to the estimated ERP of the transmitting system is subject to uncertainty and error in the process of measuring or estimating ERP along with any drift in the ERP over time. Relative measurements are only subject to the drift.

5.3 X-BAND LINK

A system to capture pulses from the APAR was installed on board the Rotte tug. The pulse captures would coincide with the measurements from the S-Band link. The purpose of the measurements were twofold: (1) provide a back-up source of propagation measurements, and (2) support development of a passive capability to estimate ducting conditions.

The pulse-capture system used the Rohde and Schwarz® spectrum analyzer (described in Section 2.1.1), a Tecom 201822 1 to 18 GHz log periodic antenna (pointed aft), a control computer and associated RF and Ethernet® cabling. The pulse analysis software on the FSW allowed setting center frequency, bandwidth, and threshold for a trigger that would start in-phase and quadrature (I&Q) data collection at a 40-MHz sample rate. The pulses were displayed on the FSW and the I&Q data for pulses to be retained were saved as records via a semi-automated (to get the clock time) procedure. MATLAB® processing routines were written to calculate signal power for each I&Q record to produce the plots shown in Figure 47.

While the pulse captures show some potential for the purposes described in the first paragraph, the results for this campaign fall short of the goal. The reasons for this are as follows:

1. The maximum bandwidth for the FSW is 1.0 GHz. While the individual pulses from the APAR appear to be well less than this, the APAR's frequency-agile operation moves the center frequency of the pulses over a range that appears to be greater than the FSW's bandwidth. As a consequence, some APAR pulses had frequencies well within the pass-band of the FSW. In other instances, the pulses were outside the pass-band or at either edge. An interesting artifact of the latter is that as a pulse-compression radar, the frequency of the APAR pulse would change over a given pulse's duration. A consequence of that is that one end of the pulse would be further in the passband than the other and, as can be seen in Figure 47, the recorded amplitude would vary accordingly.
2. As a narrow-beam phased array system, the APAR dwells (i.e., the position in azimuth and height) vary as it scans in accordance with its control program. Dwells from adjacent positions (i.e., one or two bins above or to the side of the beam) still radiate enough power to trigger an FSW data collection. If the FSW could record each of these, an order statistic process such as ranking the pulse strengths over a minute might yield a stable power measurement. A limitation of the FSW, however, is that the time to save the I&Q data for a pulse was such that only three pulses could be collected per minute. Thus, the contamination of the data with adjacent beam data precludes using the data for our original purpose of estimating propagation loss.
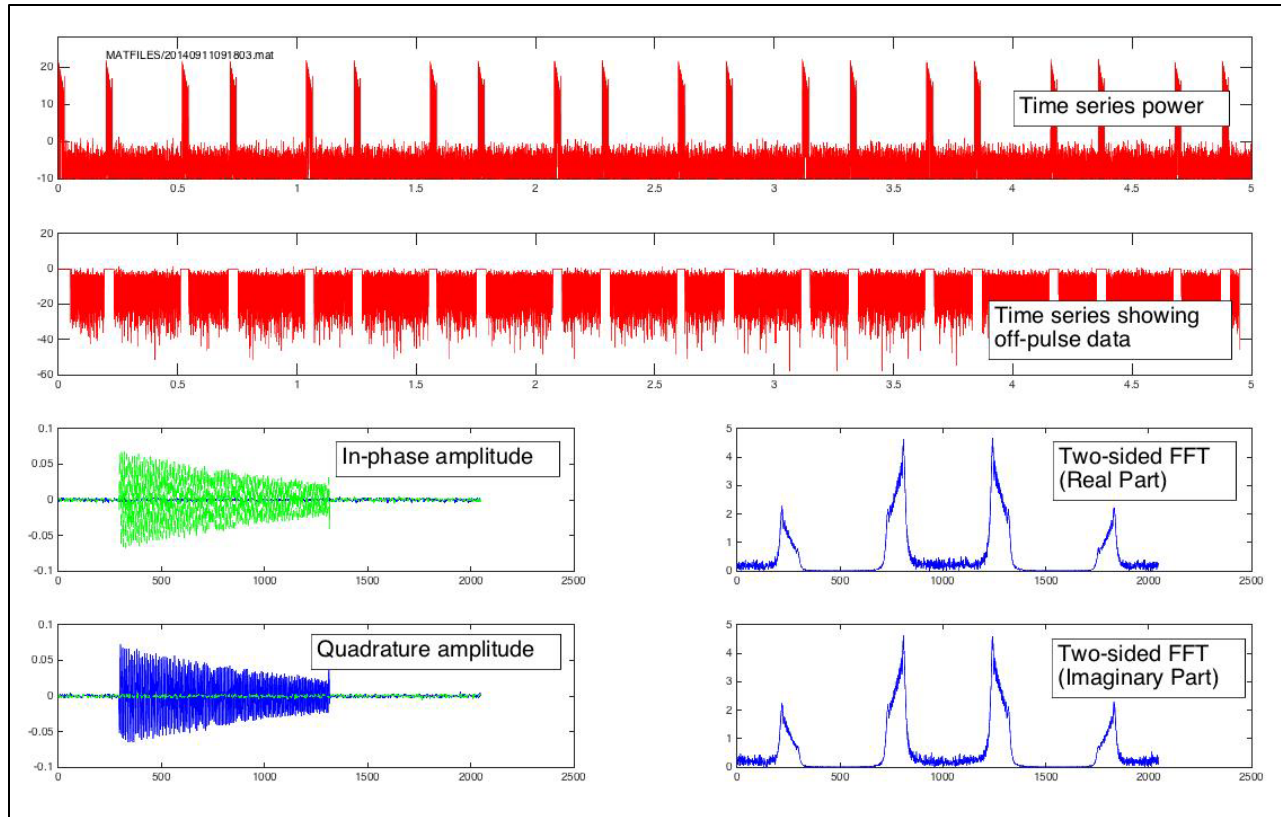
Figure 47. Pulse capture example. Top plot show time series of pulses and their alternate short/long staggers. Next plot shows output of algorithm to separate non-pulse data from pulses. Two lower-left plots are in real-valued in-phase and quadrature components are shown on the right.

A sample of a pulse capture (presumably) of an APAR pulse is shown in Figure 47, which shows the raw data used to construct a time-series that will be shown subsequently. The upper plot in the figure shows the time series of pulses with an apparent staggering such that the separation of the leading edges of the pulses switched (in this instance) back-and-forth from ~0.2 to ~0.3 ms with a pulse length of ~0.03 ms. The next plot shows the post-processing routine's ability to identify the leading and trailing edges of the pulses. The two plots on the lower left show the signal amplitude for in-phase and quadrature data (I&Q) while the two plots on the right show the magnitude-squared for the real and imaginary parts of the FFT (fast Fourier transform).

A range-series of pulse captures for Run # 1 of 11 September 2014 is shown in Figure 48. The figure shows data over the range of 7 to 13 km. The signal contamination is readily apparent—the power observations vary over a range of approximately 10 dB. Over that horizontal region where pulses were obtained (6 to 13 km), the variation in loss that separates standard atmosphere and duct heights of 24 to 28 m for range is very small. Without performing further analysis, it is clear fluctuations in power for the pulse captures, combined with the low sample rate (making mean or medians over short range intervals quite noisy as well) is such that inference of change in propagation loss for range would be unreliable. We hypothesize that a capture system with a sampling rate sufficient to capture all revisits (i.e., all of times when the radar energy is directed

at the target) may yield order statistics (e.g., 80th percentile level values) that have relatively low variance, hence are more suitable for making inference of change in propagation loss with respect to range. That is, however, a hypothesis and not a finding.
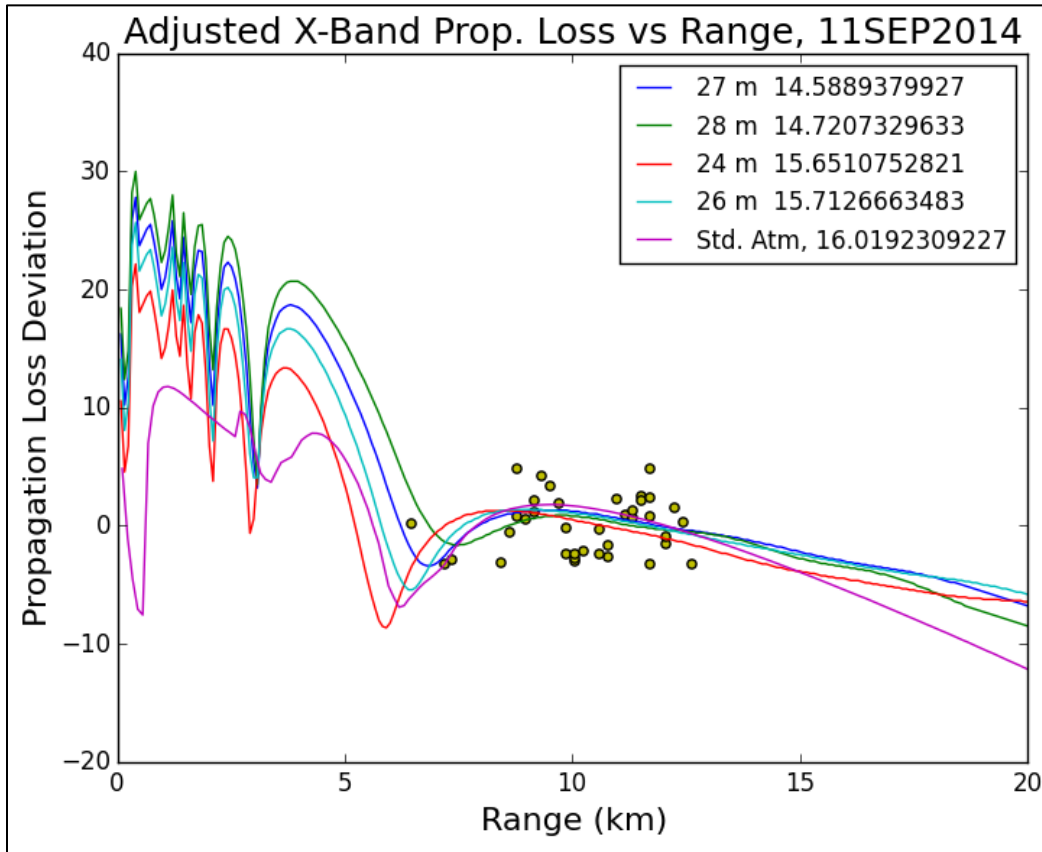
Figure 48. Range series of pulse captures. Pulse captures are shown as dots and modeled negative relative propagation are shown as lines. The mean of the pulse captures is adjusted to match the mean of the relative loss values over the spatial interval where there are pulse captures.

5.4 APAR DATA

As mentioned in Section 2.1.1, one of the parameters recorded by the APAR is the RCS of all targets detected and tracked by the radar. From the fundamental radar equation, the propagation factor, F, can be extracted from the RCS measurements since we know the RCS of the target—namely the FRISC. This will allow us to determine the "goodness" of RF propagation predictions based on in-situ meteorological measurements vs. that from NWP model forecasts. The propagation factor, F, is defined as the ratio of the magnitude of the electric field at a point to the magnitude of the electric field that would occur at the same point in free-space with the beam of the transmitter pointed in the direction of maximum radiation. This quantity in the radar equation contains all the propagation effects induced on the radiated frequency by the natural environment, i.e., the atmospheric and surface conditions along the path.

43

The radar equation for a monostatic radar is defined as

$$SNR \stackrel{\text{def}}{=} \left(\frac{S}{N}\right) = \frac{P_t G^2 \tau \lambda^2 \sigma F^4}{(4\pi)^3 (kT_o) N_f L_s R^4},$$ (1)

where P_t = transmitted power (W),
S = received signal power (W),
N = noise power [at the same receive point as S] (W)
G = antenna gain, here the transmit and receive antennas are assumed equal
(unitless or W/W),
τ = pulse length (sec^{-1})
λ = wavelength (m),
σ = RCS of the target (m^2),
$kT_o = 4 \times 10^{-21}$ W/Hz; noise constant combining Boltzmann's constant (1.38×10^{-23}
W/Hz °K) and a room temperature of 293 °K,
N_f = receiver noise figure (unitless or W/W)
L_s = miscellaneous system losses (unitless or W/W),
R = range (m),
F = propagation factor (unitless).

Generally, the radar-specific quantities are well known and the target RCS and F are known to a much lesser degree. The primary quantity measured by the APAR is the target RCS. However, the internal processing of the radar does not account for atmospheric conditions along the path as this is unknown to the radar. Therefore, the target RCS measured, σ_{APAR}, is an effective RCS with F coupled within the measured quantity. This is given by

$$\sigma_{APAR} = \sigma_{true} F^4,$$ (2)

where σ_{true} is the true, or known, RCS of the target.

Both the Rotte tug and the FRISC were outfitted with corner reflectors and during each day the APAR collected the RCS for each vessel as it rotated for a full 360° within a 3-5 km range from the radar to get a calibrated RCS value and remove any atmospheric effects. The measured RCS is shown in Figure 49 for both the Rotte tug (Figure 49a) and the FRISC (Figure 49b). The RCS is seen to be relatively aspect independent. In dB form, Equation 2 is

$$\sigma_{APAR(dB)} = \sigma_{true(dB)} + 2F_{dB},$$
$$-20 \log F = F_{dB} = 0.5\left(\sigma_{APAR(dB)} - \sigma_{true(dB)}\right).$$ (3)

Here we have specified the definition for the one-way F in dB. From calibrated measurements, $\sigma_{true(dB)}$ for the FRISC is 13 dB. Equation 3 now provides a means to obtain the observed one-way F from the observed APAR radar cross section (RCS) as a function of range.

The APAR antenna location at the LBTS, while very near shore, does have some intervening land between the antenna and the sea surface. This is shown in Figure 50 , where the first 0.8 km of the propagation path is over land. In determining the terrain profile for this portion of the path to properly compute RF predictions, several terrain databases were investigated to get the best

representation possible. One of the features along the path that may induce some terrain effects is the dike marked in the figure. Figure 51 shows the terrain profile for this portion of the path from several terrain databases: (1) DTED (Level 1), (2) SRTM (Level 1), (3) SRTM (Level 2), and (4) ArcGis (http://ahn.maps.arcgis.com/apps/webappviewer/index.html?id=c3c98b8a4ff8 4ff4938fafe7cc106e88). Due to the higher vertical resolution of the ArcGis data, this was the chosen terrain profile for all RF predictions discussed in the next two sections.

The propagation factor was computed using the Advanced Propagation Model (APM) (Barrios, 2003) for all comparisons with observed APAR data shown in the next two sections.
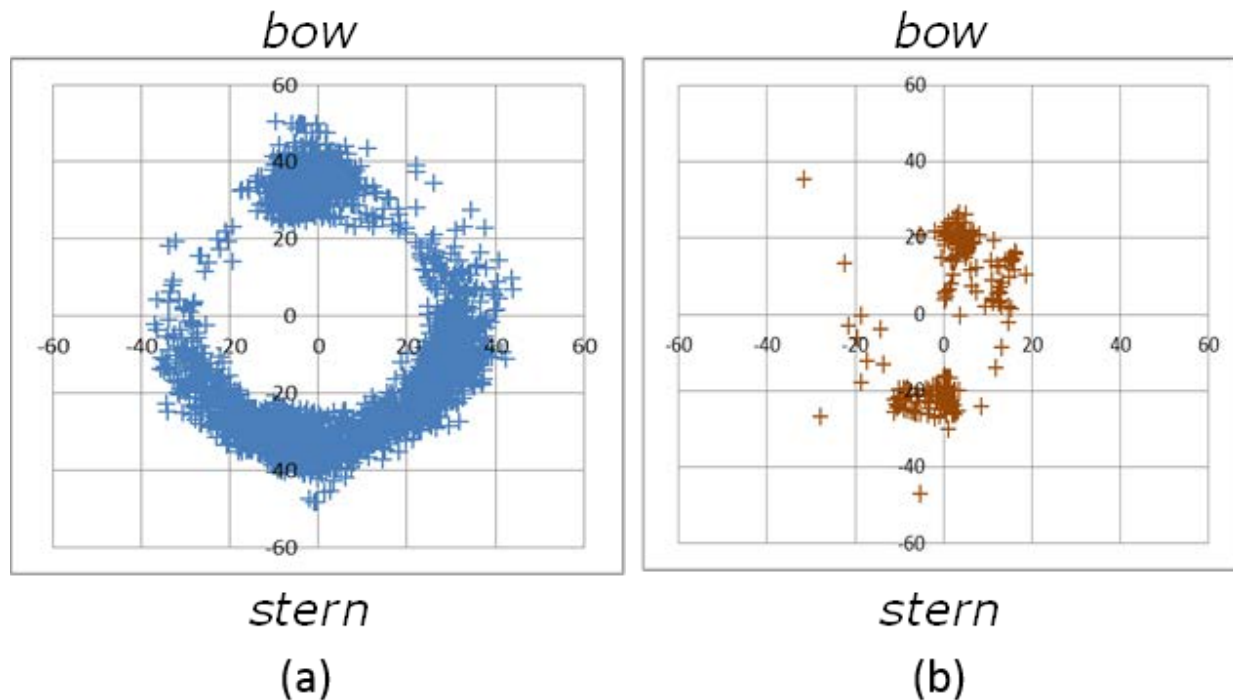
Figure 49. Short-range RCS as a function of azimuth angle of the (a) Rotte tug, and (b) FRISC.
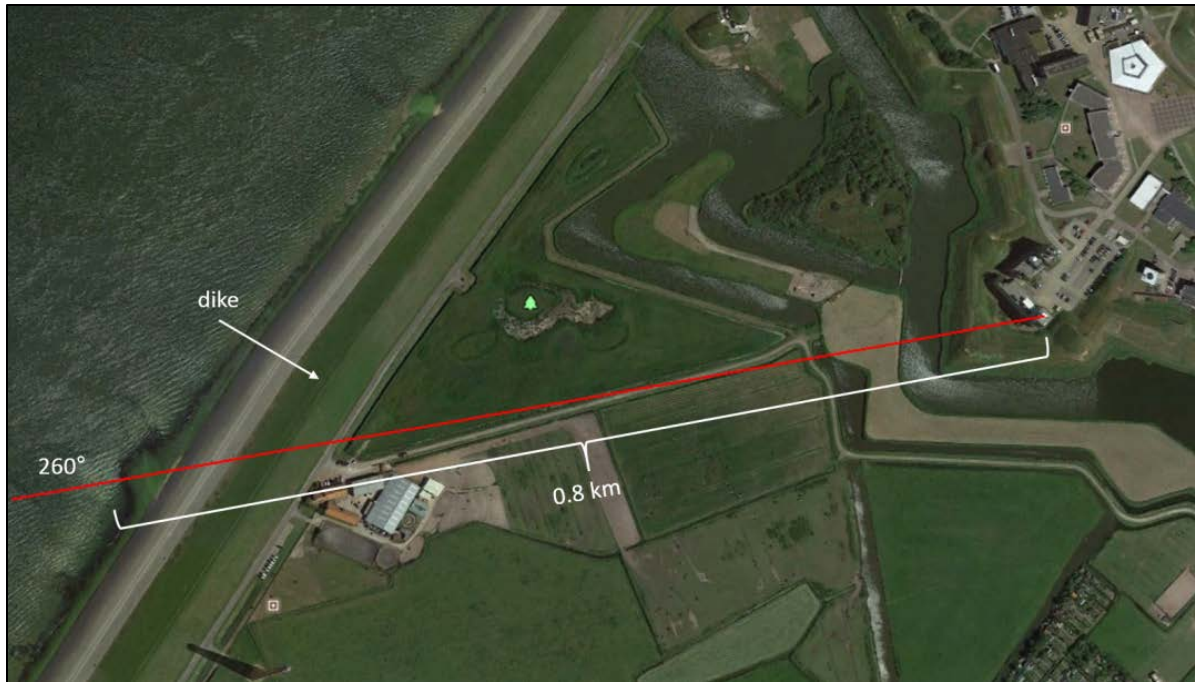
Figure 50. APAR location and 260° sight-line to the shore.
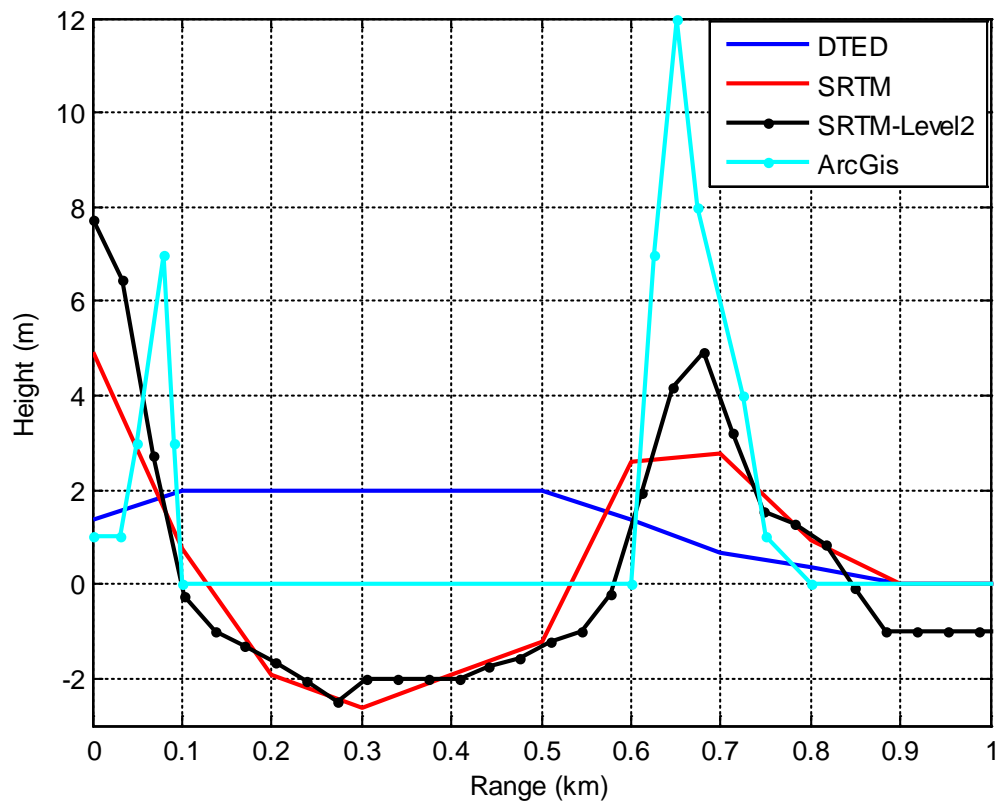
Figure 51. Terrain profile, from the APAR to the shore, from several terrain database sources.

5.4.1 RF Predictions and Observations - NWP Forecasts

Due to the transmitter/target geometries (APAR and FRISC, respectively), all propagation factor predictions were computed based on evaporation duct profiles only, computed from NAVSLaM along the path, with the exception of the first refractivity profile over land, which was based on the vertical pressure, temperature, and humidity profiles forecast by each NWP model. For completeness, all initialization times were also used in the comparisons. The predicted propagation factor at the FRISC target height, nominally 4.0 m, is determined with the APAR transmitting antenna height adjusted for variable tide height.

Using Equation 3, Figures 52 to Figure 59 compare the observed and predicted F, in dB, based on variable evaporation duct profiles from COAMPS (top plot) and HARMONIE (bottom plot) forecast surface parameters for all outbound and inbound runs from 9–12 Sep 2014. The NWP-based predictions shown in the solid red and blue curves refer to the nearest hourly forecast before and after the start time of the FRISC run, respectively, at the 00Z initialization times. NWP-based predictions shown in the dashed red and blue curves refer to the same nearest hourly forecasts but for the nearest following initialization time. There is also a third set of HARMONIE prediction curves for the next initialization time. Shown for reference is predicted F based on standard atmosphere, indicated by the black dotted line. The green dots are the "raw" observed time-sampled data extracted and shown as a function of range. The solid black line represents a 30-point moving average [window] of the raw observations. For all figures shown, the propagation factor predictions include range- and height-varying gaseous attenuation rate profiles based on the ITU model (International telecommunication union-radio communication example) with vertical pressure, temperature, and humidity profiles computed by the NAVSLaM using the NWP surface parameter forecasts.

For 09 Sep 2014 (Figure 52 and Figure 53), all afternoon observations spanned only a portion of the entire 40+ km path as the FRISC was maneuvered to meet the Rotte tug mid-path on this day. Of note is that COAMPS consistently predicts a larger "spread" of F in all runs, compared to the HARMONIE predictions, not only between forecast times but for both initialization times as well. For the outbound run at 1411Z, HARMONIE shows a slight bias in its predictions compared to COAMPS; however, overall both NWP models agree fairly well with observations.

For the four outbound and inbound runs on 10 Sep 2014 (Figure 54 and Figure 55) both COAMPS and HARMONIE predictions generally agreed well with observations with the notable exception of the 0922Z outbound run and the 0812Z inbound run. For the 0812Z inbound run, both NWP models under-predict the propagation factor observed for all but one forecast time: 0900Z from COAMPS and 0800Z from HARMONIE. On the 0922Z outbound run, the HARMONIE-based predictions for all initialization times consistently resulted in lower-than-observed propagation factor values. The noticeable "kink" in the prediction curves near the farthest null is due to a discontinuity between calculation regions within the APM for these particular geometries at these times.

The outbound and inbound runs for 11 Sep 2014 are shown in Figure 56 and Figure 57. For all five runs during this day, both COAMPS and HARMONIE show excellent agreement with the observed F. The "spike" in the smoothed (observed) curve (at roughly 31 km) in the 0924Z outbound run is due to a large RCS/F value resulting from the FRISC maneuvering near a

navigation buoy on its outbound trajectory. Throughout much of the runs there is sparse data for ranges less than 10 km due to the FRISC maneuvering outside the FoV of the radar.

Figure 58 and Figure 59 show the final two outbound and inbound runs for 12 Sep 2014. The first inbound and final outbound runs were shortened due to the FRISC not completing the full run but meeting the Rotte tug at the mid-path point. Missing data from approximately 4 to10 km on the final inbound run was again due to the FRISC maneuvering outside the FoV of the radar. For the majority of the runs, predictions using both NWP models were consistent in over-predicting F at the farthest ranges, except for a few isolated forecast times (0900Z COAMPS-based predictions for the 0810Z inbound and 0827Z outbound runs, and the 0700Z HARMONIE-based predictions for the 0733Z outbound run).

Figure 52. Predicted vs. measured propagation factor for all outbound runs on 9 Sep 2014.
Predictions based on (a) COAMPS, and (b) HARMONIE forecasts.

Figure 53. Predicted vs. measured propagation factor for all inbound runs on 9 Sep 2014. Predictions based on (a) COAMPS, and (b) HARMONIE forecasts.

Figure 54. Predicted vs. measured propagation factor for all outbound runs on 10 Sep 2014. Predictions based on (a) COAMPS, and (b) HARMONIE forecasts.

Figure 55. Predicted vs. measured propagation factor for all inbound runs on 10 Sep 2014. Predictions based on (a) COAMPS, and (b) HARMONIE forecasts.
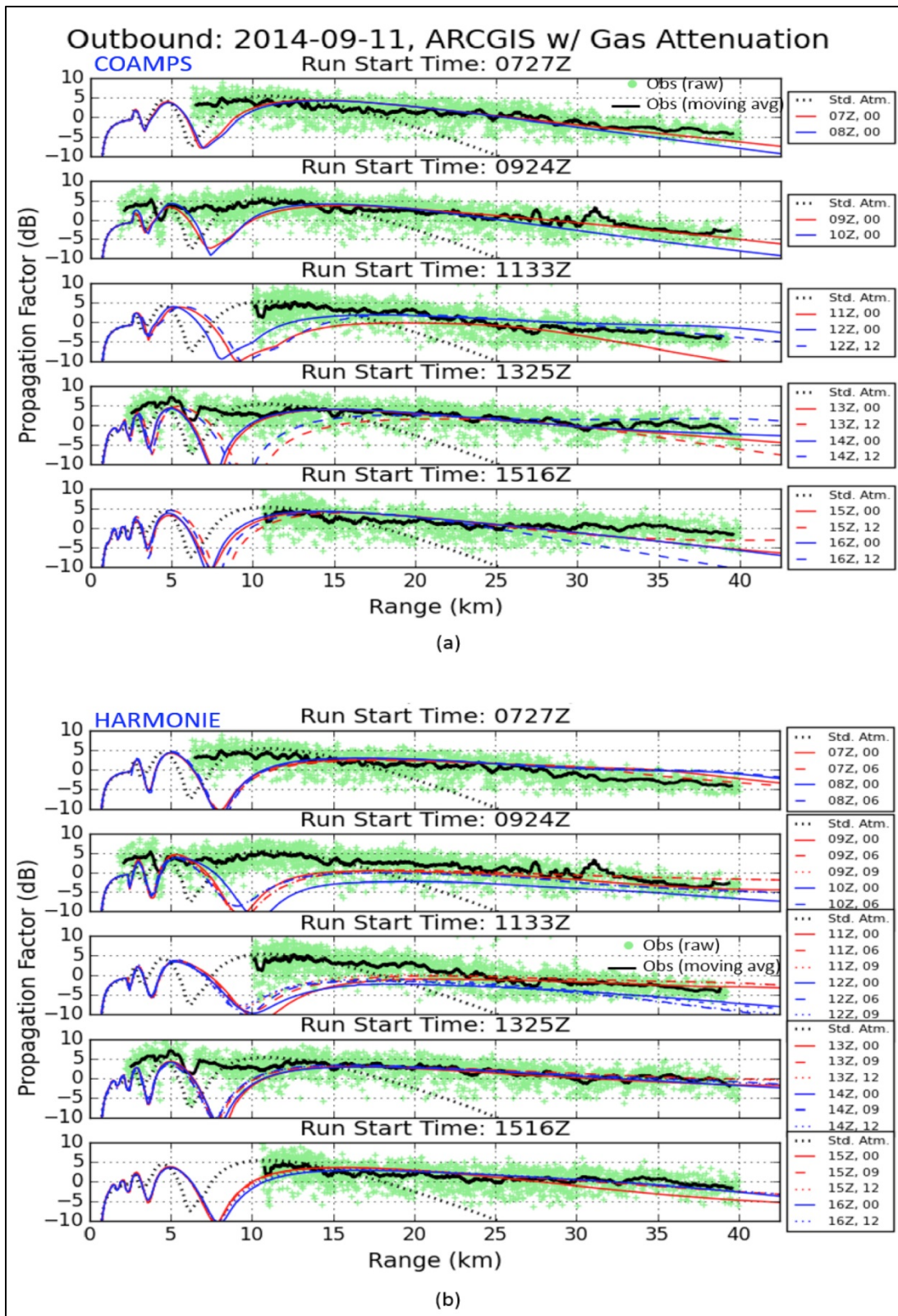
Figure 56. Predicted vs. measured propagation factor for all outbound runs on 11 Sep 2014. Predictions based on (a) COAMPS, and (b) HARMONIE forecasts.
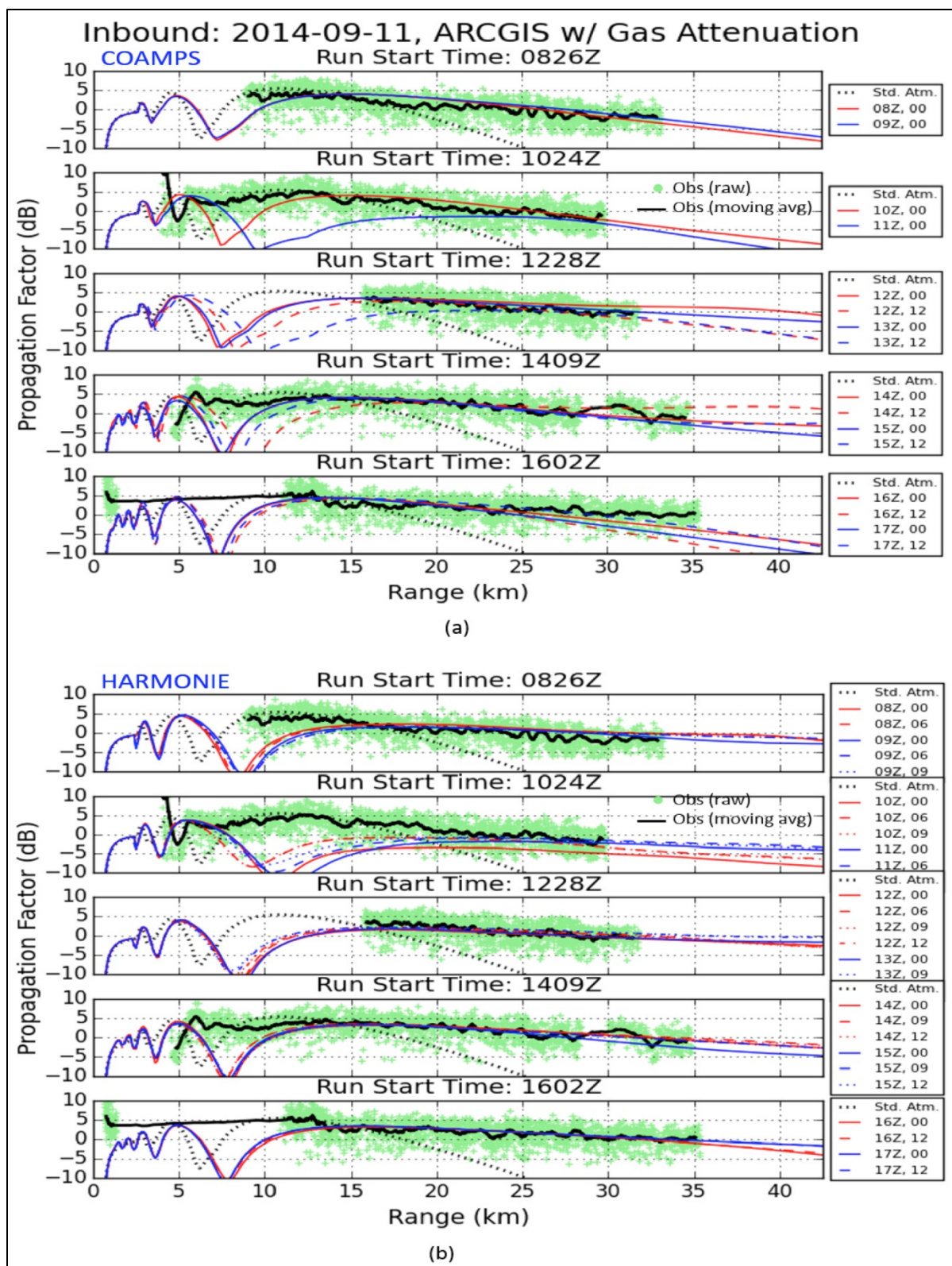
Figure 57. Predicted vs. measured propagation factor for all inbound runs on 11 Sep 2014. Predictions based on (a) COAMPS, and (b) HARMONIE forecasts.
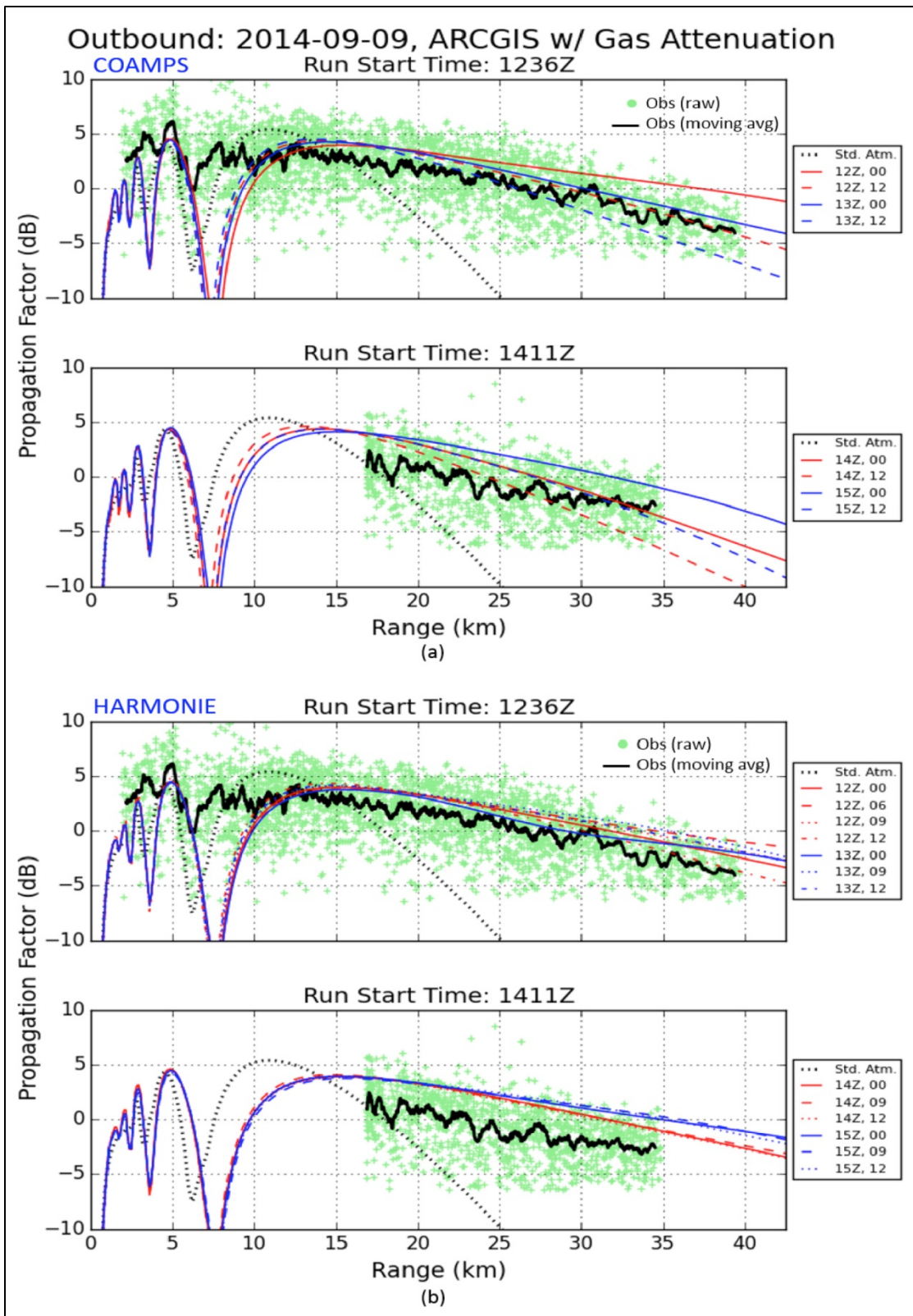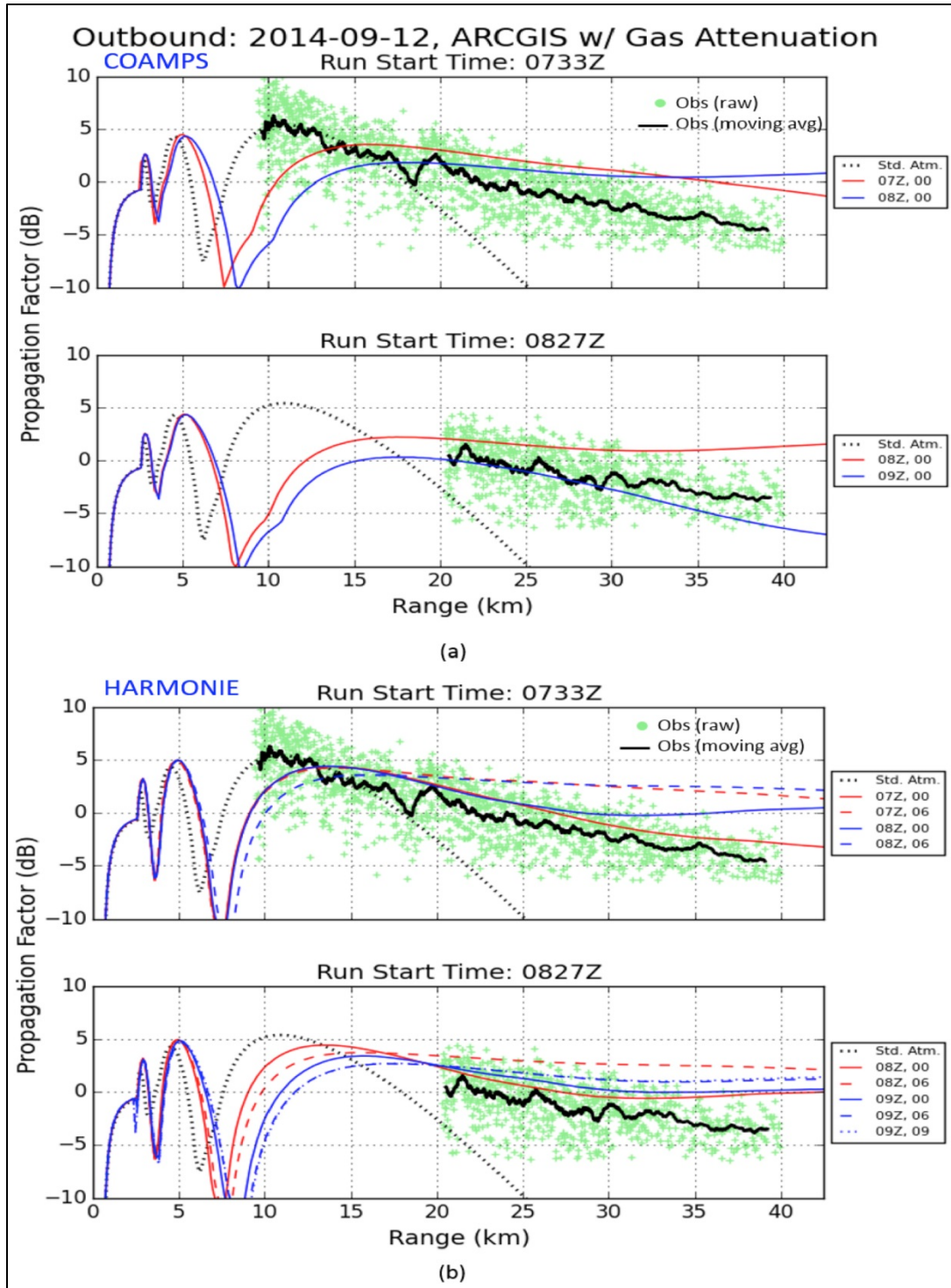
Figure 58. Predicted vs. measured propagation factor for all outbound runs on 12 Sep 2014. Predictions based on (a) COAMPS, and (b) HARMONIE forecasts.
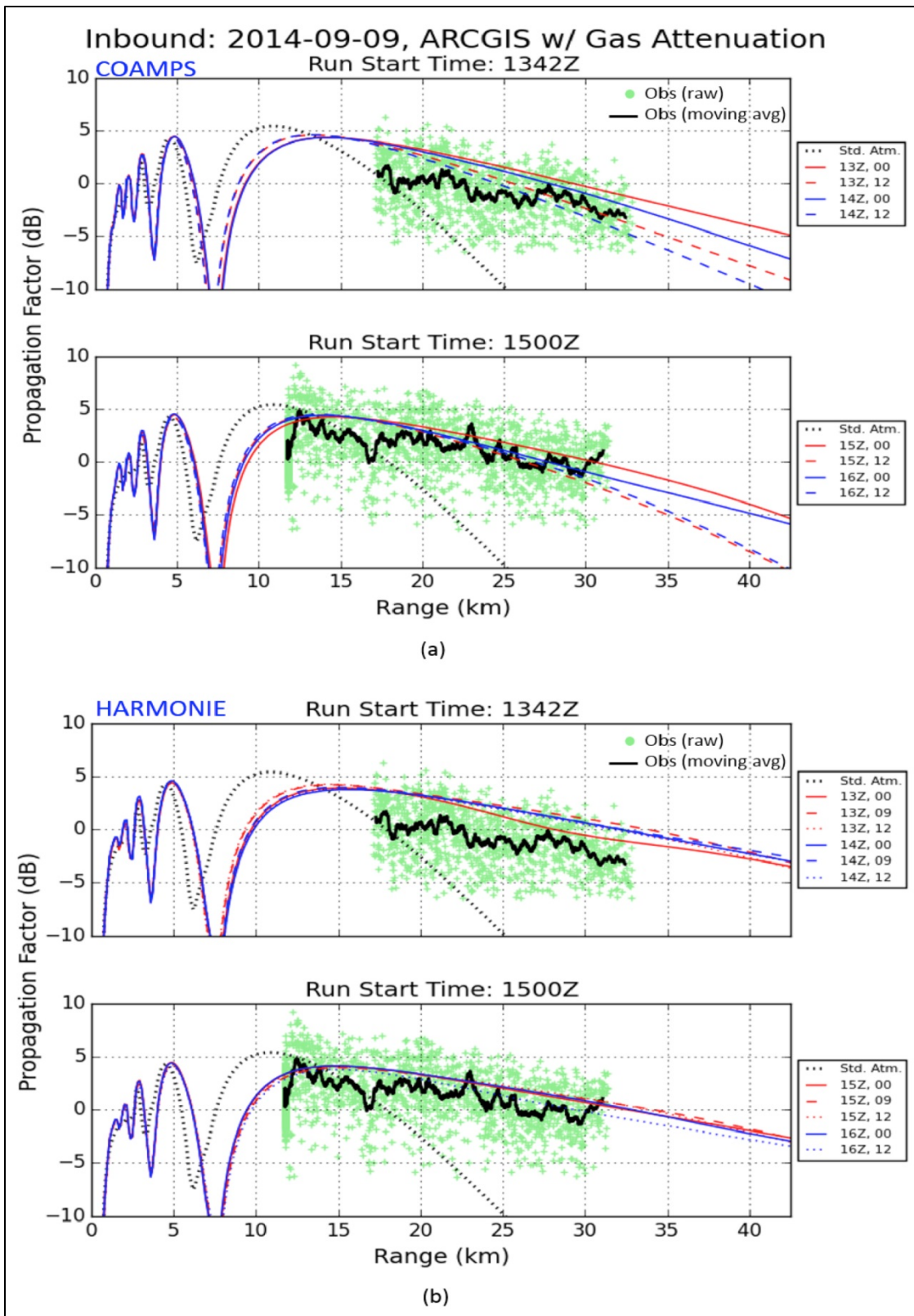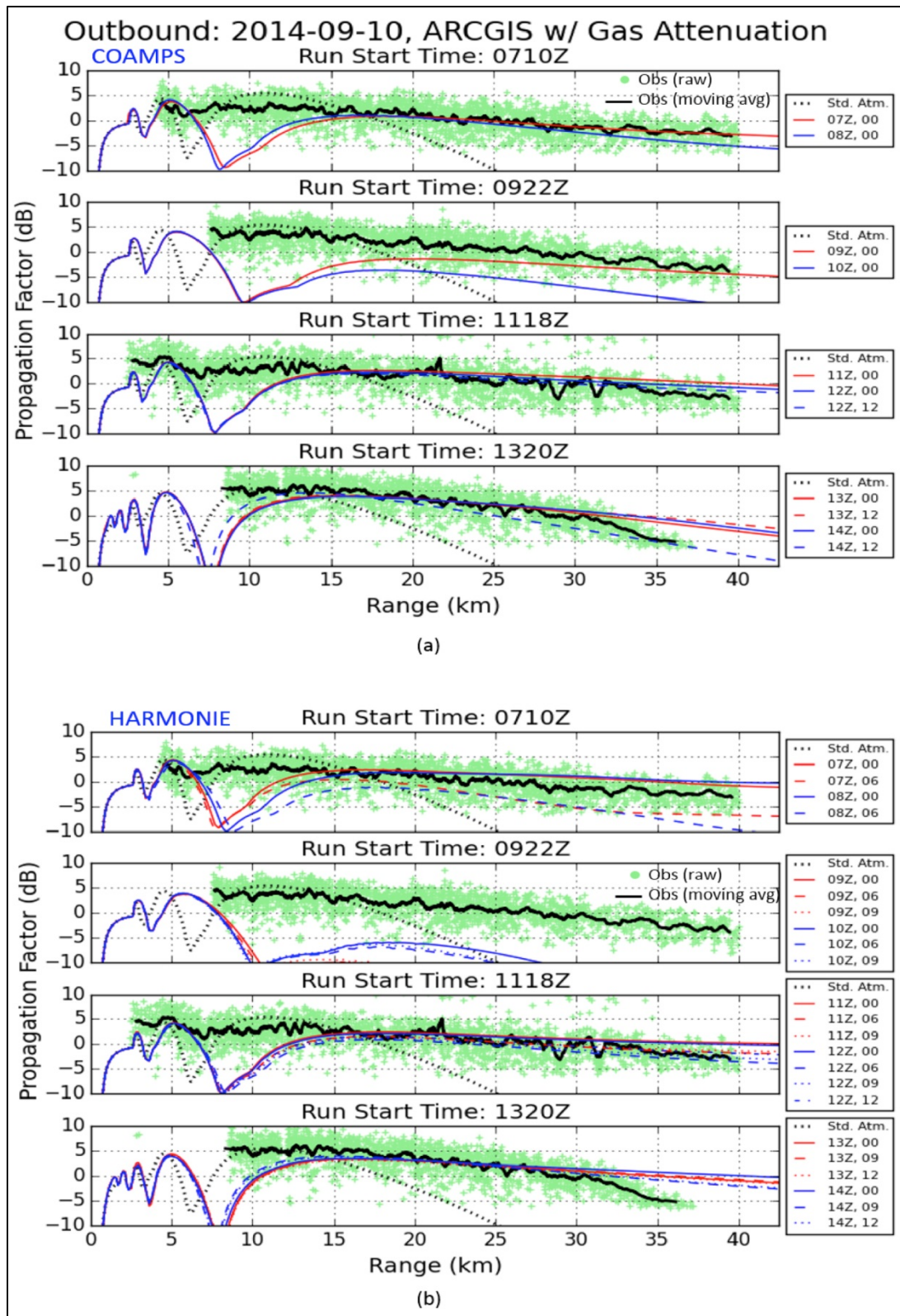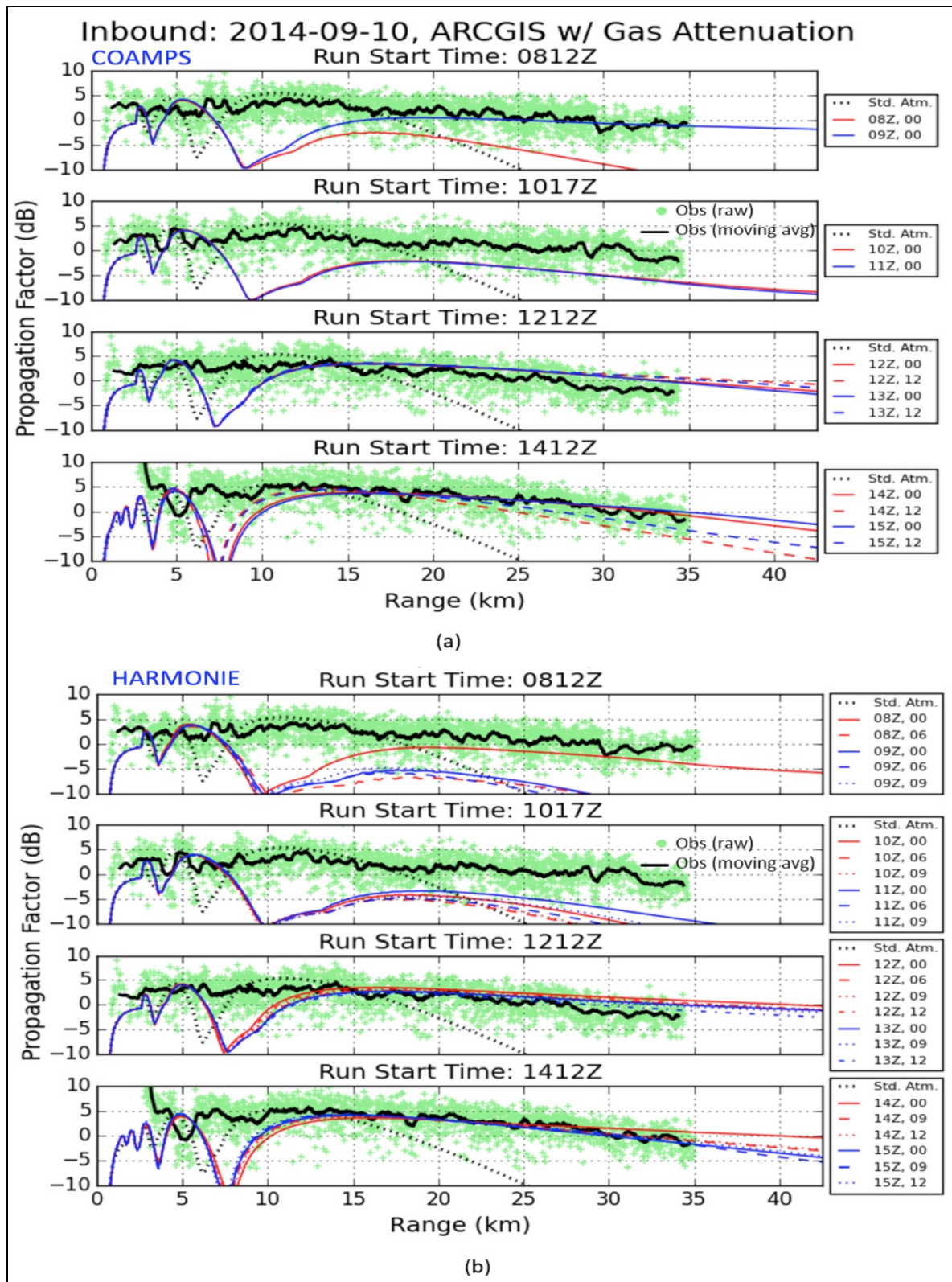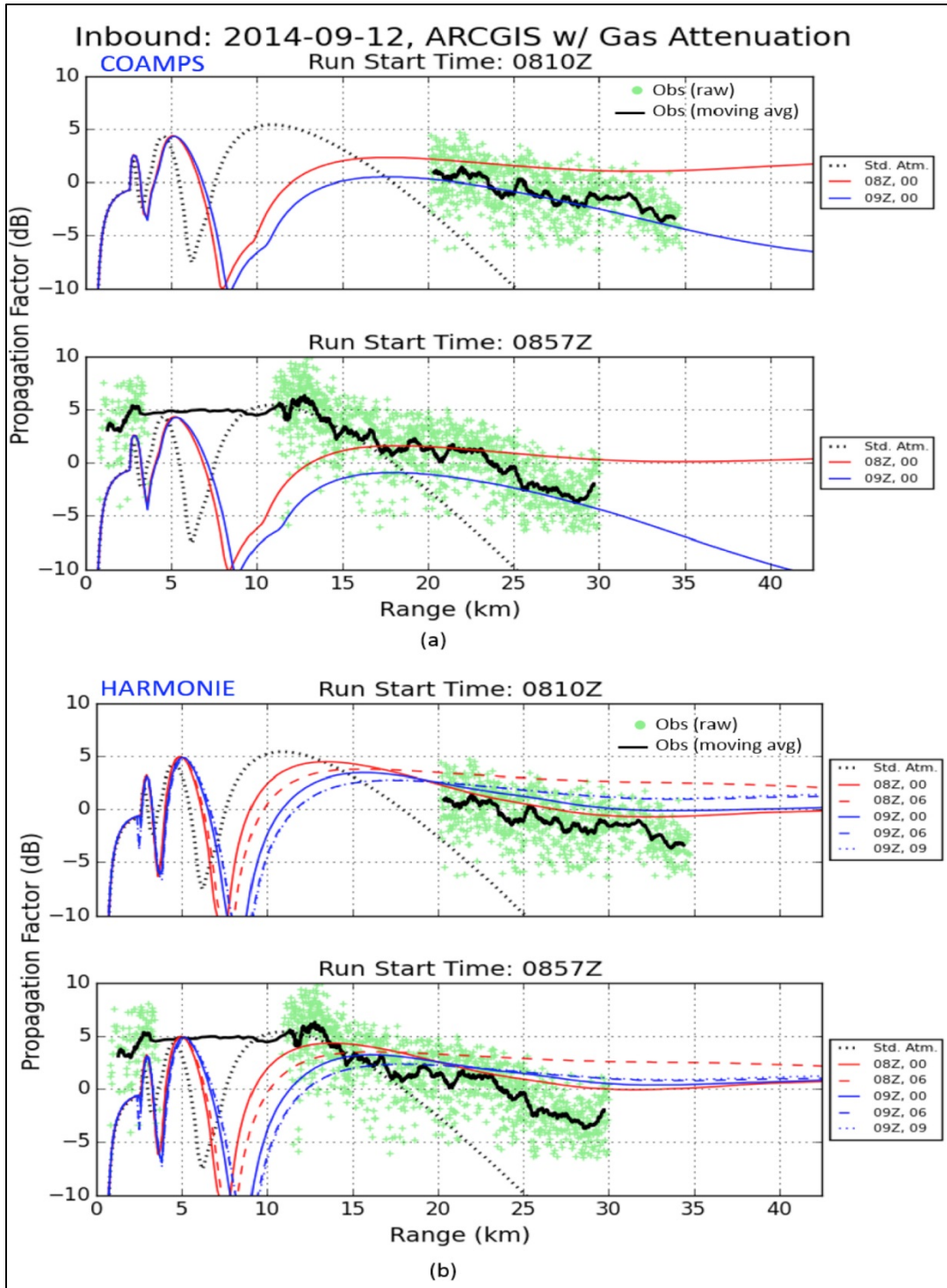
Figure 59. Predicted vs. measured propagation factor for all inbound runs on 12 Sep 2014. Predictions based on (a) COAMPS, and (b) HARMONIE forecasts.

5.4.2 RF Predictions and Observations – In-situ Measurements

Propagation factor predictions presented here are based on in-situ measurements using both radiosonde data and surface "bulk" observations. When treating the in-situ data we must take into account several considerations. Unlike the rigid structure of the NWP data, since the tug is a moving platform we did not collect data which is uniform along the path in time and space. Possibly due to sensor placement and the wake of the ship, there are some irregularities with the tug TACMET data. Shown in Figures 39 to 42, spikes in recorded temperature seem to be concurrent with sonde launches during which the ship remained stationary. Wind speed is "course-estimated" since no heading data was recorded from the tug. This results in decreased accuracy especially at slow speeds, where the relative wind across the sensor is no longer dominated by the ship's movement. Note that for 11 Sep 2014 the shore-side ASTD indicates stable conditions, which is consistent with warm off-shore flow due to the NW winds present that day.

For each prediction we identified those TACMET and radiosonde times that "frame" the FRISC run. Assumptions made in our initial treatment were as follows:

1. Within a certain time frame (~1 h), we assume that within a small spatial region along the propagation path that the surface and upper-air meteorology remain relatively unchanged; we then treat data separated both spatially and temporally that are within tolerances as simultaneous measurements for entry into the APM; (As was done in the previous section, only evaporation duct profile(s) are applied on the over-water portion of the propagation path due to the low-altitude geometries.)
2. Calculated wind, though course-estimated, is taken as true wind speed and taken from 10-min average values
3. Although the shore-side radiosonde launch location is not along the 260° radial, we've applied the refractivity profile determined from the upper air sounding at the same location as the APAR.

In determining refractive profiles for input into the APM, three profiles are determined along the propagation path. For each set of range-dependent environments, the profiles are determined as follows:

1. The first profile is placed at the APAR site (range 0.0 km) and is determined from the shore-side radiosonde observations
2. The second profile is placed at the shoreline (range 0.8 km from the APAR), and is the evaporation duct profile computed by NAVSLaM using the shore-side TACMET surface observations coupled with the climatology-based SST; the TACMET sensor heights in this case are adjusted for tide height; the time stamp of the TACMET surface measurements correspond to the FRISC start time for all outbound runs; (for all inbound runs the time stamp corresponds to the end of the FRISC run.)
3. The third profile is placed at the tug site and is the evaporation duct profile based on surface layer observations by the TACMET on board the Rotte tug; the time stamp of the surface measurements correspond to the middle of the FRISC run, with the SST values determined by linear interpolation of the bucket measurements; the range which defines the "tug site" is based on the tug location at the same time; (The refractivity is assumed homogeneous beyond the range of the tug).

Radiosonde observations (identified by radiosonde launch times), the evaporation duct height (EDH) computed from both shore and tug TACMET data, along with the tug ranges, are provided in Table 7. All evaporation duct profiles computed are shown in Figures A-27 to A-34. We place a caveat for the evaporation duct profiles on 12 Sep 2014. Due to the lack of shore-side TACMET data for this day, the refractivity profile is assumed homogeneous for the entire over-water portion of the path and is based on the TACMET data from the tug. All radiosonde observations are those taken from the descent profile, except where noted.

Table 7. Radiosonde launch times, EDHs, and third-profile ranges used in defining the in-situ range-dependent environments.

Day	FRISC Start Time (UTC)	Shore Sonde (UTC)	Shore EDH (m)	Tug EDH (m)	Tug Range (km)
9 Sep	12:36	13:12[1]	8.4	9.4	23.1
	13:42	13:50	8.8	8.8	16.7
	14:11	13:50	8.6	8.6	21.1
	15:00	14:36	8.6	10.4	14.0
10 Sep	07:10	07:10	9.4	11.8	6.3
	08:12	07:10	10.4	11.4	12.0
	09:22	09:44[1]	9.4	10.8	24.4
	10:17	09:44[1]	16.6	11.0	14.5
	11:18	10:58[1]	21.4	10.4	21.0
	12:12	12:15[1]	9.0	10.6	25.3
	13:20	12:15[1]	8.2	11.0	12.9
	14:12	13:29[1]	10.0	10.6	6.0
11 Sep	07:27	07:13	7.0	9.6	10.2
	08:26	08:29	12.6	5.2	11.7
	09:24	09:35[1]	14.0	8.8	23.8
	10:24	10:28[1]	16.4	8.8	23.0
	11:33	11:14	11.2	9.6	22.4
	12:28	12:18	14.6	10.6	23.2
	13:25	13:01	15.0	11.4	20.9
	14:09	13:45[1]	17.6	13.2	25.4
	15:16	15:17	15.0	13.8	23.3
	16:02	16:13	13.2	12.4	22.8
12 Sep	07:33	07:01	-	7.6	See note 2
	08:10	08:03	-	8.4	
	08:27	08:03	-	8.4	
	08:57	08:46	-	8.2	

[1] Ascent profile only is available for this time.
[2] The ED refractivity profile is assumed homogeneous from the shoreline.

Figures 60 to 67 show the observed and predicted *F*, based on the range-dependent environments listed above for each FRISC run. Similar to Section 5.4.1, "raw" APAR measurements are indicated by green dots and the corresponding 30-point moving average (window) is indicated by the solid black line. At first glance, the results show favorable agreement with observations and appear to be very similar than those based on the NWP models.

Figure 60. Predicted vs. measured propagation factor for all outbound runs on 9 Sep 2014. Predictions based on radiosonde and evaporation duct profiles referenced in Table 7.

Figure 61. Predicted vs. measured propagation factor for all inbound runs on 9 Sep 2014. Predictions based on radiosonde and evaporation duct profiles referenced in Table 7.
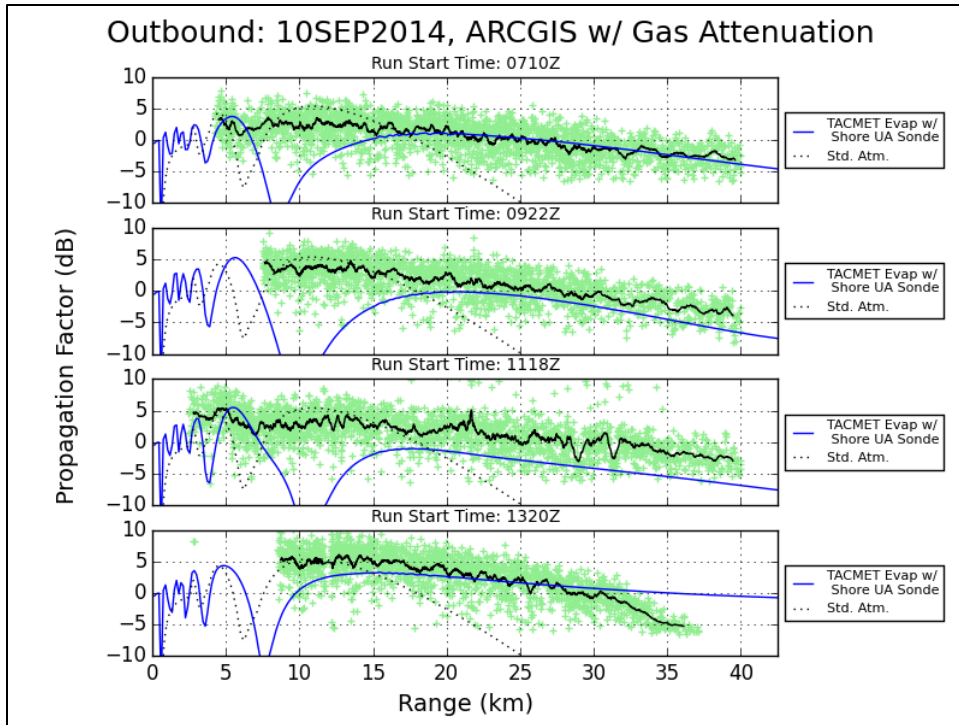
Figure 62. Predicted vs. measured propagation factor for all outbound runs on 10 Sep 2014. Predictions based on radiosonde and evaporation duct profiles referenced in Table 7.
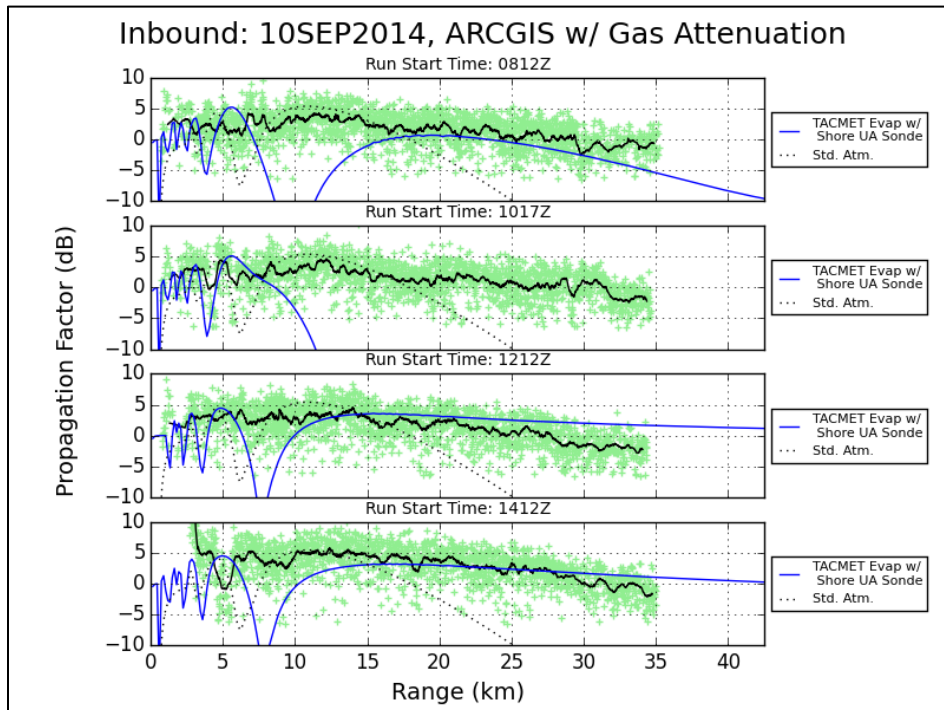
Figure 63. Predicted vs. measured propagation factor for all inbound runs on 10 Sep 2014. Predictions based on radiosonde and evaporation duct profiles referenced in Table 7.
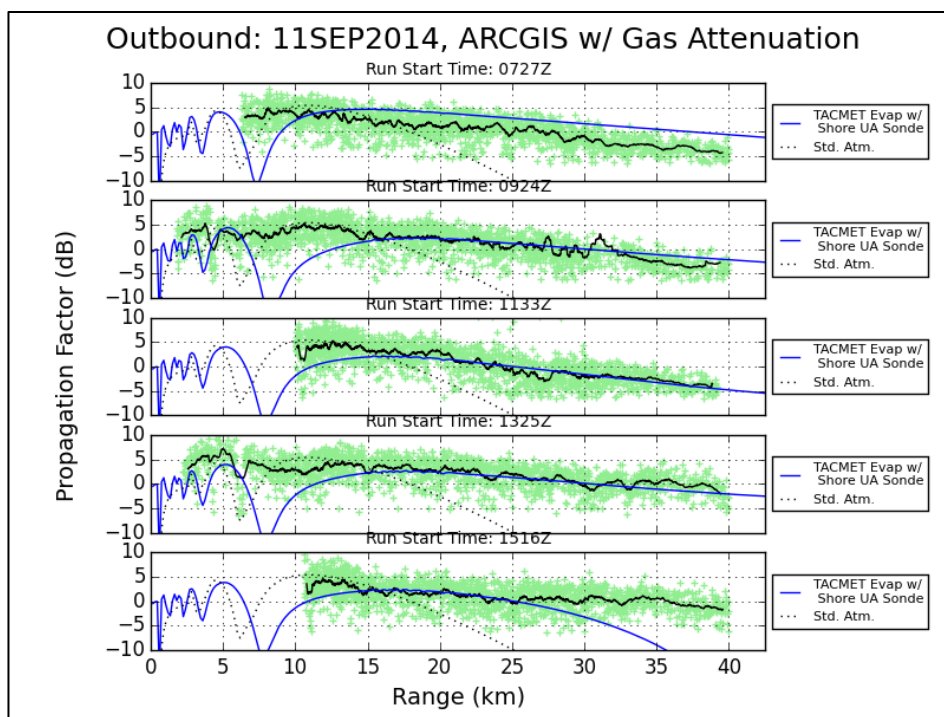
Figure 64. Predicted vs. measured propagation factor for all outbound runs on 11 Sep 2014. Predictions based on radiosonde and evaporation duct profiles referenced in Table 7.
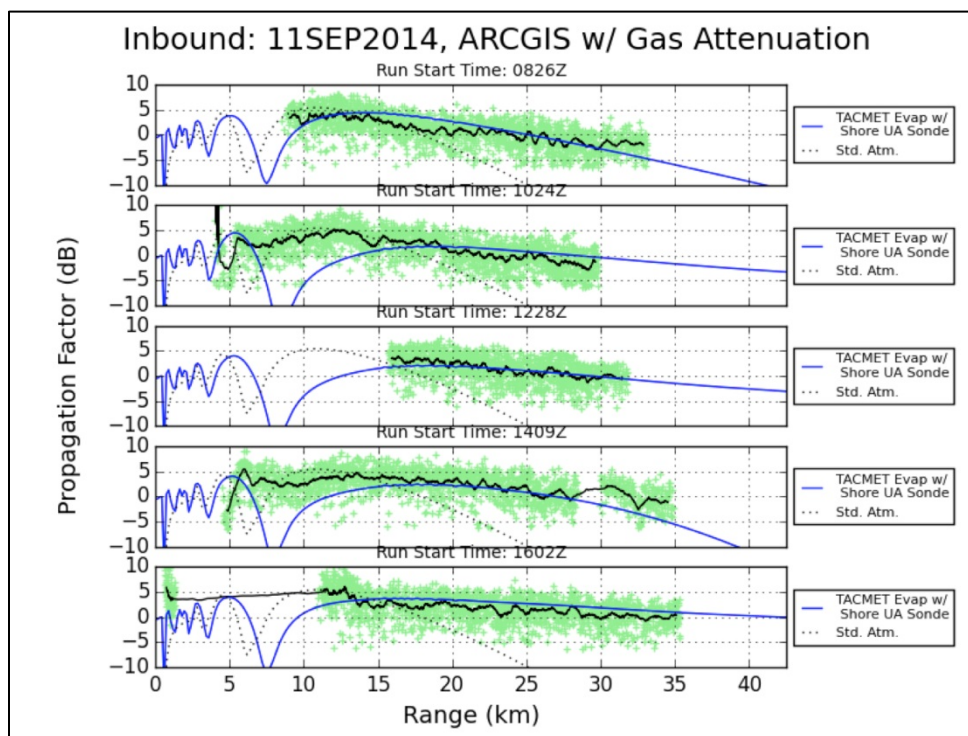
Figure 65. Predicted vs. measured propagation factor for all inbound runs on 11 Sep 2014. Predictions based on radiosonde and evaporation duct profiles referenced in Table 7.
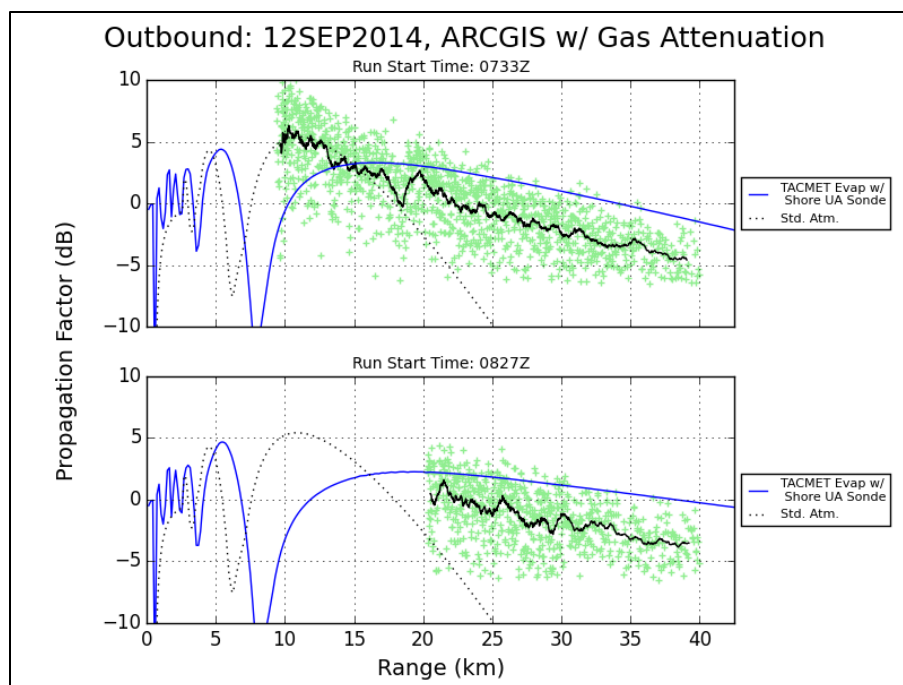
Figure 66. Predicted vs. measured propagation factor for all outbound runs on 12 Sep 2014. Predictions based on radiosonde and evaporation duct profiles referenced in Table 7.
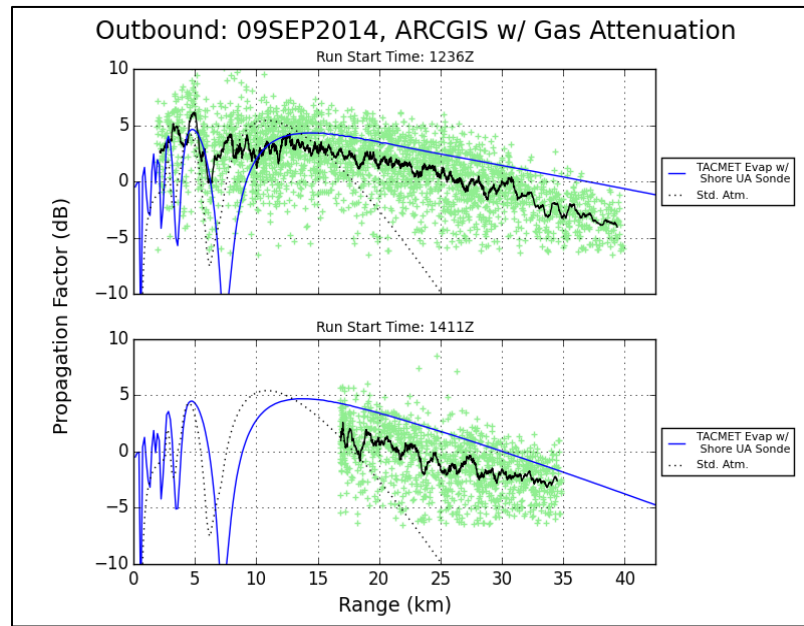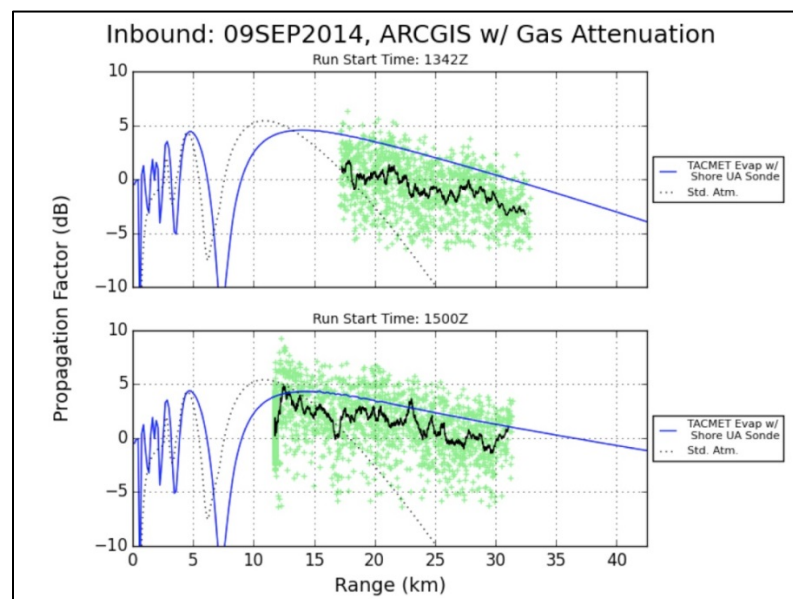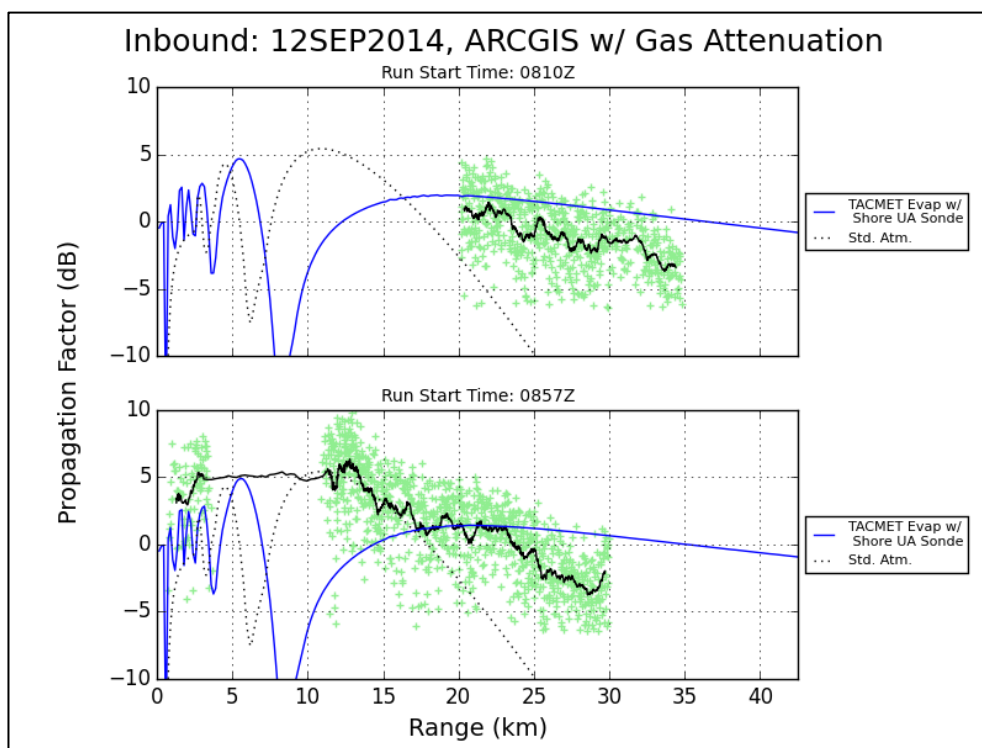

Figure 67. Predicted vs. measured propagation factor for all inbound runs on 12 Sep 2014. Predictions based on radiosonde and evaporation duct profiles referenced in Table 7.

A notable discrepancy is the 10 Sep 2014 inbound run at 1017Z. Although this particular run was also problematic for the NWP models, the difference is much greater here. For 12 Sep 2014, the predictions show a consistent positive bias: however, this may be due to the "ad hoc" assumption of a homogeneous environment for the over-water portion of the path.

A closer look at the propagation conditions for the 10 Sep 2014, 1017Z event highlight the deep horizontal null induced by the evaporation ducts during this time. This is shown in Figure 68. The coverage diagram (top plot) illustrates the overall effect of the evaporation duct conditions present where low loss (extended range) is evident at very low altitudes. The dashed black line indicates the target height (height of the corner reflector) of the FRISC, which happens to fall directly within the horizontal null induced by the evaporation ducts. The bottom plot displays the propagation factor as a function of range at the target height and the target height ±1.0 m. The green curve is identical to the blue curve in Figure 63 (second graphic from the top). In Figure 68(b), the vertical scale extends down to -30 dB, showcasing the variability of the propagation factor immediately above and below the initial target height of 4.0 m. In some regions the propagation factor can vary as much as 20 dB or more.
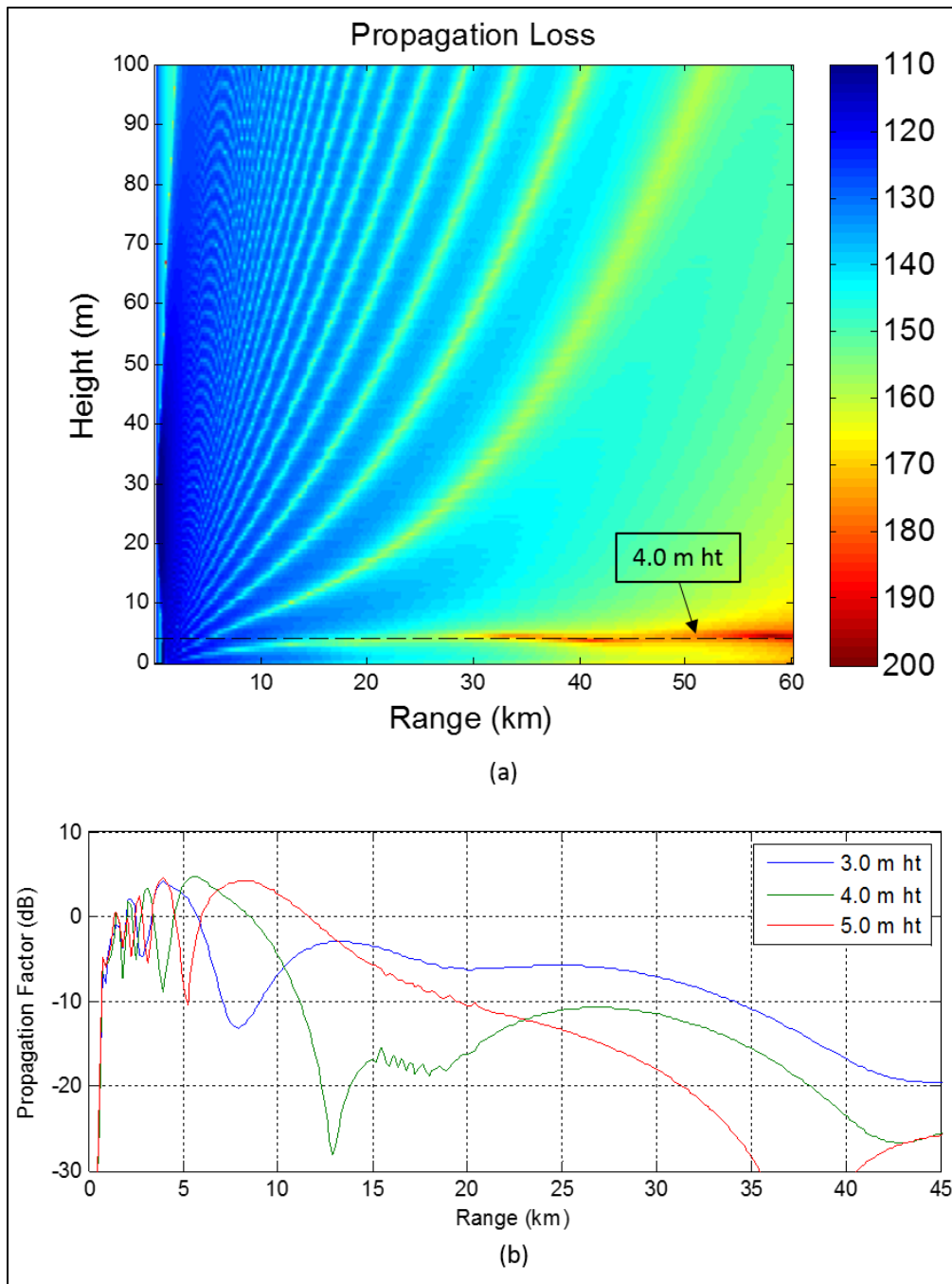
Figure 68. 10 Sep 2014 1017Z event illustrating (a) a coverage diagram of propagation loss with the dashed line indicating the FRISC target height, and (b) propagation factor vs. range at the FRISC target height (4.0 m) ±1.0 m.

6. DISCUSSION

One basic metric for quantifying the differences between RF predictions and actual measurements is the root mean square error (RMSE), defined by

$$RMSE = \sqrt{\frac{1}{n}\sum_{i=1}^{n}\left[F_o(i) - F_p(i)\right]^2},$$ (4)

where n is the number of samples, F_o is the observed propagation factor and F_p is the predicted. While the *RMSE* can provide a basic metric for the quality of model predictions against sampled data, it is not by itself, a sufficient metric.

While predicted *F*, shown in Sections 5.4.1 and 5.4.2, includes effects from gaseous attenuation, we expected very little contribution from gaseous absorption in the overall propagation factor, as the attenuation rate for X-band typically did not exceed 0.02 dB/km. A comparison of RMSE with and without accounting for gaseous attenuation is shown in Figure 69 for both COAMPS and HARMONIE predictions. For RMSE values between 2 to 6 dB, both NWP models produce slightly lower RMSE when considering gaseous absorption: however, the overall RMSE difference between accounting for and neglecting gaseous attenuation is negligible. Nevertheless, all metrics provided below are based on predictions that account for gaseous absorption along the propagation path.
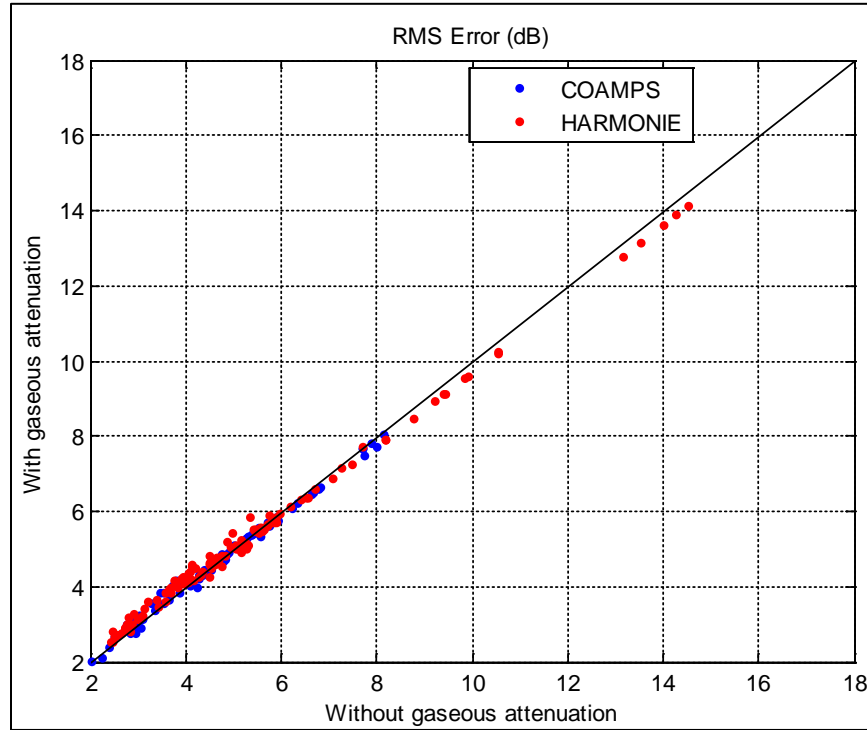
Figure 69. COAMPS and HARMONIE RMSE with and without gaseous attenuation.

6.1 NWP-BASED RF PERFORMANCE

A histogram of the RMSE from all predictions based on COAMPS and HARMONIE, for all forecast and initialization times shown in Figures 52 to 59 are compared in Figure 70. The RMSE values were determined based on the time-averaged (moving window) observations. The median RMSE from both NWP models are similar, at 3.2 dB for COAMPS and 3.6 dB for HARMONIE. Also shown is the histogram of the RMSE based on standard atmosphere (bottom plot), where the median RMSE is 11.6 dB—more than three times that of RF results based on either NWP model. It is clear that the basic assumption of standard atmosphere conditions results in the largest error when compared to observations. Of note is that while the largest RMSE value from COAMPS is more than 7+ dB, some HARMONIE predictions resulted in RMSE values of as much as 13 to 14 dB. However, a larger set of predictions based on HARMONIE environments were available due to more HARMONIE forecasts and initialization times generated.
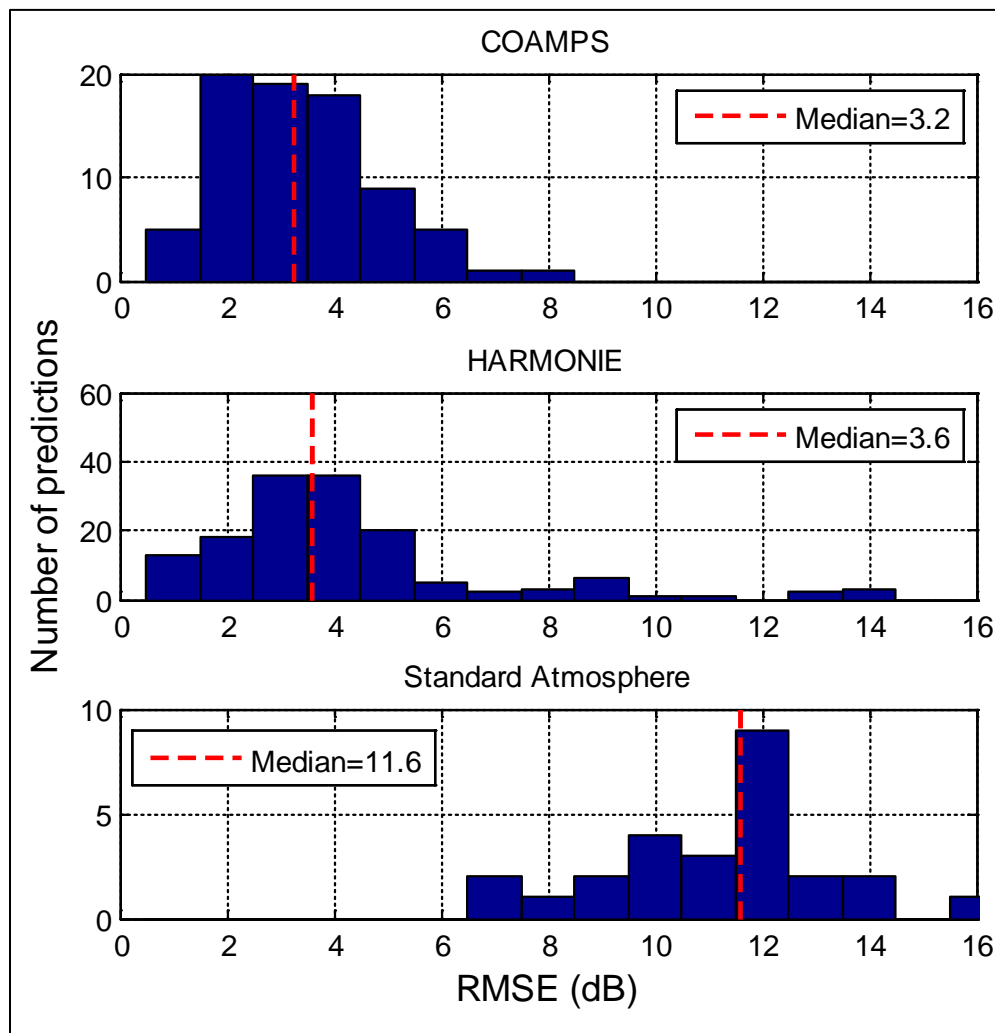
Figure 70. Histograms of RMSE (moving average of observed and the APM) based on COAMPS, HARMONIE, and standard atmosphere conditions, where all forecast and initialization times were included for each NWP model.

When using NWP forecasts to determine RF performance, the nearest initialization time is always desired due to forecasts being produced with initial boundary conditions (within the NWP model[s]) based on the nearest temporal real-world data. Focusing on only those forecast and nearest-initialization times for each NWP model, the RMSE for each outbound and inbound run for all days are shown in Figures 71 and 74. The specific forecast time (prior and following each FRISC run) as well as initialization times for each run start time for all days are provided in Table A-1 in Appendix A.

In Figure 71, all runs were conducted in the afternoon (UTC) on 9 Sep 2014; therefore, all COAMPS and HARMONIE forecasts shown are based on 12Z initialization times. For each run, the RMSE for the nearest hourly forecast prior and following the FRISC start time are presented. Standard atmosphere is also included, and duplicated for each forecast time within a graphic, for comparison. Results from both COAMPS and HARMONIE were comparable and provided extremely good comparisons with observed data. HARMONIE produced slightly higher RMSE values for the inbound 1342Z and outbound 1411Z runs, but differences were within 1.2 dB.

Figure 71. RMSE for all runs on 10 Sep 2014, of observed vs. predicted propagation factor based on COAMPS, HARMONIE, and standard atmosphere environments. Nearest temporal initialization and forecast times are used for the NWP environments.

For 10 Sep 2014 (Figure 72) both COAMPS- and HARMONIE-based results were comparable and produced low RMSE, except for the first and second inbound runs, 0812Z and 1017Z, respectively, as well as the second outbound run (0922Z). For these runs, propagation results from both NWP models produced RMSE values greater than 5 dB, with HARMONIE producing results where the RMSE exceeded that of standard atmosphere conditions for the 0922Z run.

Figure 72. RMSE for all runs on 11 Sep 2014, of observed vs. predicted propagation factor based on COAMPS, HARMONIE, and standard atmosphere environments. Nearest temporal initialization and forecast times are used for the NWP environments.

Figure 73 displays the RMSE results for all runs on 11 Sep 2014. Propagation factor predictions based on COAMPS and HARMONIE show excellent agreement for all runs, the majority resulting in a RMSE value of 5 dB or less. The exception is for inbound run 1024Z, where the RMSE is greater than 5 dB (for both NWP models) for the 1100Z forecast time. Of note is that for most of the morning runs, COAMPS-based propagation predictions produced lower RMSE values than those

from HARMONIE; however, for the afternoon runs, the reverse is true. HARMONIE-based propagation predictions provided lower RMSE values than that from COAMPS. For the afternoon runs, predictions from both models are using the same initialization time of 12Z.
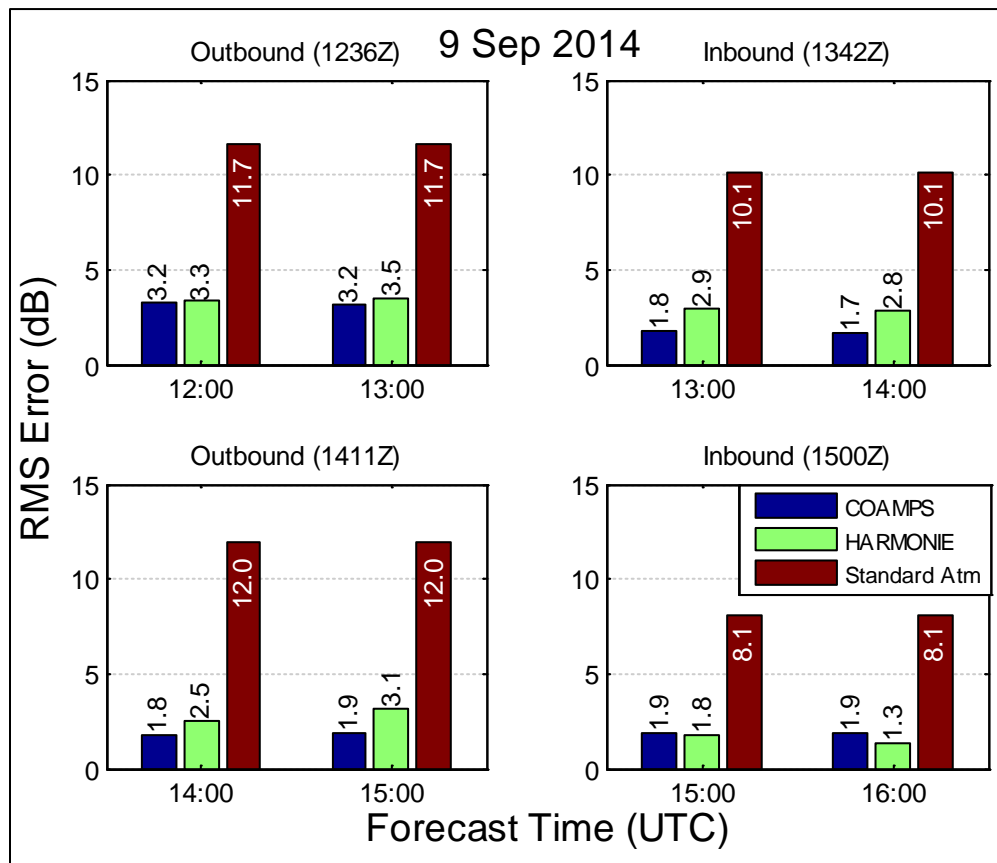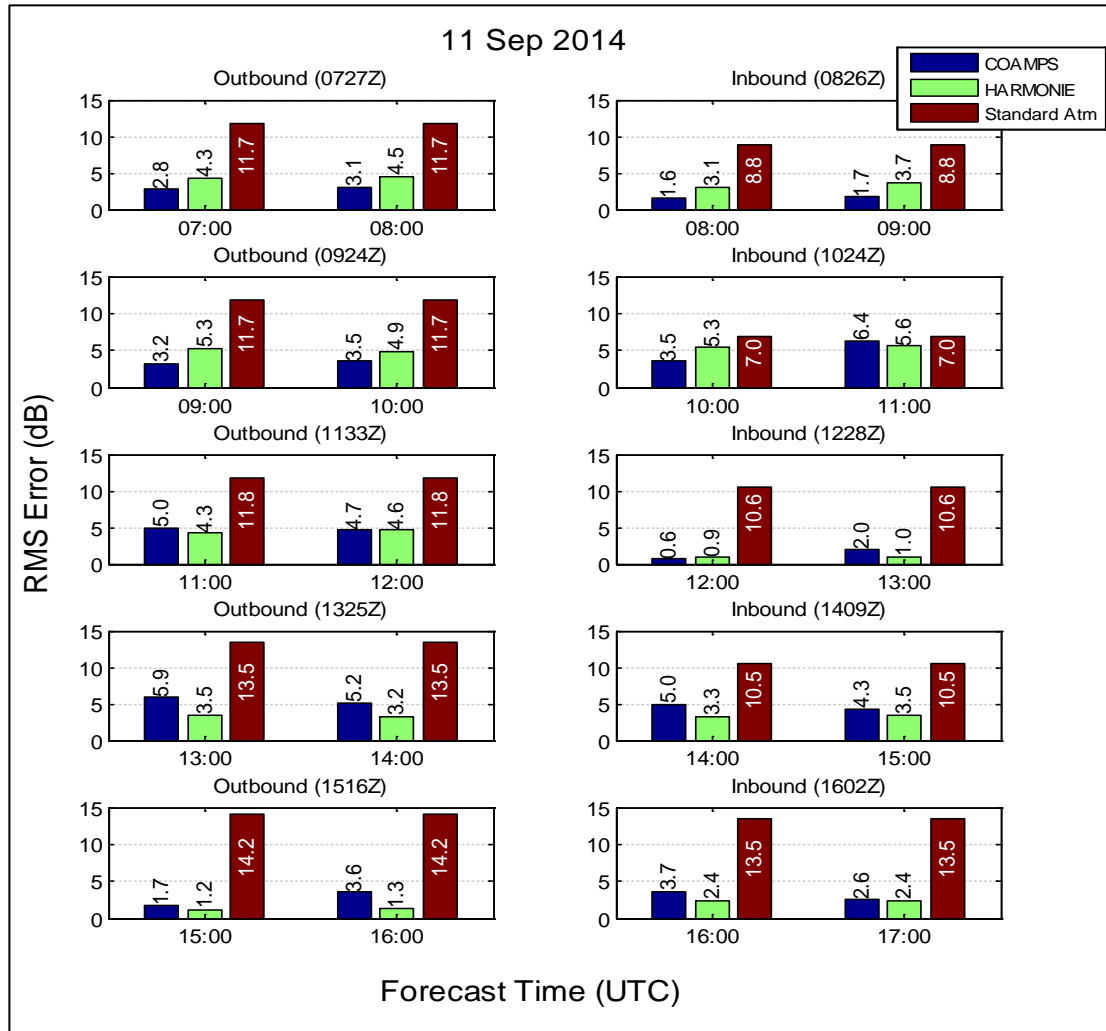

Figure 73. RMSE for all runs on 11 Sep 2014, of observed vs. predicted propagation factor based on COAMPS, HARMONIE, and standard atmosphere environments. Nearest temporal initialization and forecast times are used for the NWP environments.

Finally, Figure 74 provides the RMSE results for runs on 12 Sep 2014. Here again, propagation predictions based on both NWP models resulted in low RMSE values when compared with observations, much lower than that based on standard atmosphere.

In focusing on the nearest temporal initialization times for results presented in Figures 71 to 74, the assumption is that propagation predictions based on the nearest times, or lowest latency, would produce the best results; i.e., lowest RMSE values. However, we found this not to be the case and found that both NWP models provided inconsistent results. This is illustrated in Figures 75 to 78.
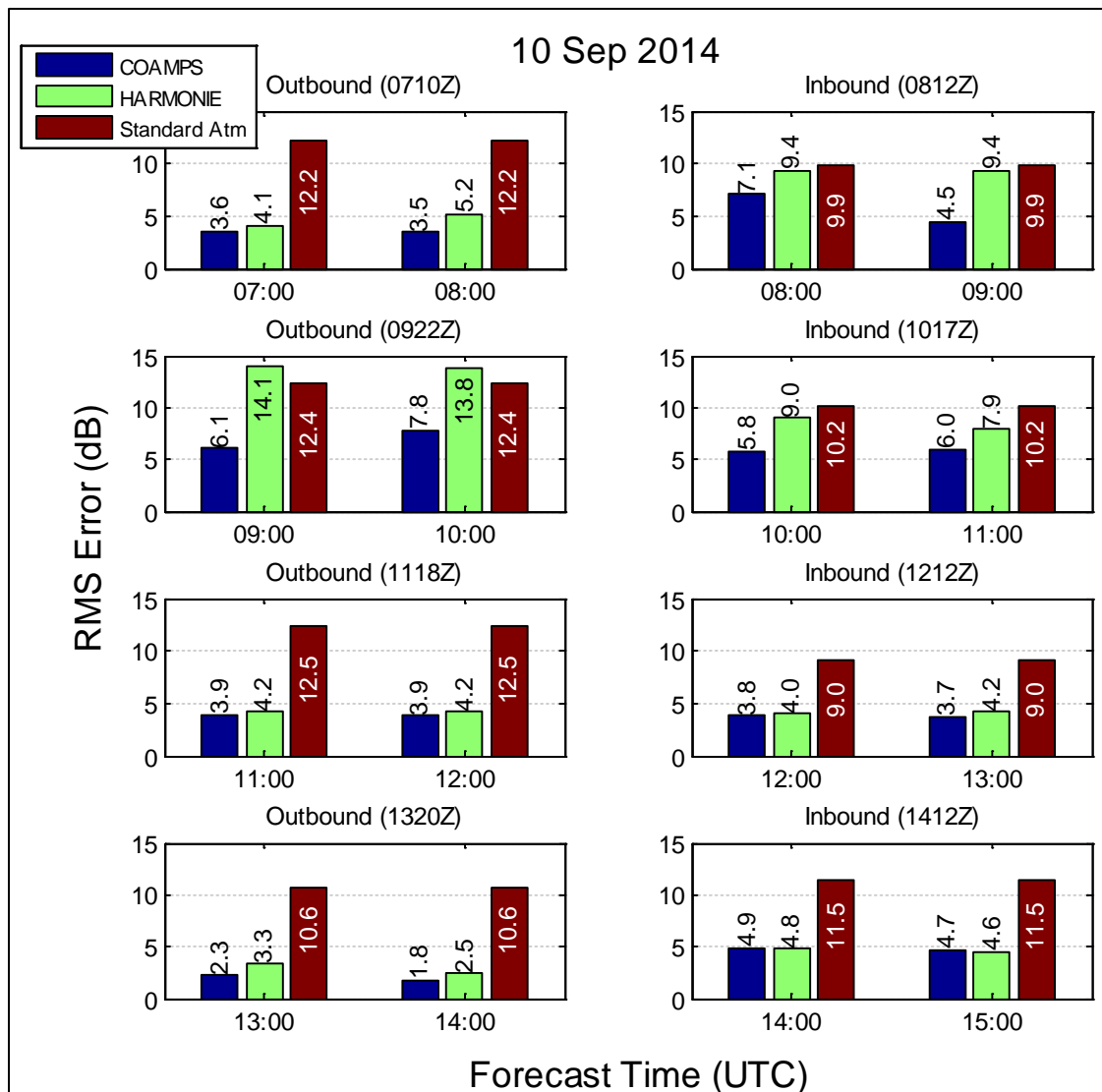
69
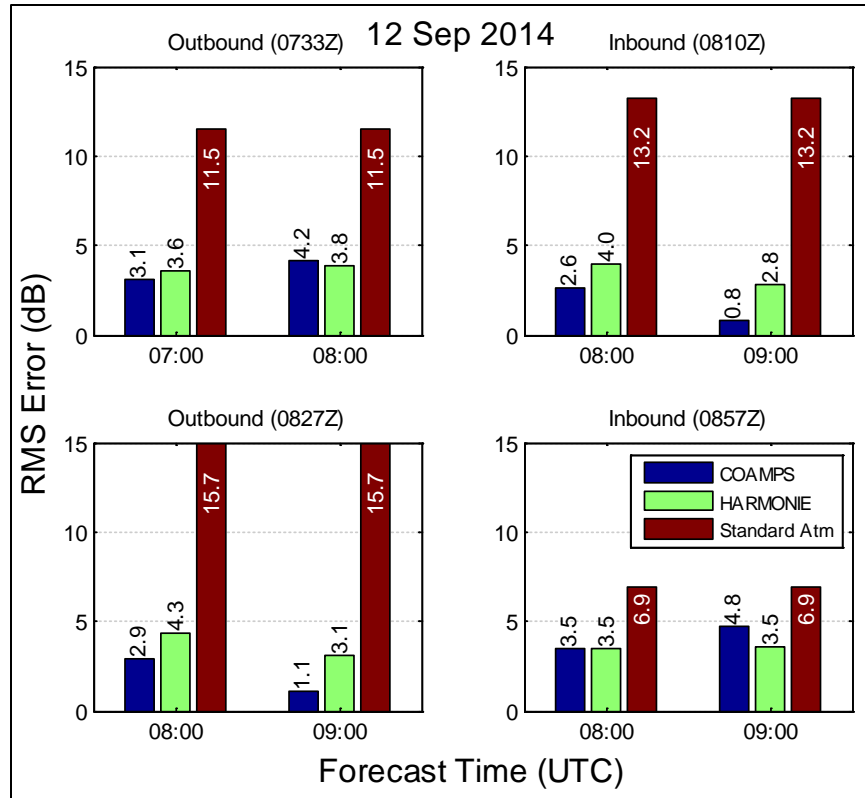
Figure 74. RMSE for all runs on 12 Sep 2014, of observed vs. predicted propagation factor based on COAMPS, HARMONIE, and standard atmosphere environments. Nearest temporal initialization and forecast times are used for the NWP environments.
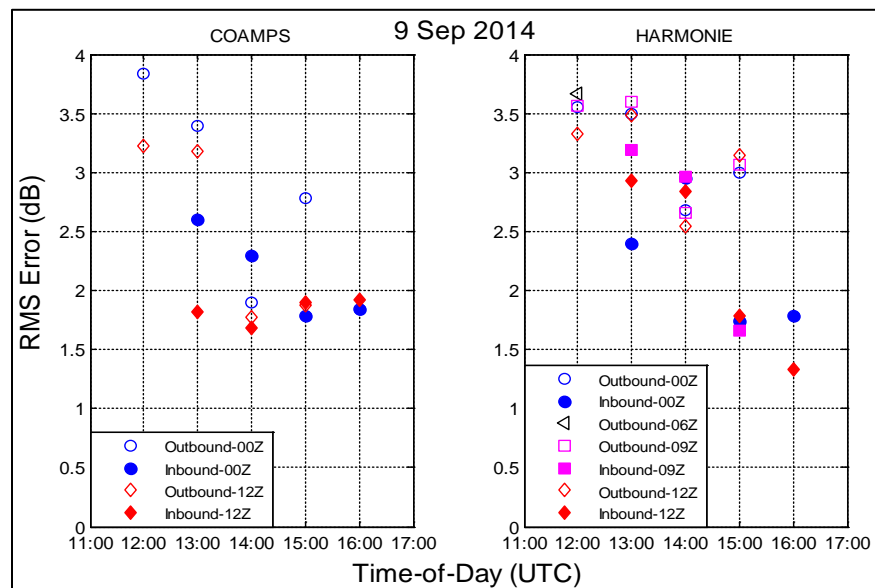
Figure 75. RMSE of observed vs. predicted propagation factor from COAMPS- and HARMONIE-based refractivity for all initialization times for 9 Sep 2014.

70
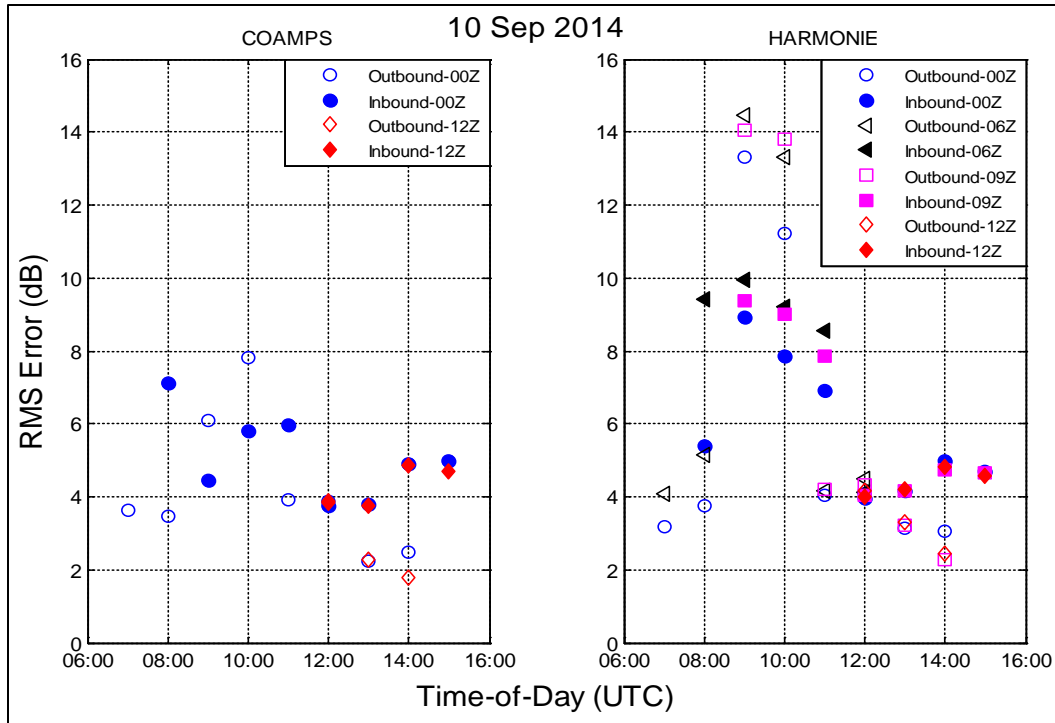
Figure 76. RMSE of observed vs. predicted propagation factor from COAMPS- and HARMONIE-based refractivity for all initialization times for 10 Sep 2014.
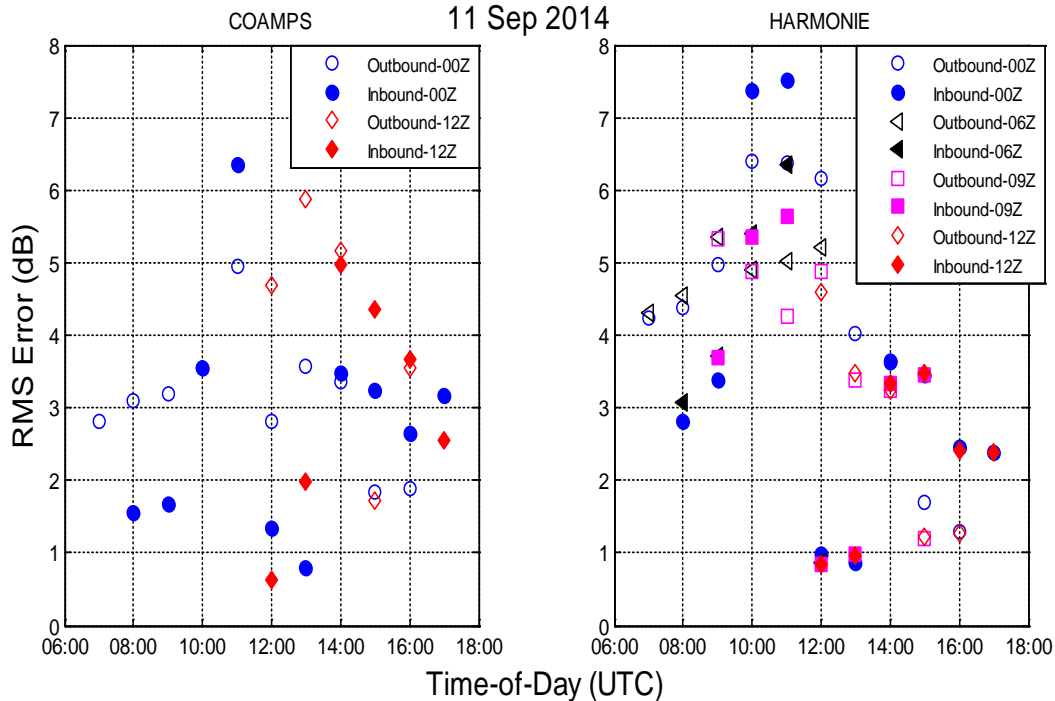
Figure 77. RMSE of observed vs. predicted propagation factor from COAMPS- and HARMONIE-based refractivity for all initialization times for 11 Sep 2014.
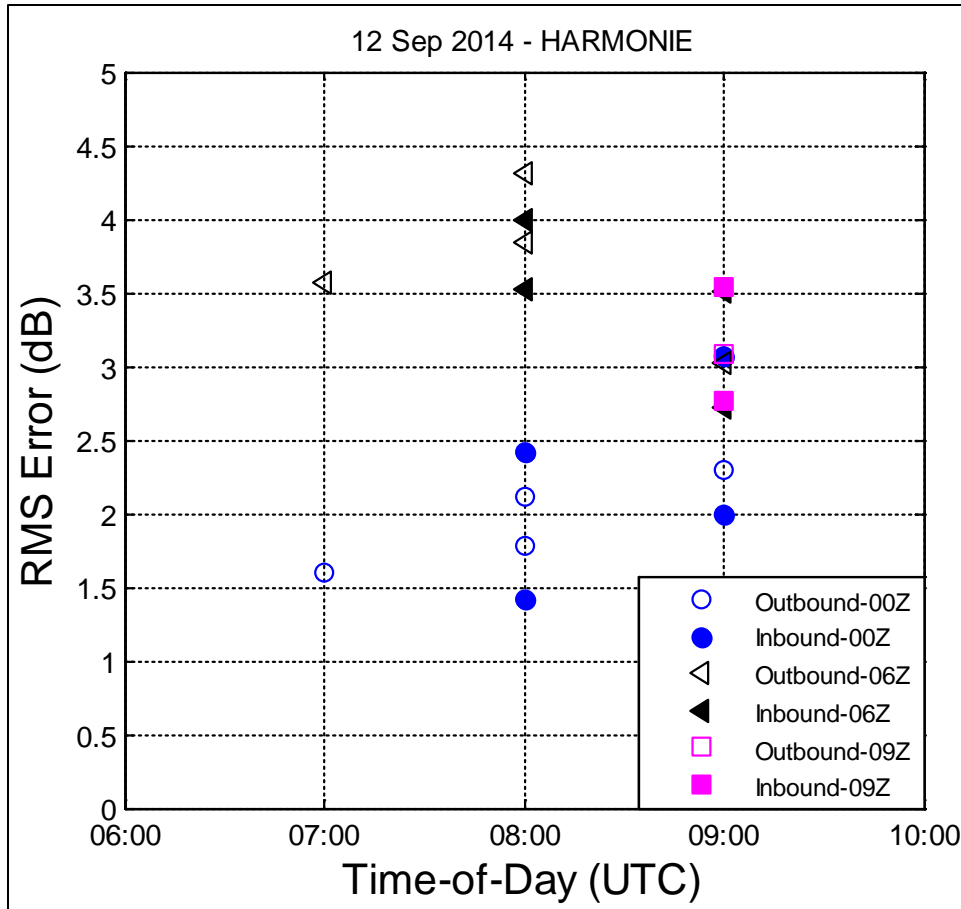
Figure 78. RMSE of observed and predicted propagation factor from HARMONIE-based refractivity for all initialization times for 12 Sep 2014.

These figures show the RMSE values for the nearest forecast times (horizontal axis) for all outbound and inbound FRISC runs, but using all initialization times. The RMSE values for all outbound runs are indicated by open markers, and all inbound runs are indicated by solid markers. Each set of RMSE values brackets an outbound or inbound FRISC start time, and the visual comparison should be made between like markers (i.e., compare all open markers, associated with different initialization times for outbound runs, separately from all solid markers).

For instance, in Figure 75, all runs for 9 Sep 2014 have an afternoon start time, so one would expect that predictions based on COAMPS forecasts with initialization times of 12Z would provide better agreement than those with initialization times at 00Z. For this day, this is the case for most of the predictions, as the 12Z outbound values (red open diamonds) indicate lower RMSE than the 00Z outbound values (blue open circles). Similarly, for the inbound runs the RMSE for 12Z (red solid diamonds) provided lower RMSE than those for 00Z (blue solid circles). The last two predictions at 15:00 and 16:00 are very similar, with no significant distinction between the two. For predictions based on HARMONIE forecasts (right graphic), the trend is not so clear. Here, the RMSE values for the outbound (open markers) 12Z initialization times appear to be slightly lower than the 00Z, 06Z, and 09Z initializations for two of the four forecast times (12:00 and 14:00), but are very similar for the remaining. The RMSE values for the inbound runs (solid markers) show no distinctive trend as

the 12Z initialization forecasts produced a lower RMSE only for the 16:00 forecast. However, based on the overall scale of difference between all RMSE values, this is arguably insignificant.

In Figure 76, for 10 Sep 2014 there was no distinction in RMSE between the COAMPS 00Z and 12Z initialization forecasts for all afternoon inbound runs. The HARMONIE 00Z-based predictions resulted in lower RMSE values than the [lower latency] initialization times of 06Z and 09Z for both morning inbound and outbound runs, whereas all RMSE values for the afternoon runs are indistinguishable.

For 11 Sep 2014, Figure 77 results from COAMPS are somewhat counter-intuitive in that the 00Z initialization forecasts resulted in lower RMSE values than those at 1200Z for the majority of the afternoon inbound and outbound runs. In this case, the HARMONIE-based results provided the more consistent correlation of lower RMSE associated with low latency initialization forecasts for the majority of the morning FRISC runs, with the exception of the first three forecasts, although the differences are small (within 0.5 dB). For all afternoon runs, the RMSE values are similar, regardless of initialization time.

Lastly, for 12 Sep 2014 (Figure 78), only HARMONIE-based results are shown as only two morning runs were conducted and COAMPS results consisted of one initialization time at 00Z. Here again, we see that results are not consistent in that lower RMSE values are associated with the higher latency initialization time of 00Z for both inbound and outbound runs.

Another metric in gauging the "goodness of fit" of predicted propagation factor is to view the cumulative distribution function (CDF) of the predictions against the observed data. This is illustrated in Figures 79 to 82 for each day, where distribution functions from both COAMPS- and HARMONIE-based results are shown alongside the observed data. Here, the non-filtered (raw) observed data is used and only those predictions that are time [or range]-coincident with observations are included in the CDF plots. In keeping consistent with Figures 71 to Figure 74, only those forecast times immediately prior and following each FRISC run, coinciding with the nearest initialization time from each NWP model, are shown in the figures. With the exception of "clear misses" from both NWP models for the 0922Z outbound run and 0812Z & 1017Z inbound runs on 10 Sep 2014, the NWP-based propagation predictions provide very good agreement with observations, particularly when viewed against the conventional standard atmosphere assumption. For CDF plots for all initialization times for both NWP models are shown in Figures A-35 to A-42 in Appendix A.

Figure 79. Cumulative distribution functions of observed and predicted propagation factor based on nearest forecast and initialization times from COAMPS and HARMONIE for 9 Sep 2014: (a) outbound, and (b) inbound runs.

Figure 80. Cumulative distribution functions of observed and predicted propagation factor based on nearest forecast and initialization times from COAMPS and HARMONIE for 10 Sep 2014: (a) outbound, and (b) inbound runs.

Figure 81. Cumulative distribution functions of observed and predicted propagation factor based on nearest forecast and initialization times from COAMPS and HARMONIE for 11 Sep 2014: (a) outbound, and (b) inbound runs.
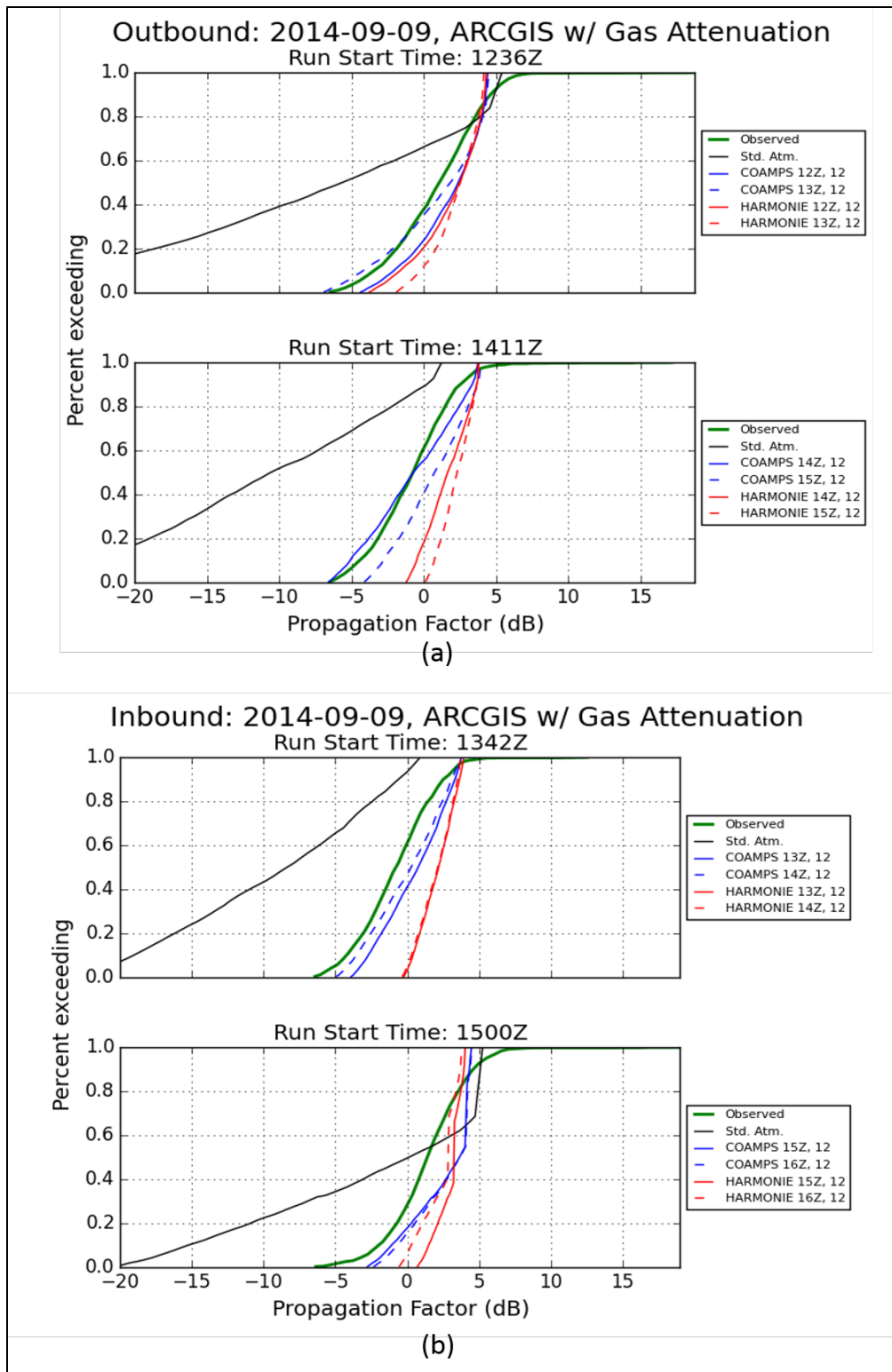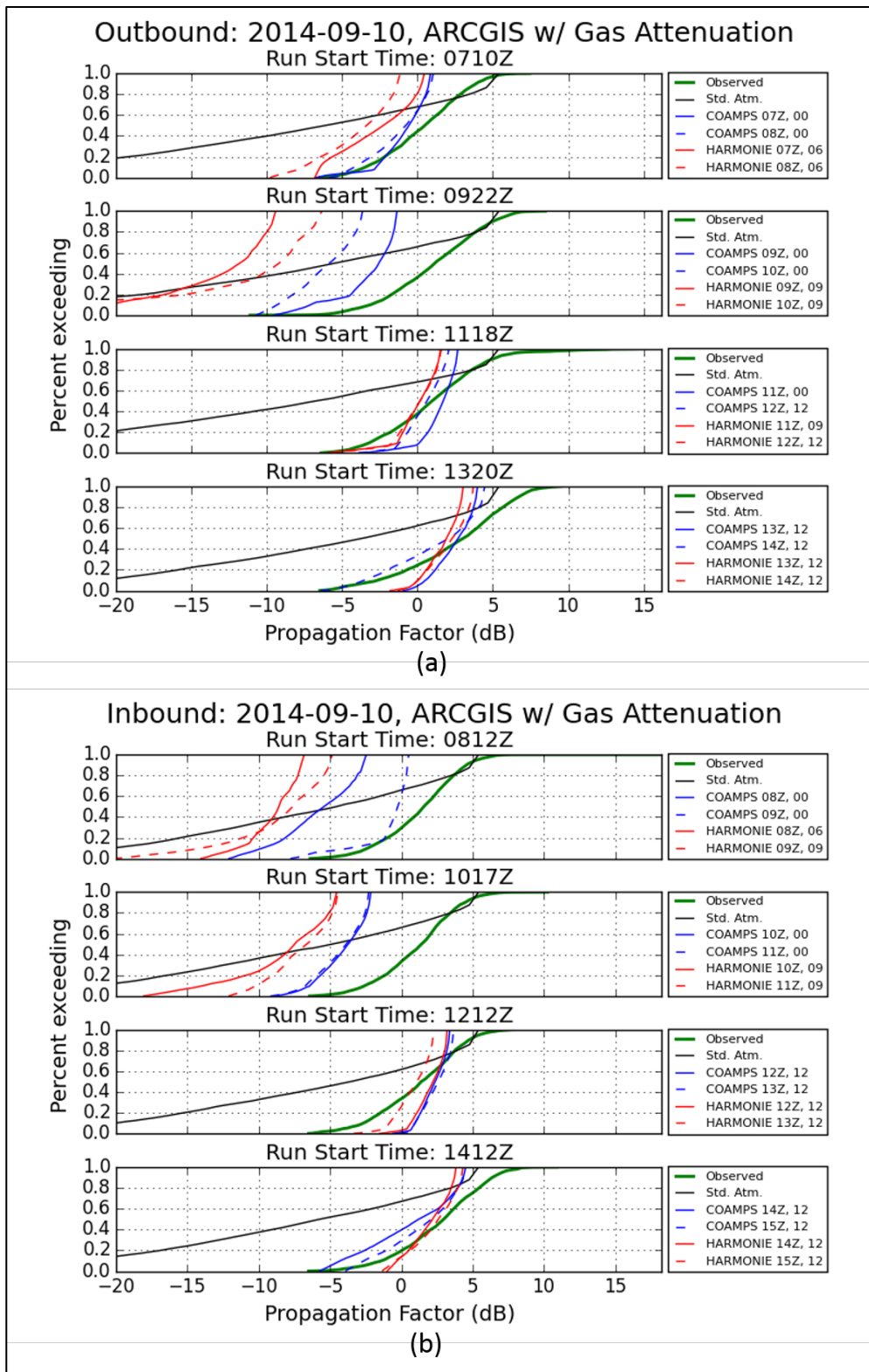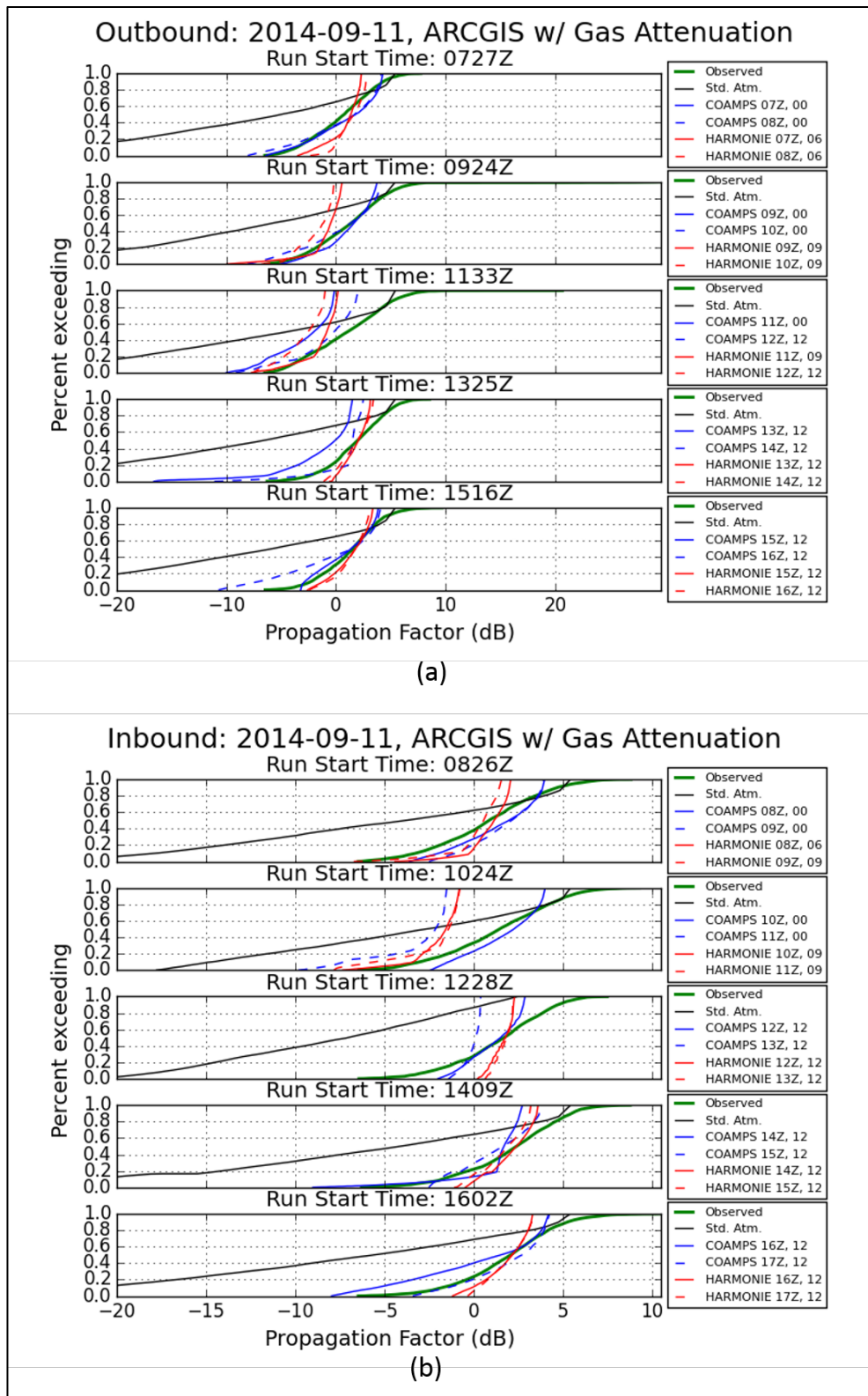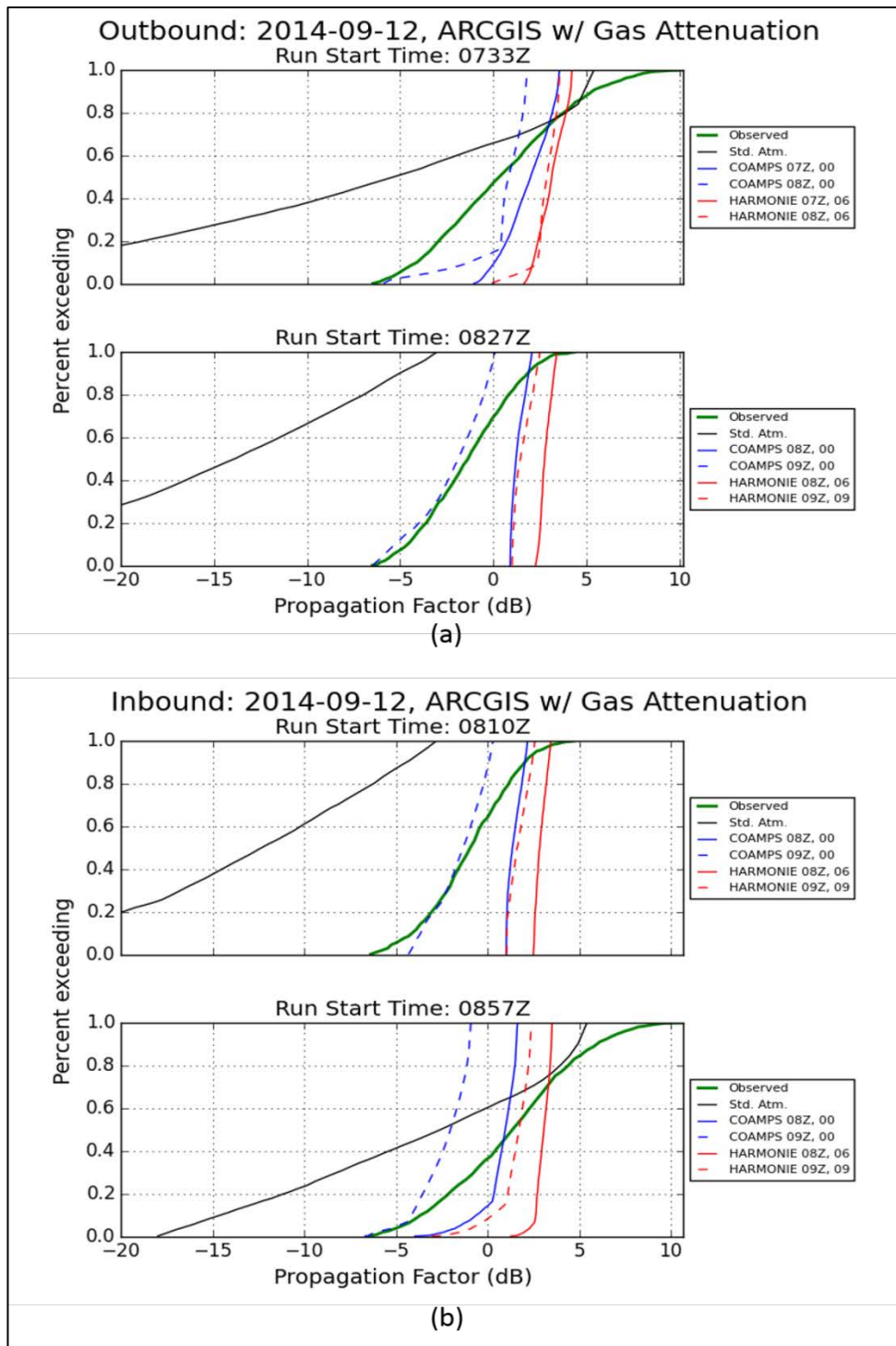
Figure 82. Cumulative distribution functions of observed and predicted propagation factor based on nearest forecast and initialization times from COAMPS and HARMONIE for 11 Sep 2014: (a) outbound, and (b) inbound runs.

77

One noticeable discrepancy, when viewing Figures 52 to 59, is that F predictions from both NWP models predict a deep null between 5 km and 10 km, whereas a similar null is noticeably absent from the observed data for those runs where the RCS (or propagation factor) was measured at ranges less than 10 km. One explanation to account for this discrepancy is the possibility that as the FRISC traversed nearer to the radar antenna, the FRISC-plus-corner-reflector no longer appeared as a point target but behaved as a distributed target to the APAR. The observed F would then behave as if "smeared" over several target heights within a small distribution about the actual. As a small test, the COAMPS environment for the 1325Z run on 11 Sep 2014 was used, in combination with the APM, to compute F as a function of range for five receiver heights centered at the original target height ± 2.0 m at 1.0 m increments. For ranges less than 10 km, the average F was computed from these five target heights and this was combined with the original predicted F for ranges greater than 10 km. The result is shown in Figure 83. While the depth of the null has indeed been reduced, the peak prior to this has also been reduced, which may prevent an overall lower RMSE.
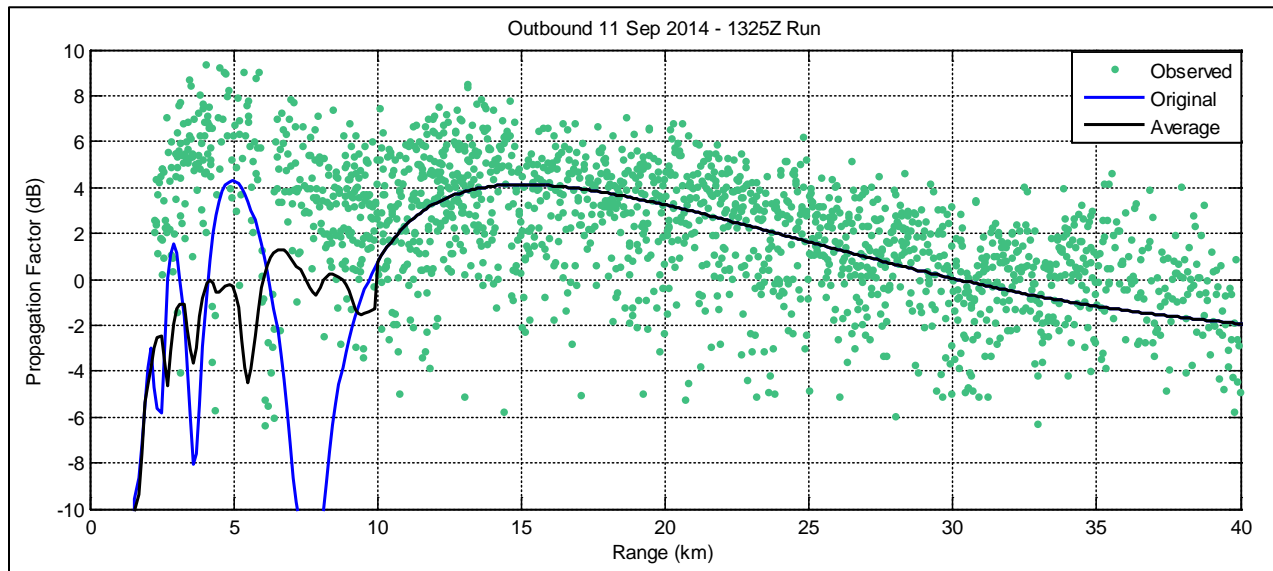

Figure 83. Case shown is Figure 56(a) for the COAMPS environment (1400Z forecast, 0000Z initialization) and 1325Z run. Blue curve is the original single target height prediction. Black curve is averaged F over five target heights at ranges less than 10 km.

6.2 RF PERFORMANCE BASED ON in-situ MET OBSERVATIONS

Figures 84 to 87 show the RMSE between the observed and predicted F based on the in-situ range-dependent environments described in Section 5.4.2. The RMSE based on standard atmosphere are identical to those shown in Figures 71 to 74 and is duplicated here for ease of comparison. Overall, the in-situ-based predictions show favorable agreement with observations where the RMSE is 5 dB or less for the majority of the runs during the IOP. The exceptions are the four runs on 10 Sep 2014 (0812Z, 0922Z, 1017Z, and 1118Z). On this day, the 1017Z run in particular produced an RMSE greater than that assuming standard atmosphere conditions. We see that this is consistent with the NWP-based results when comparing Figure 85 with Figure 72, although in Figure 72, the largest RMSE occurred for the 0922Z run. For both sets (NWP-based and in-situ-based) of propagation factor predictions the morning runs from 0812Z to 1118Z were the most problematic.

Figure 84. RMSE for all outbound and inbound runs on 9 Sep 2014, of observed vs. predicted propagation factor based on TACMET and shore radiosonde observations.

Figure 85. RMSE for all outbound and inbound runs on 10 Sep 2014, of observed vs. predicted propagation factor based on TACMET and shore radiosonde observations.
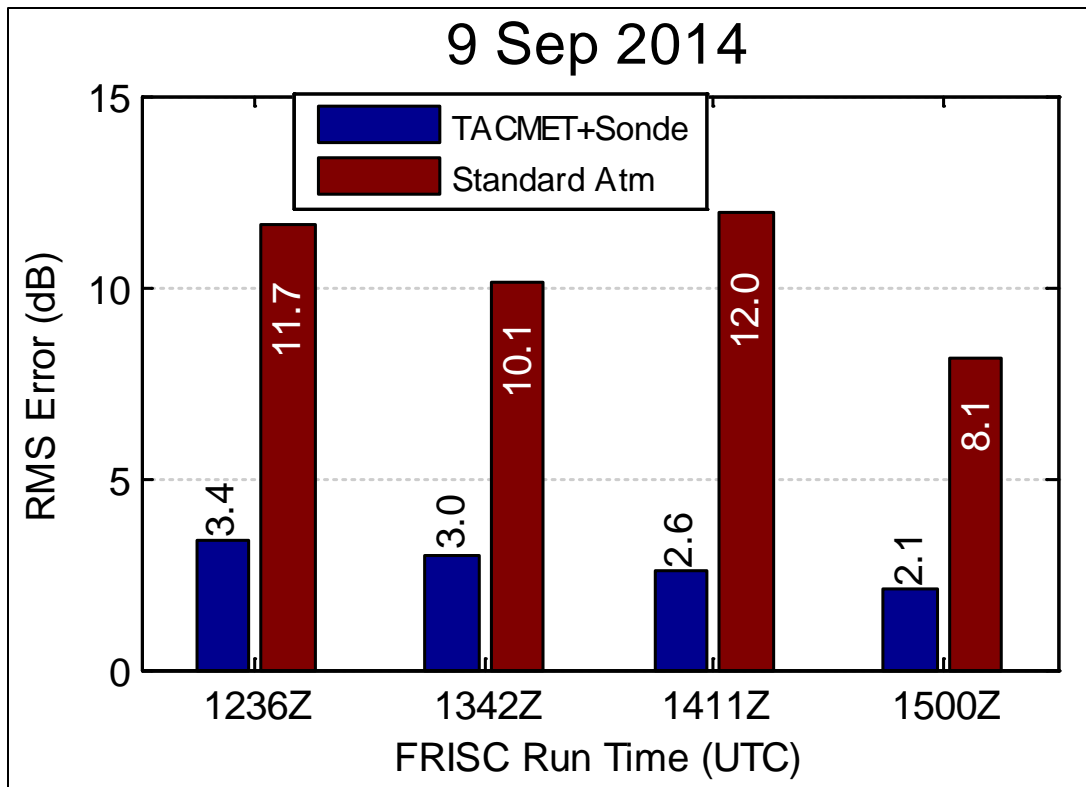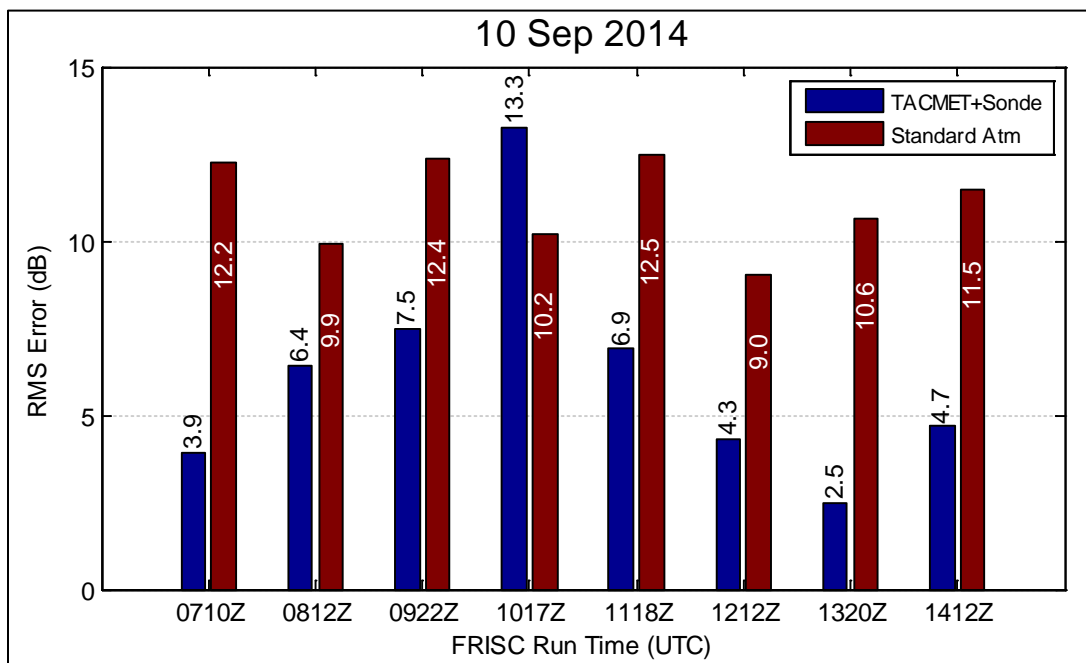
Figure 86. RMSE for all outbound and inbound runs on 11 Sep 2014, of observed vs. predicted propagation factor based on TACMET and shore radiosonde observations.
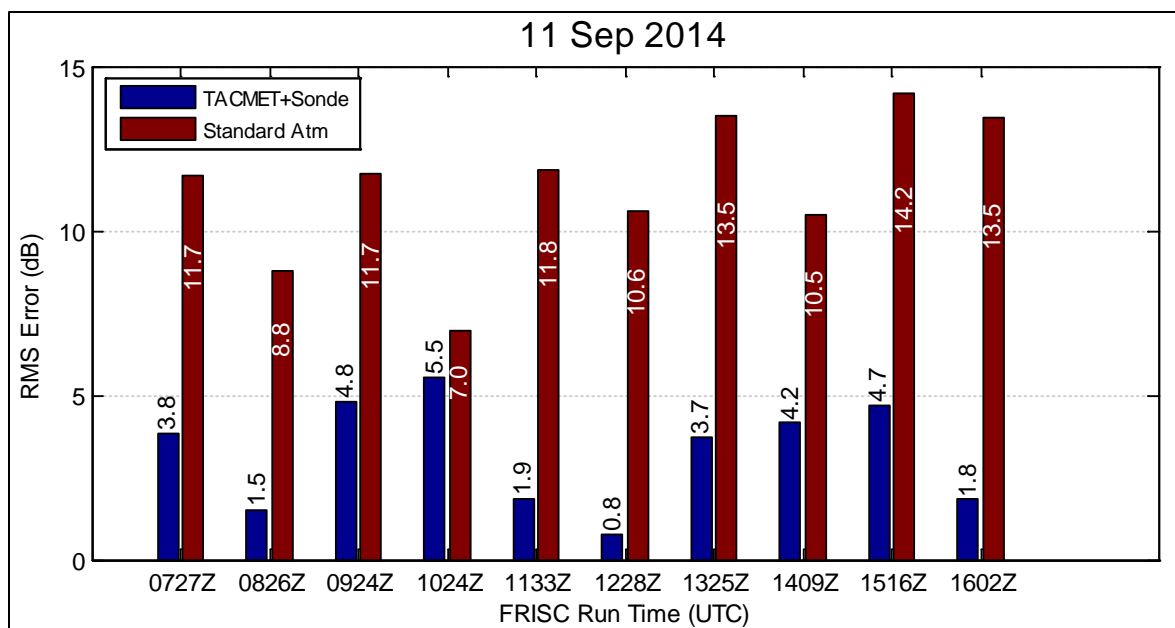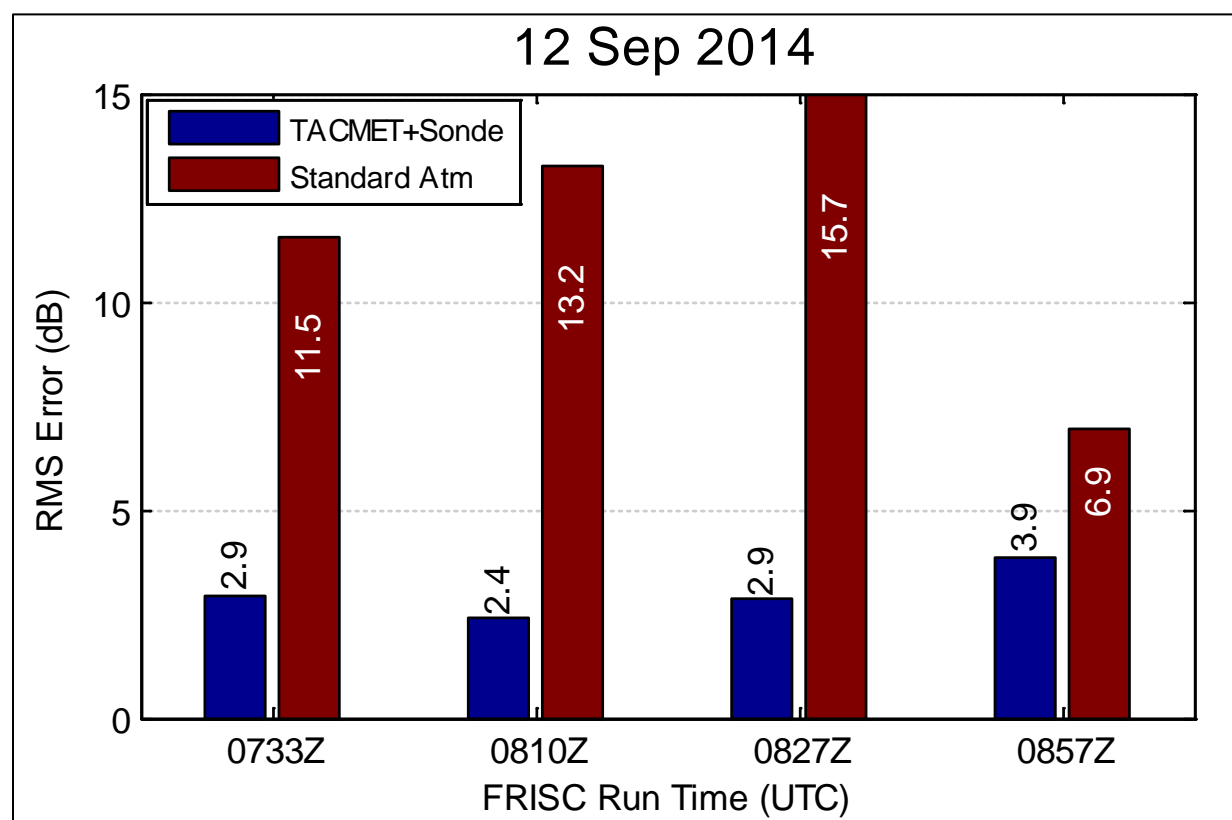

Figure 87. RMSE for all outbound and inbound runs on 11 Sep 2014, of observed vs. predicted propagation factor based on TACMET and shore radiosonde observations.

Considering the in-situ-based RMSE results are arguably inconclusive due to the use of climatology for the source of the near-shore SST, very good agreement for the majority of the FRISC run events prevent an outright dismissal of the results.

For ease of direct comparison, the RMSE results based on predictions from both NWP models and the in-situ data are shown in Figures 88 to 91. The RMSE results based on both NWP models are taken from the nearest temporal forecast to the FRISC run time. With the exception of the 10 Sep 2014 morning runs, all show comparable agreement. While isolated FRISC runs can be identified where each of the NWP models, as well as the in-situ observations, resulted in the "worst" or "best" fit, there is no consistent overall "winner" as generally, all provide excellent agreement with the observed propagation factor.

Figure 88. RMSE for all inbound and outbound runs for 9 Sep 2014 based on in-situ observations and NWP forecasts.

Figure 89. RMSE for all inbound and outbound runs for 10 Sep 2014 based on in-situ observations and NWP forecasts.
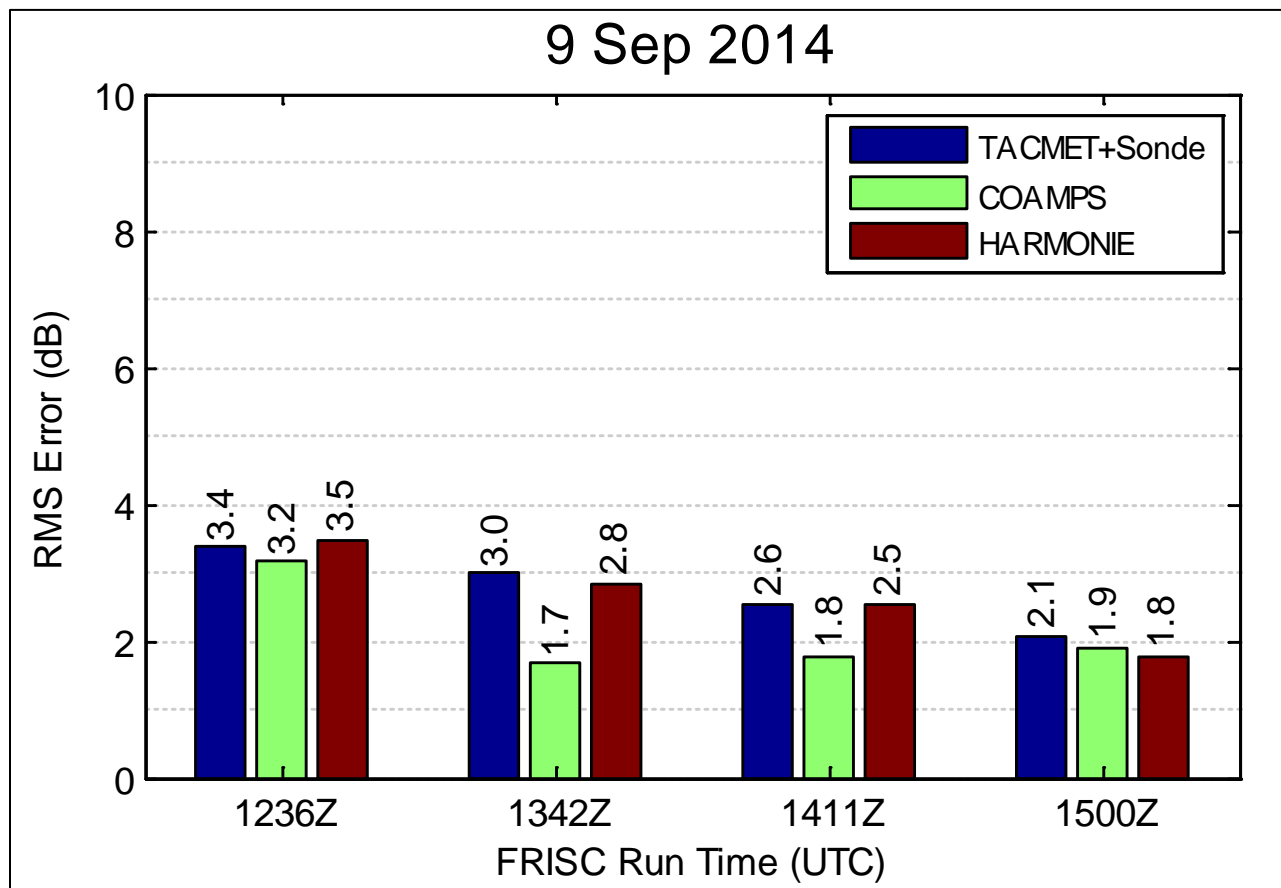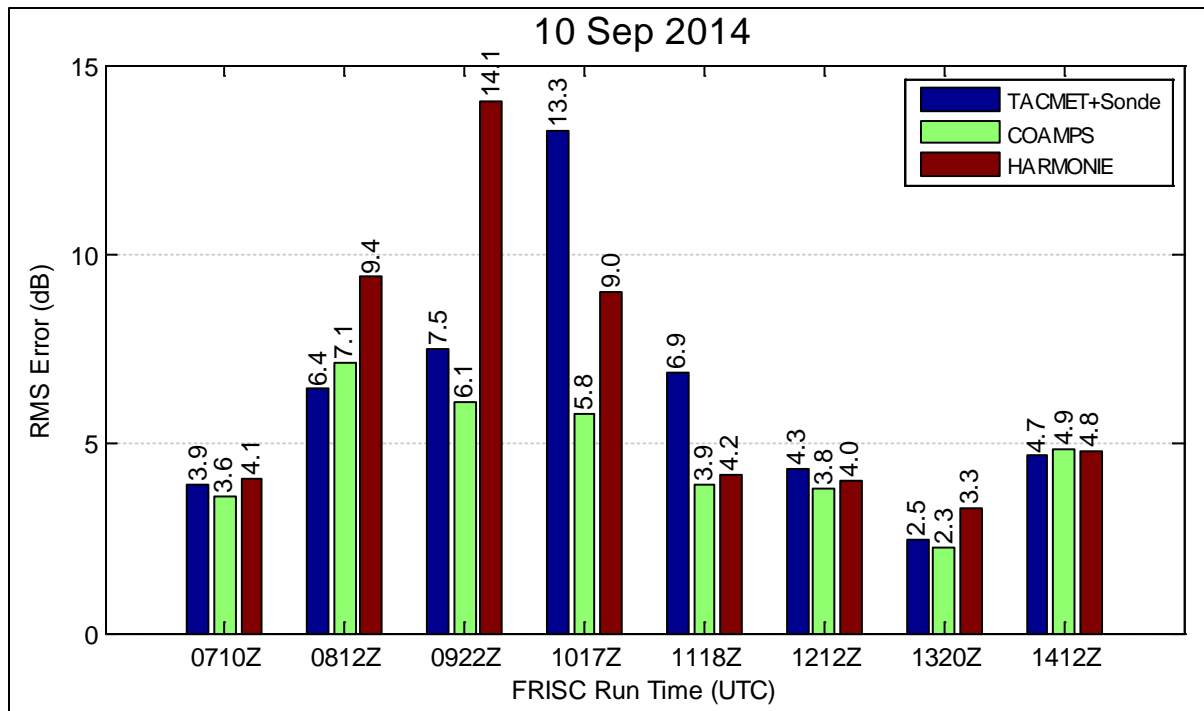

Figure 90. RMSE for all inbound and outbound runs for 11 Sep 2014 based on in-situ observations and NWP forecasts.
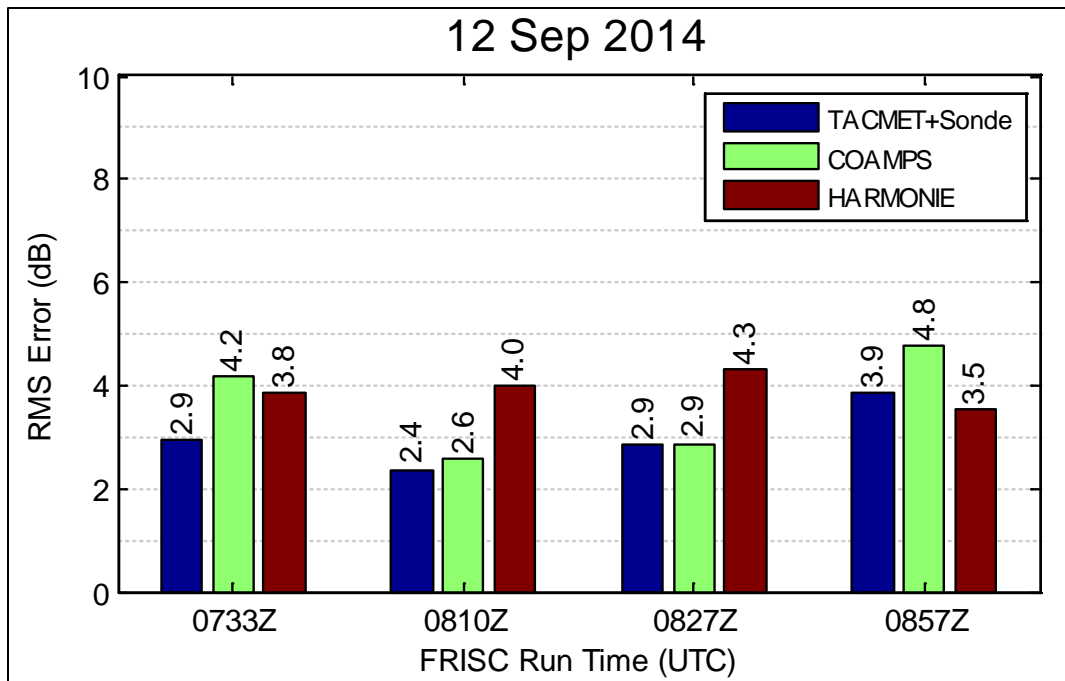
Figure 91. RMSE for all inbound and outbound runs for 12 Sep 2014 based on in-situ observations and NWP forecasts.

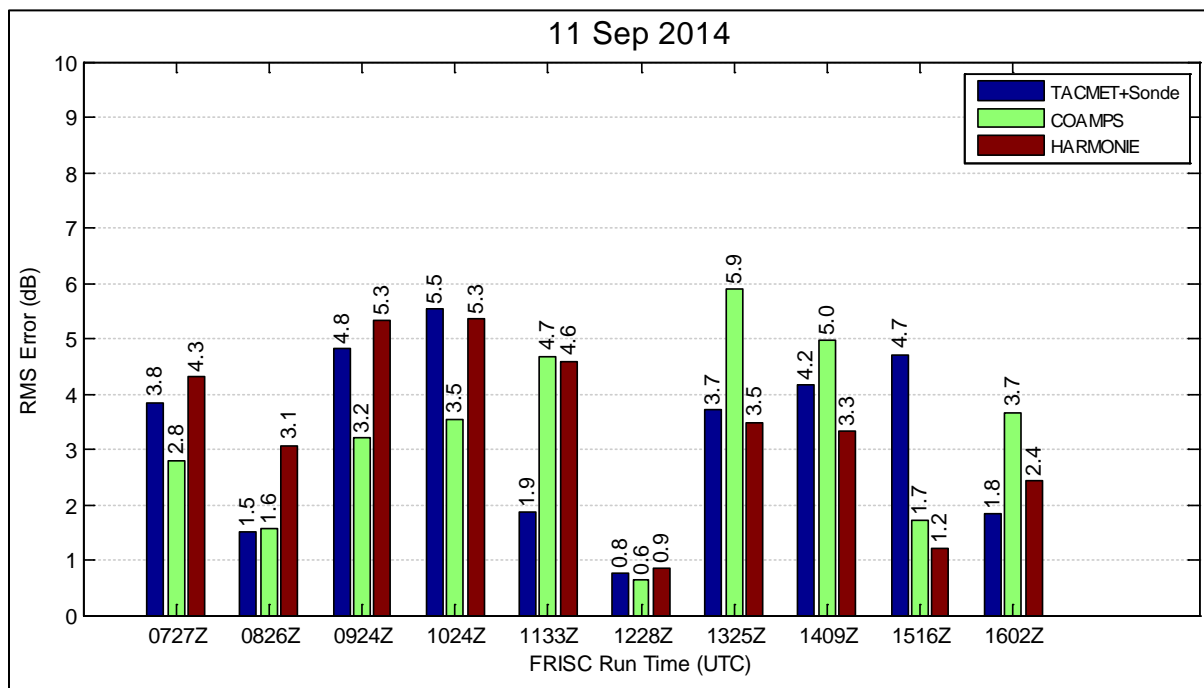Similar to Section 6.1, the corresponding cumulative distribution functions for all inbound and outbound runs during the IOP are shown in Figures 92 to 95. Again, there is overall good agreement, exception for the previously mentioned 10 Sep 2014 morning runs.

Figure 92. Cumulative distribution functions of observed and predicted propagation factor based on TACMET and radiosonde observations for 9 Sep 2014: (a) outbound, and (b) inbound runs.

Figure 93. Cumulative distribution functions of observed and predicted propagation factor based on TACMET and radiosonde observations for 10 Sep 2014: (a) outbound, and (b) inbound runs.
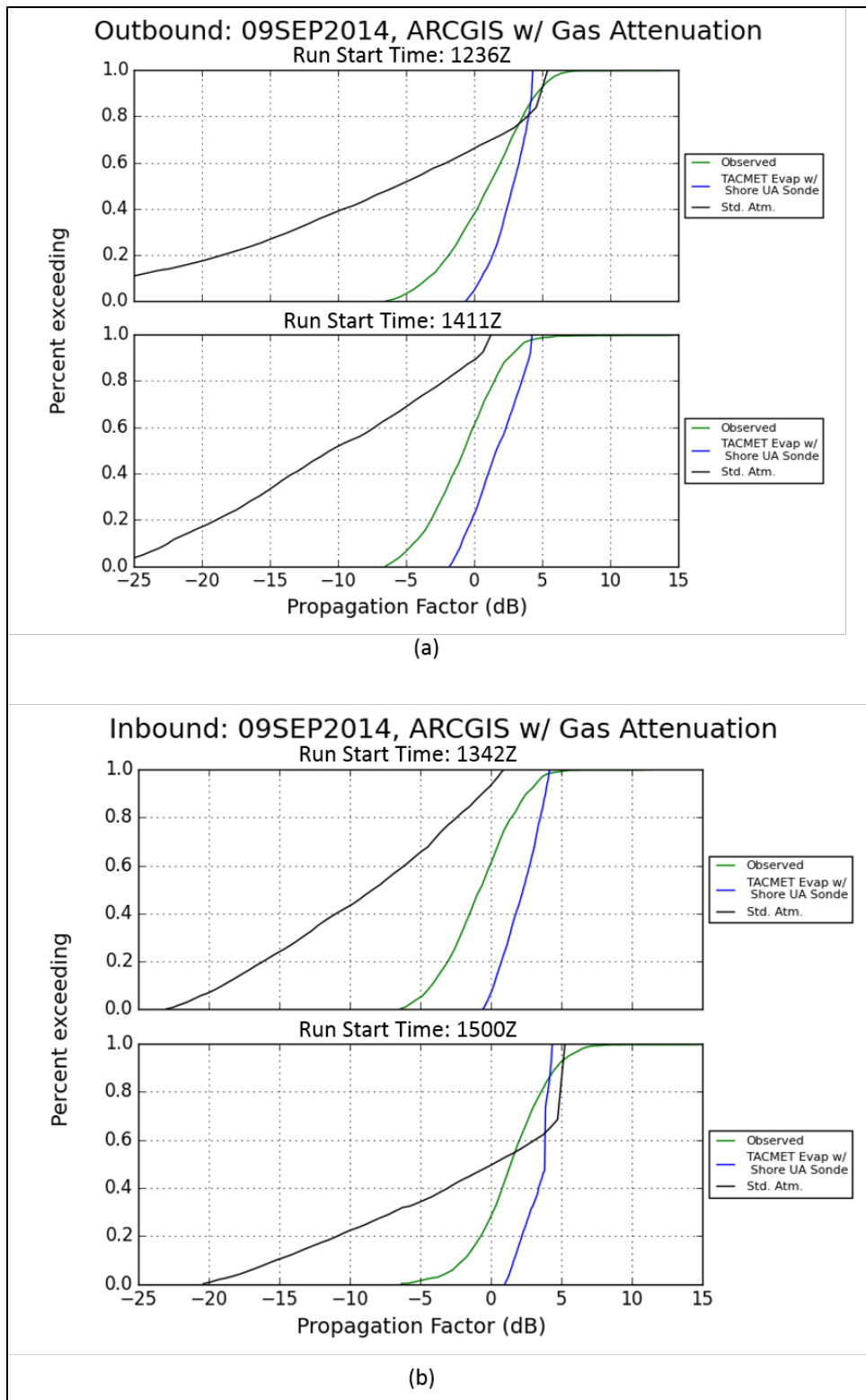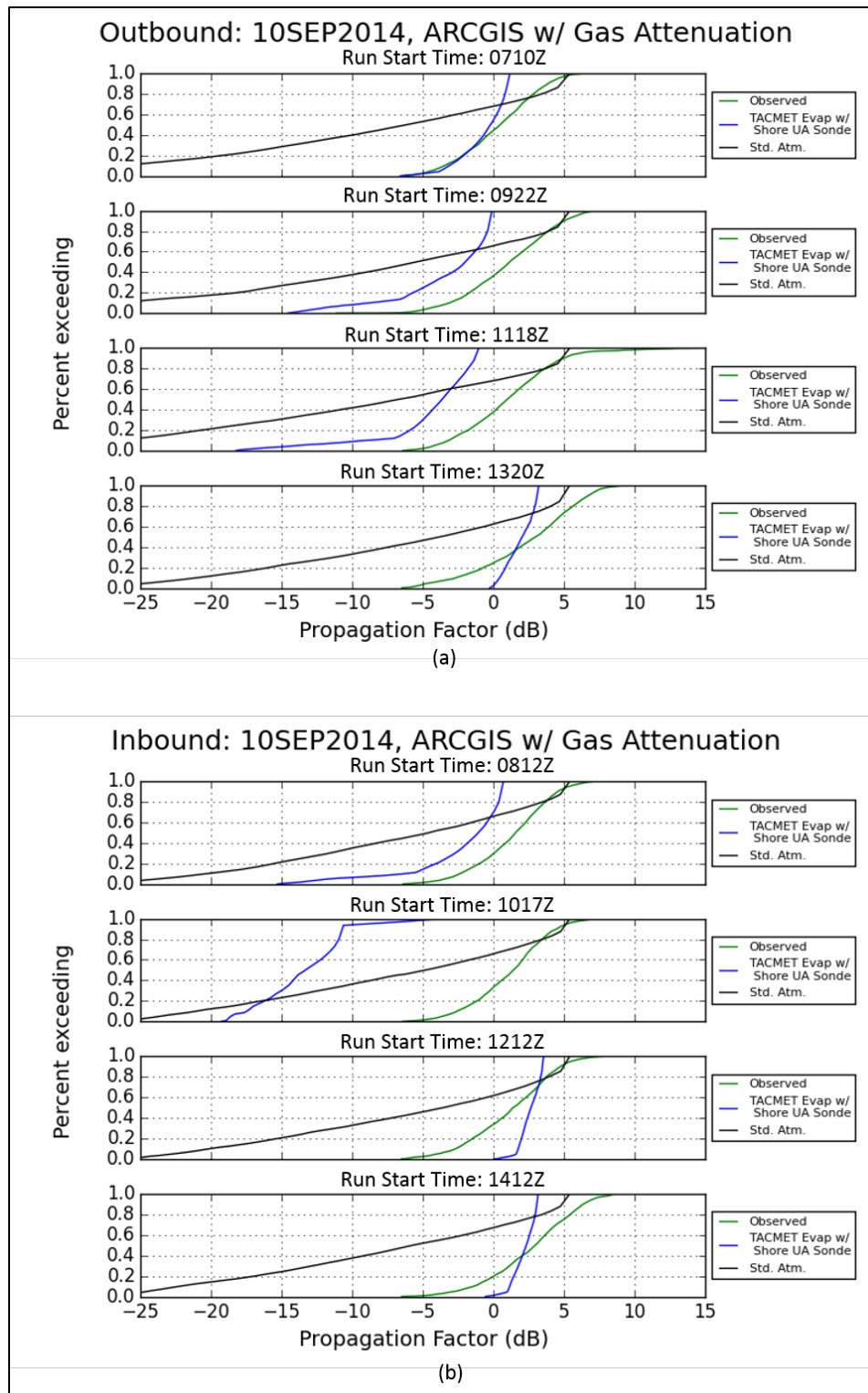
Figure 94. Cumulative distribution functions of observed and predicted propagation factor based on TACMET and radiosonde observations for 11 Sep 2014: (a) outbound, and (b) inbound runs.
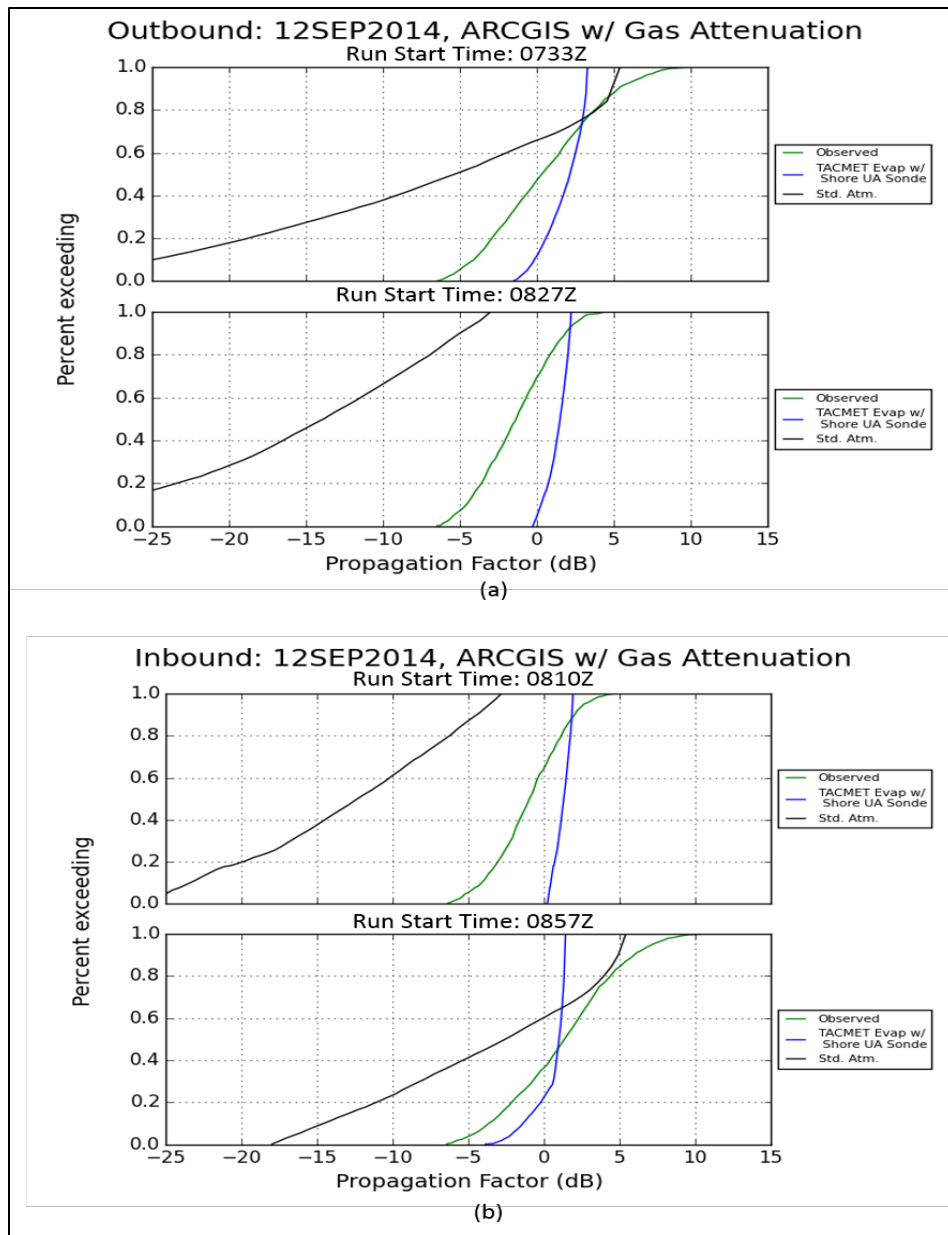
Figure 95. Cumulative distribution functions of observed and predicted propagation factor based on TACMET and radiosonde observations for 12 Sep 2014; (a) outbound, and (b) inbound runs.
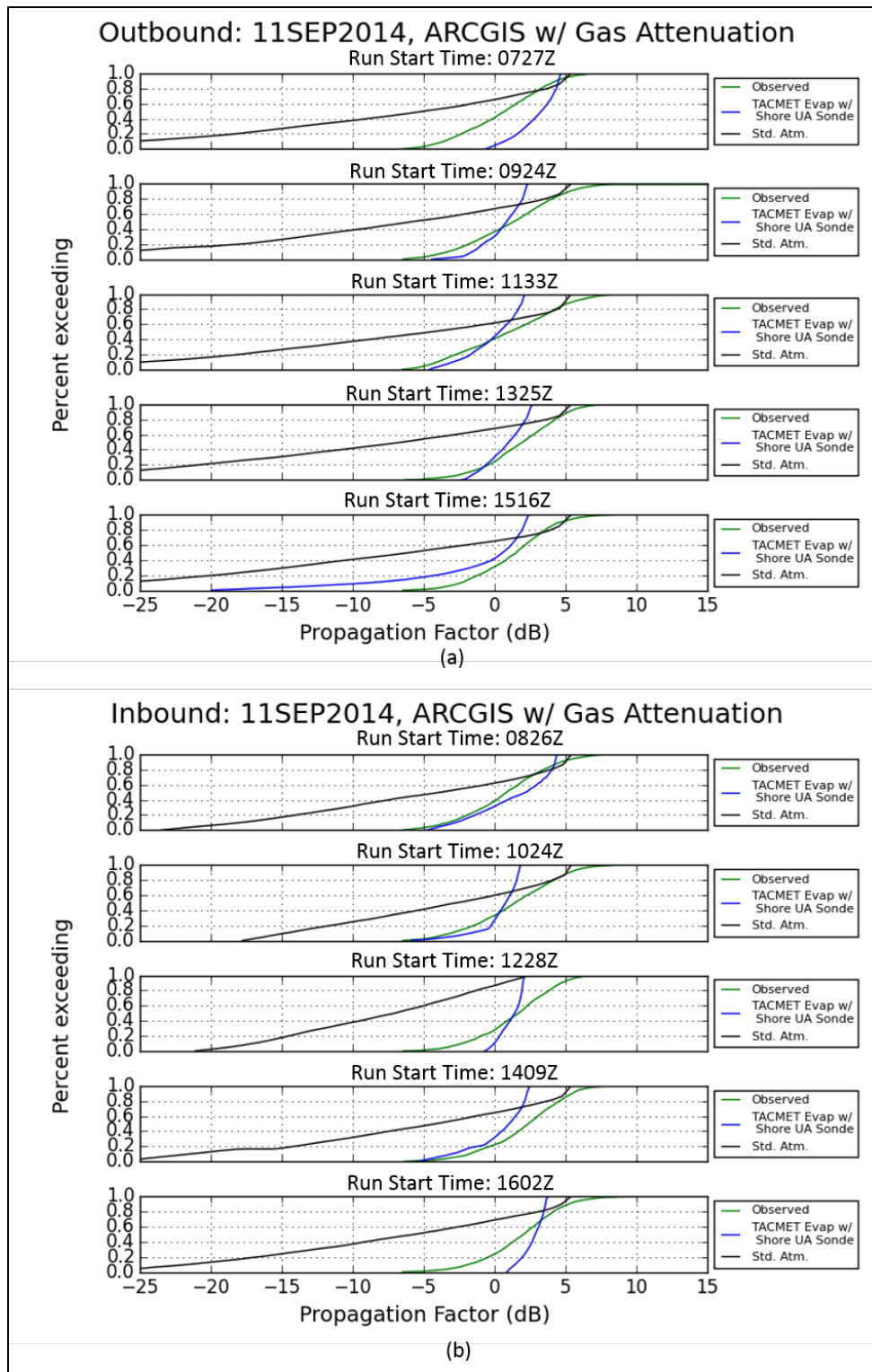
6.3 DATA ASSIMILATION - FUTURE WORK

As a final step in the analysis of the Phase 1 data, assimilation of the observed in-situ meteorological observations with the NWP forecasts will be conducted. The expectation is that the resulting refractive environment will be a better representation of the actual environment during the time of the RF measurements. Improved statistical performance of predicted vs. observed propagation factor would be evidence of this. Results of this work will be documented in a future report.

7. SUMMARY

The maximum ranges at which the FRISC target were detected and tracked for all four days of the IOP are shown in Figure 96. For these geometries, the "normal" range, indicated by the dotted red line, represents the maximum range under standard atmosphere conditions.

Detection ranges on FRISC with corner reflector
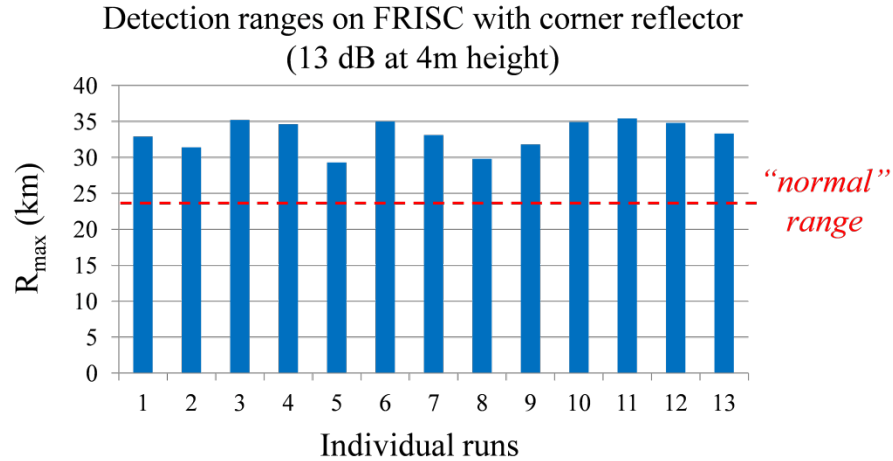(13 dB at 4m height)

Figure 96. Summary of maximum logged ranges for all FRISC runs during the IOP.

From Figure 96 and Sections 5 and 6, a summary of highlights are as follows:

1. The evaporation duct was clearly the major influence of propagation effects observed during the IOP, with upper air radiosonde measurements indicating relatively benign conditions, which resulted in greater-than-normal detection ranges for surface-to-surface geometries
2. The assumption of standard atmosphere conditions consistently resulted in the largest error when compared with observations
3. Both COAMPS and HARMONIE surface layer forecasts resulted in significantly different variability in evaporation duct parameters over the region of interest; however, when compared to observed propagation factor, predicted propagation factor from both NWP-based environments showed excellent agreement overall, with a median RMSE of 4 dB or less
4. The use of lowest latency (nearest initialization time) in the NWP forecasts did not always result in the lowest RMSE
5. Propagation factor predictions based on [sparse] in-situ measurements also showed very good agreement with observations overall
6. A small variation in target height can lead to a significant variation in propagation factor, potentially leading to large variations in detection ranges, which may suggest the optimum RF performance prediction methodology is to determine detection ranges by averaging over a small "array" of target heights, along with also providing an upper and lower bounds to the detection range based on the minimum and maximum propagation factor at each range bin; of course, this may only be necessary at low altitudes that are predominantly affected by surface ducting.

The Phase 1 analysis demonstrates that RF performance can be adequately predicted with NWP model forecasts. Since the U.S. Navy has halted its shipborne radiosonde capability in 2012, its ever-increasing reliance on NWP forecasts to characterize the highly varying environment within an AOI is placing higher importance on the fidelity of NWP forecasts, as well as indirect sensing of the environment via refractivity inversion technologies such as refractivity from clutter and refractivity from radio (Rogers, Hattan, and Stapleton, 2000; Rogers, 1996). Data assimilation of all three sources of refractive information to better characterize the environment for determining shipboard sensor performance is also becoming increasingly important rather than simply relying on one source alone (Ascensio et al., 2015).

An often overlooked, but important, aspect of the analysis presented here is the chain of modeling and simulation capabilities employed to quantify the RF prediction performance: characterization of the environment requires NWP models (step 1), in combination with a surface layer model such as NAVSLaM (step 2), to provide input to a propagation model (APM) (step 3) in determining the effects of a varying environment on RF emissions. Each of these components in themselves can be associated with some inherent error in their respective mathematical techniques in combination with physical assumptions and approximations made in their implementation. The overall excellent performance of the RF predictions presented in this report is a testament to the quality of the state-of-the-art modeling capabilities in these [technical] areas for naval operational applications.

REFERENCES

ArcGis. Map of the Netherlands is available online at http://ahn.maps.arcgis.com/apps/webappviewer/index.html?id=c3c98b8a4ff84ff4938fafe7cc106e88. Accessed 7 September 2016.

Ascensio, A., T. Rogers, N. Gordon, T. Haack, and K. Horgan. 2015. "Refractivity Data Fusion." Radio Science Meeting (Joint with AP-S Symposium). USNC-URSI. 19–24 July. Vancouver, British Columbia, Canada.

Barrios, A. 2003. "Considerations in the Development of the Advanced Propagation Model (APM) for U.S. Navy Applications." *Proceedings of the International Conference on Radar* (RADAR 2003), 3–5 Sep. 2003, Adelaide, Australia.

Brousseau, P., L. Berre, F. Bouttier, and G. Desroziers. 2011. "Background-error Covariances for a Convective-scale Data-assimilation System: AROME–France 3D-Var." *Quarterly Journal of the Royal Meteorological Society 137*:409–422. doi: 10.1002/qj.750.

Frederickson, P. A. 2010. "Software Design Description for the Navy Atmospheric Vertical Surface Layer Model (NAVSLaM) CSCI (Version 1.0)." Prepared for the Naval Oceanographic Office Systems Integration Division. Naval Oceanographic Office Systems Integration Division. Stennis Space Center, MS.

Frederickson, P. A., J. T. Murphree, K. L. Twigg, and A. E. Barrios. 2008. "A Modern Global Evaporation Duct Climatology." *Proceedings of the International Conference on Radar* (RADAR 2008). 2–5 September, Adelaide, Australia.

Gerstoft, P., L. T. Rogers, W. S. Hodgkiss, and L.J. Wagner, 2003. "Refractivity Estimation using Multiple Elevation Angles," *IEEE Journal of Oceanic Engineering 28(3)*:513–525.

Hodur, R. M. 1997. "The Naval Research Laboratory's Coupled Ocean/Atmosphere Mesoscale Prediction System (COAMPS)," *Monthly Weather Review, 125*:1414–1430.

Horgan, K., T. Haack, Q. Wang, V. Wiss, W. Thornton, I. Renta, and R. Marshall. 2014. "Comparisons of Radiosonde Measurements and Numerical Weather Prediction Results Blended with a Surface Layer Model for the Radio Frequency Application" National Radio Science Meeting, USNC-URSI. 8–11 January, Boulder, CO.

International Telecommunication Union-Radiocommunication Recommendation. 2012. "Attenuation by Atmospheric Gases." ITU-R Rec. P.676-9 (February). Geneva, Switzerland.

Rogers, L. T., C. P. Hattan, and J. K. Stapleton. 2000. "Estimating Evaporation Duct Heights from Radar Sea Echo," *Radio Science 35(4)*:955–966.

Rogers, L.T. 1996. "Remote Sensing of Evaporation Ducts using SHF Propagation Measurements." *Proceedings of AGARD SPP Symposium on Remote Sensing: A Valuable Source of Information* AGARD CP-582 (October), pp. 7.1–7.13. 22–25 April, Toulouse, France.

Seity, Y., P. Brousseau, S. Malardel, G. Hello, P. Bénard, F. Bouttier, C. Lac, and V. Masson. 2011. "The AROME-France Convective-Scale Operational Model," *Monthly Weather Review 139 (3)*:976–991.

Smith, T. A., R. A. Allard, and S. N. Carrol, 2014., "COAMPS Version 3 Model Description: General Theory and Equations." Naval Research Laboratory Marine Meteorology Division, NRL/PU/7500–03–448. Stennis Space Center, MS. Available online at https://www.researchgate.net/publication/235111995_User's_Guide_for_the_Coupled_OceanAtmospheric_Mesoscale_Prediction_System_COAMPS_Version_50. Accessed 7 September 2016.

Smith, T. A., R. A. Allard, and S. N. Carrol. 2010. "Global Data Assimilation System (GDAS)." National Oceanic and Atmospheric Administration. National Centers for Environmental Information. Available online at https://www.ncdc.noaa.gov/data-access/model-data/model-datasets/global-data-assimilation-system-gdas. Accessed 7 September 2016.

APPENDIX A
ADDITIONAL CHARTS, AND TABLE

A.1 OVERVIEW

Appendix A has test results for 5 areas tested. Results are shown in two formats, line charts and a table. Line charts are presented in Figures A-1 to A-42. Radiosonde profiles of Rotte tug at UTC and onshore, shore and tug evaporation duct refractivity profiles, evaporation duct refractivity profile based on tug TACMET data, cumulative distribution functions of observed and predicted propagation for all initialization times, and forecast times prior and following each FRISC outbound and inbound run from COAMPS and HARMONIE, and Table A-1 lists theNWP forecast and initialization times prior and after FRISC start times.

A.2 RADIOSONDE PROFILES OF ROTTE TUG AT UTC AND ONSHORE

Figures A-1 to A-26 show line charts comparing radiosonde profiles of pressure, temperature, humidity, and gaseous attenuation rates from tests conducted on the Rotte tug.
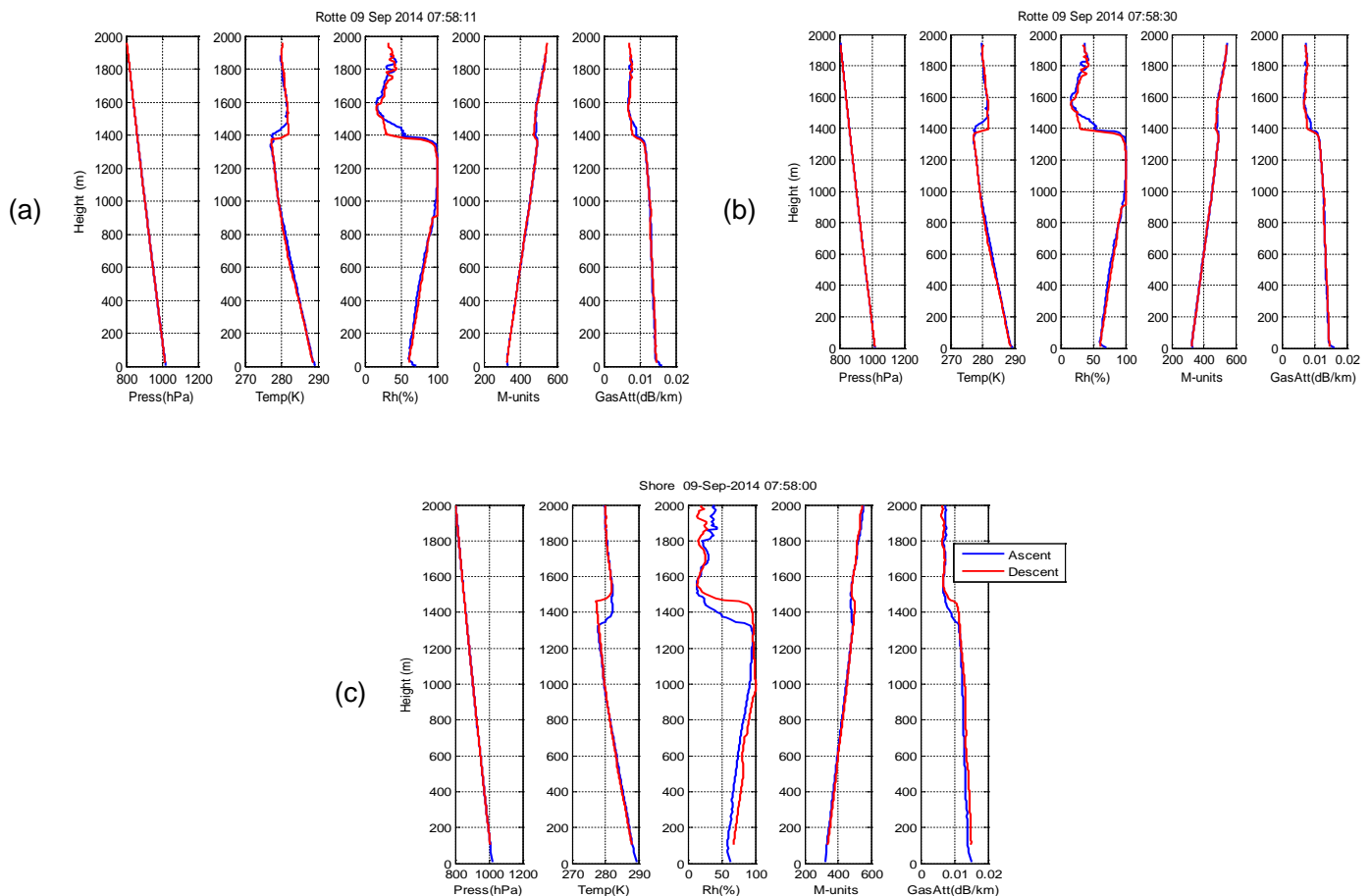
Figure A-1. 9 Sep 2014 radiosonde profiles of pressure, temperature, humidity, M-units, and gaseous attenuation rates from the Rotte tug at (a) 07:58:11UTC, and (b) 07:58:30 UTC; and (c) from onshore at 07:58:00 UTC.
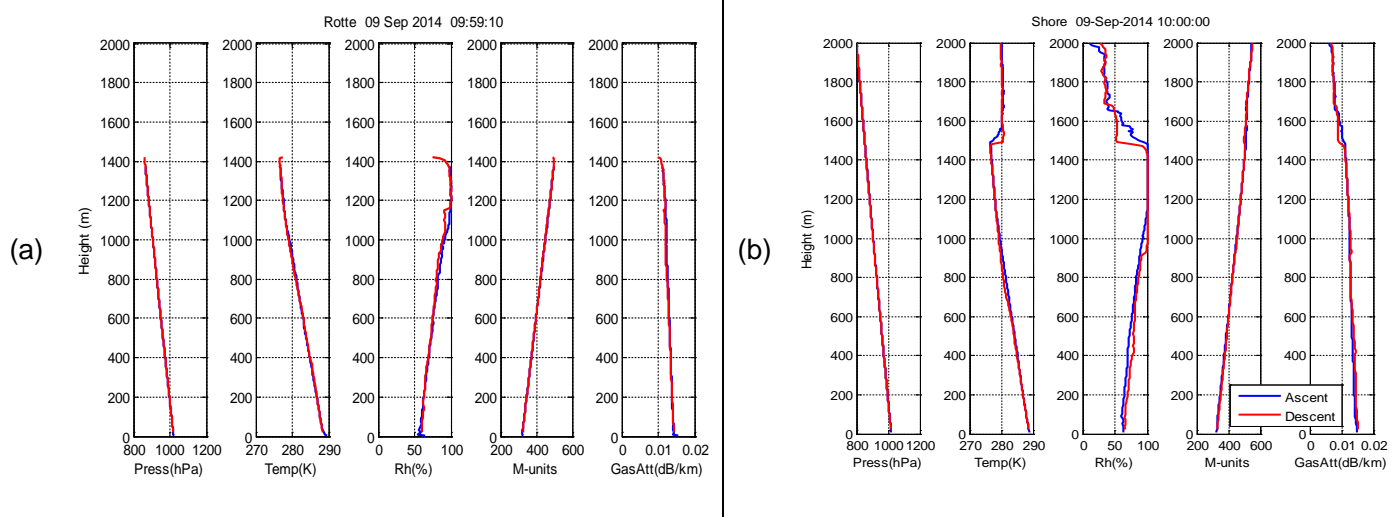
Figure A-2. 9 Sep 2014 radiosonde profiles of pressure, temperature, humidity, M-units, and gaseous attenuation rates from (a) the Rotte tug at 09:59:10 UTC, and (b) onshore at 10:00:00 UTC.
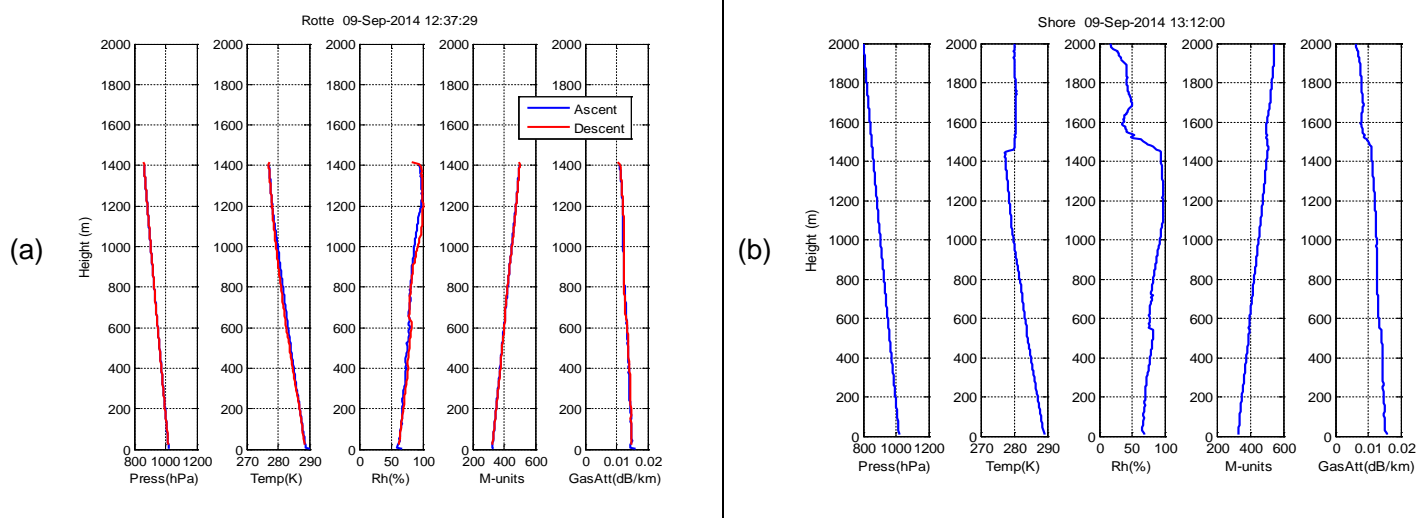
Figure A-3. 9 Sep 2014 radiosonde profiles of pressure, temperature, humidity, M-units, and gaseous attenuation rates from (a) the Rotte tug at 12:37:29 UTC, and (b) onshore at 13:12:00 UTC.
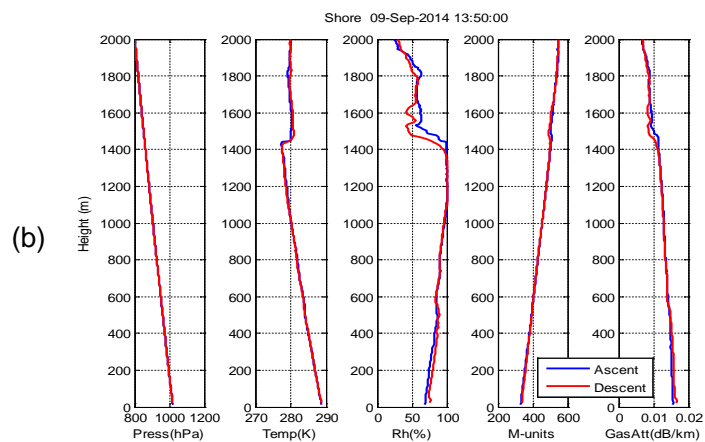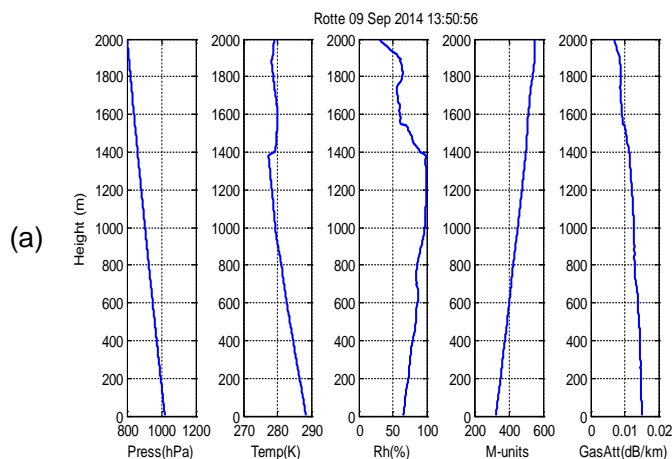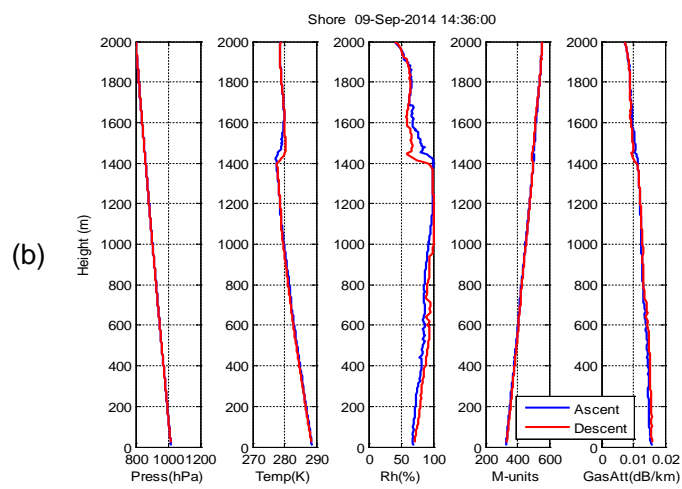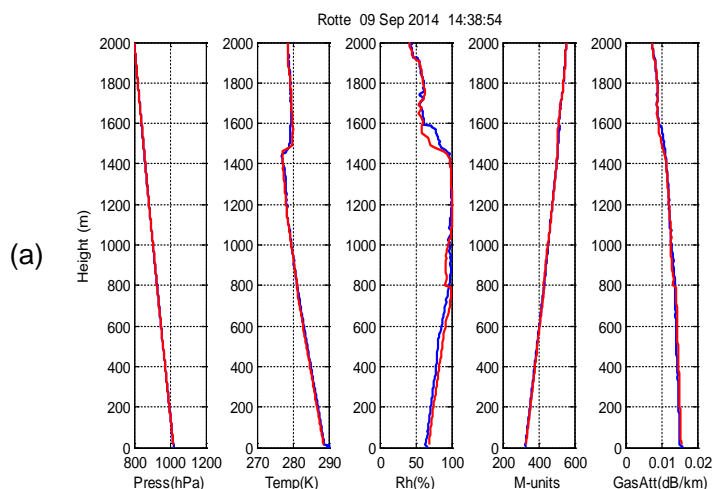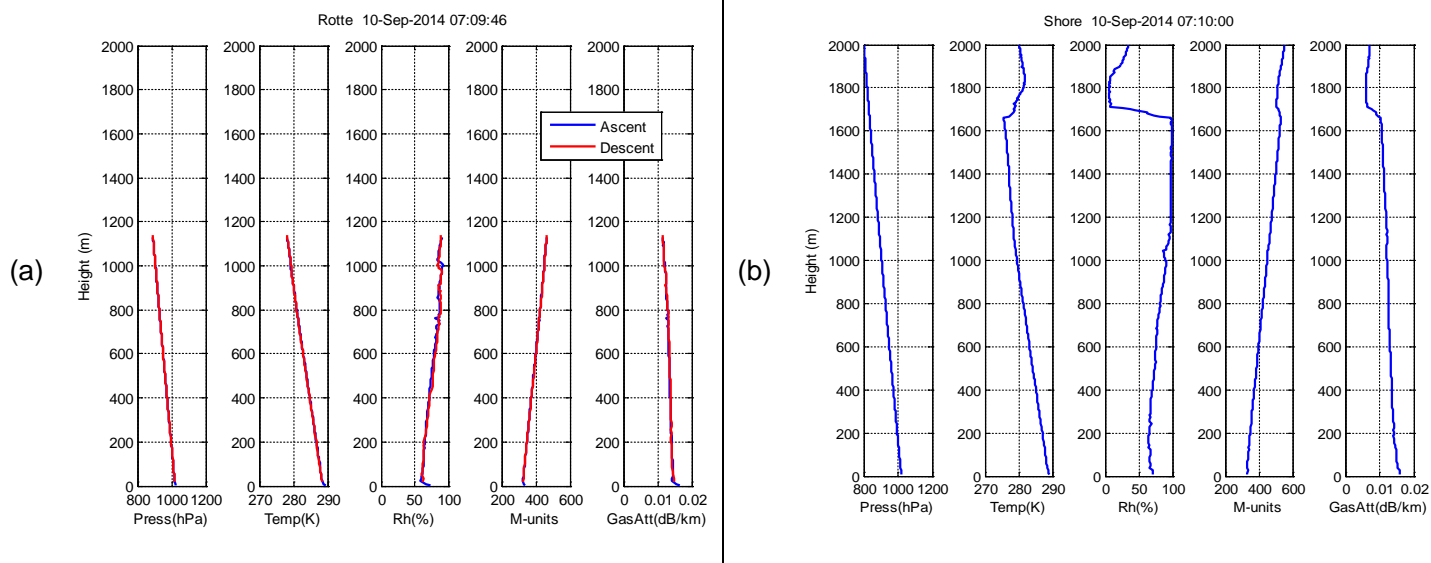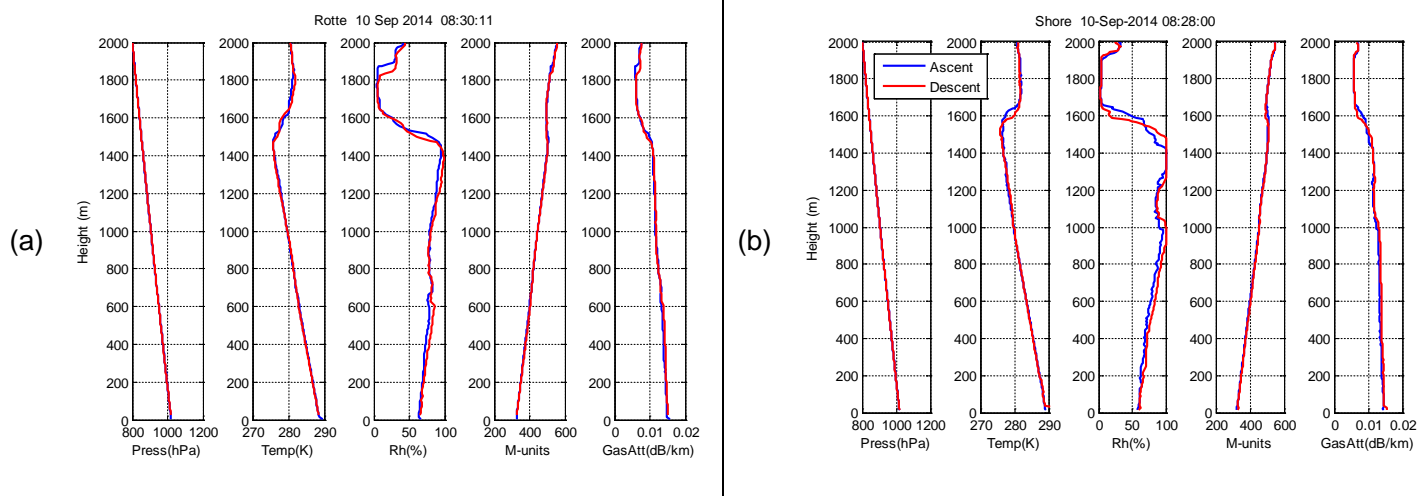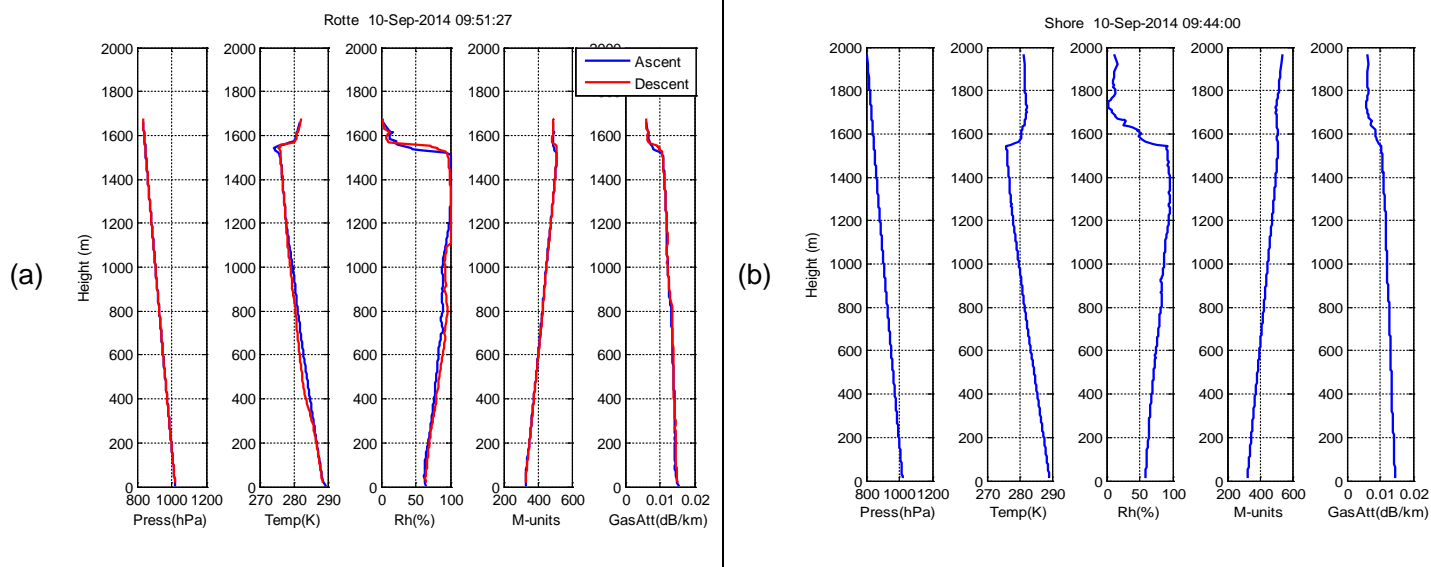
Figure A-4. 9 Sep 2014 radiosonde profiles of pressure, temperature, humidity, M-units, and gaseous attenuation rates from (a) the Rotte tug at 13:50:56 UTC, and (b) onshore at 13:50:00 UTC.

Figure A-5. 9 Sep 2014 radiosonde profiles of pressure, temperature, humidity, M-units, and gaseous attenuation rates from (a) the Rotte tug at 14:38:54 UTC, and (b) onshore at 14:36:00 UTC.
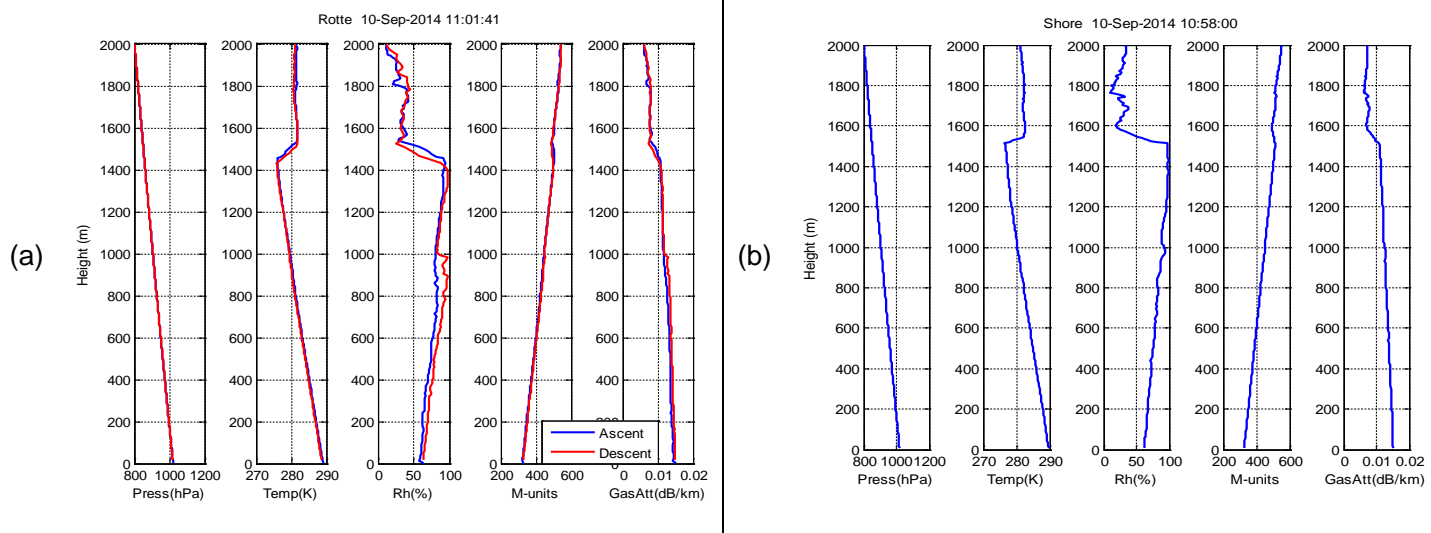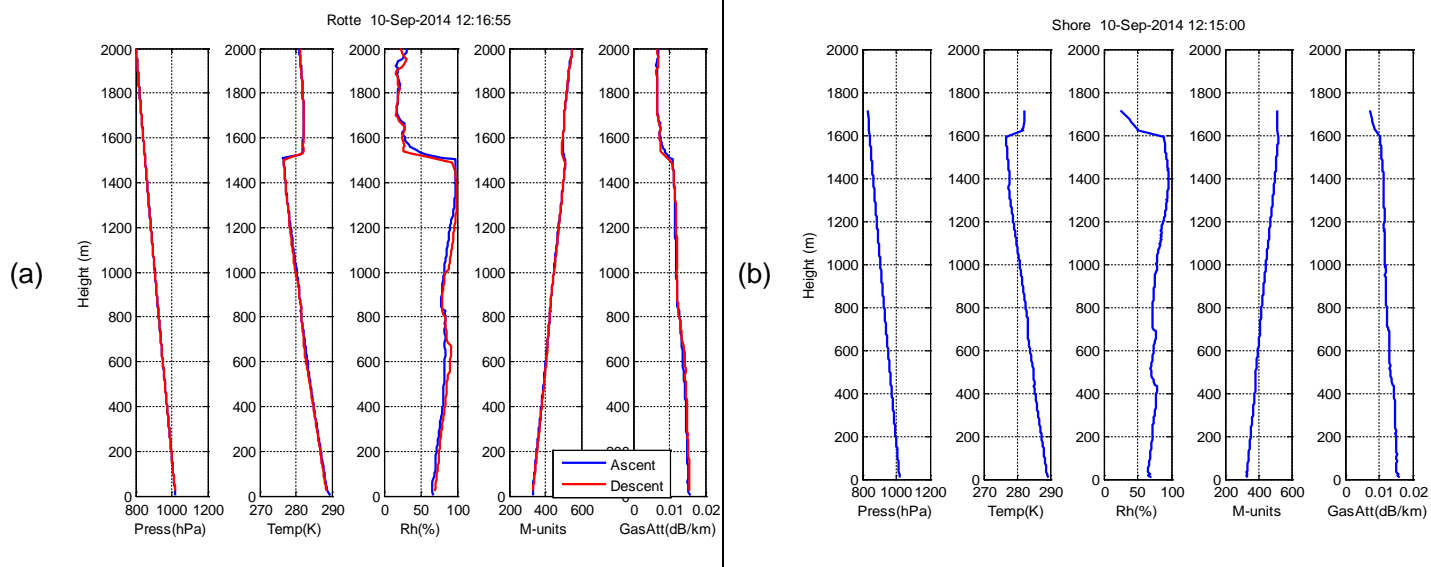
Figure A-6. 10 Sep 2014 radiosonde profiles of pressure, temperature, humidity, M-units, and gaseous attenuation rates from (a) the Rotte tug at 07:09:46 UTC, and (b) onshore at 07:10:00 UTC.

Figure A-7. 10 Sep 2014 radiosonde profiles of pressure, temperature, humidity, M-units, and gaseous attenuation rates from (a) the Rotte tug at 08:30:11 UTC, and (b) onshore at 08:38:00 UTC.

Figure A-8. 10 Sep 2014 radiosonde profiles of pressure, temperature, humidity, M-units, and gaseous attenuation rates from (a) the Rotte tug at 09:51:27 UTC, and (b) onshore at 09:44:00 UTC.
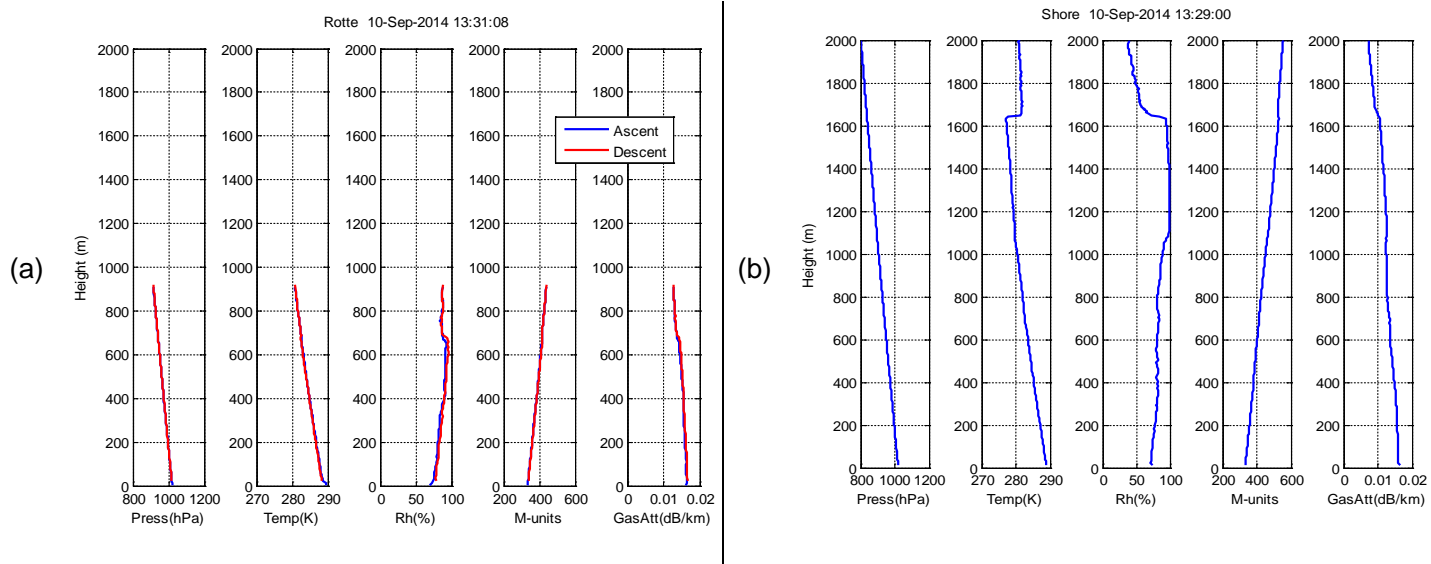

Figure A-9. 10 Sep 2014 radiosonde profiles of pressure, temperature, humidity, M-units, and gaseous attenuation rates from (a) the Rotte tug at 11:01:41 UTC, and (b) onshore at 10:58:00 UTC.

Figure A-10. 10 Sep 2014 radiosonde profiles of pressure, temperature, humidity, M-units, and gaseous attenuation rates from (a) the Rotte tug at 12:16:55 UTC, and (b) onshore at 12:15:00 UTC.

Figure A-11. 10 Sep 2014 radiosonde profiles of pressure, temperature, humidity, M-units, and gaseous attenuation rates from (a) the Rotte tug at 13:31:08 UTC, and (b) onshore at 13:29:00 UTC.
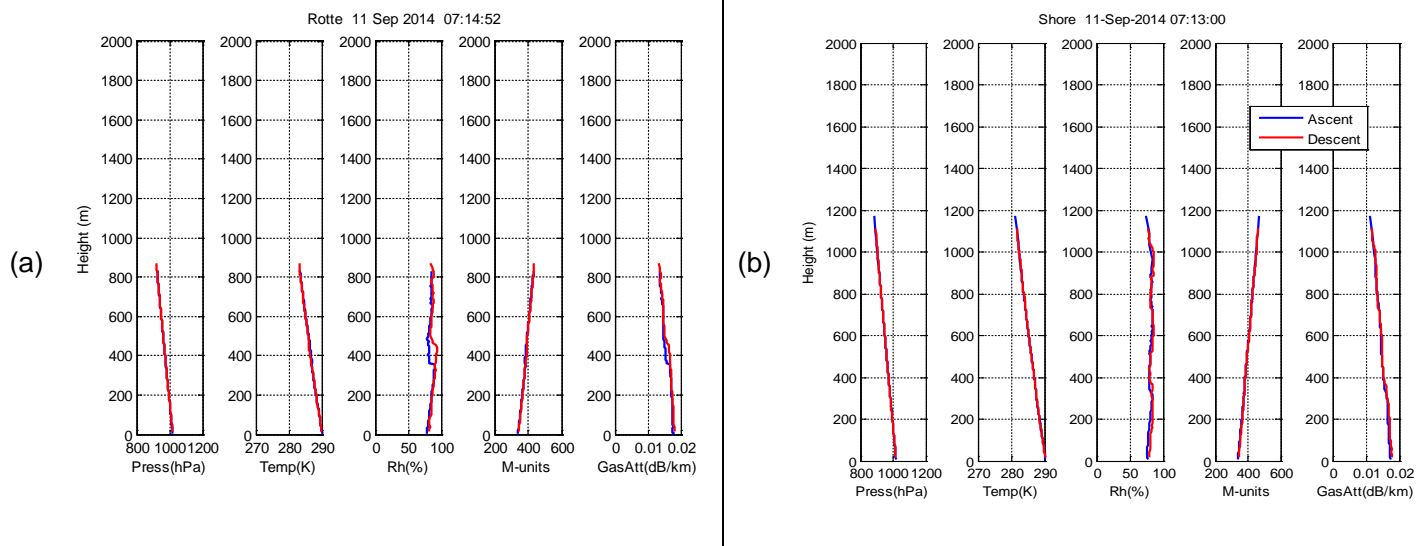
Figure A-12. 11 Sep 2014 radiosonde profiles of pressure, temperature, humidity, M-units, and gaseous attenuation rates from (a) the Rotte tug at 07:14:52 UTC, and (b) onshore at 07:13:00 UTC.
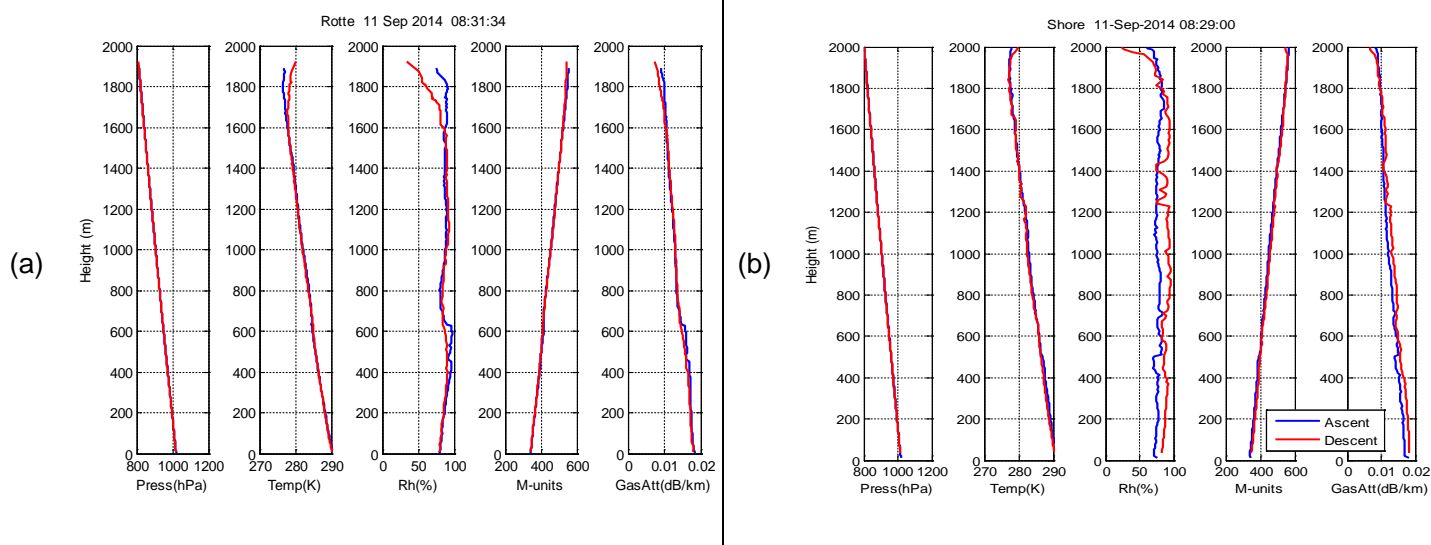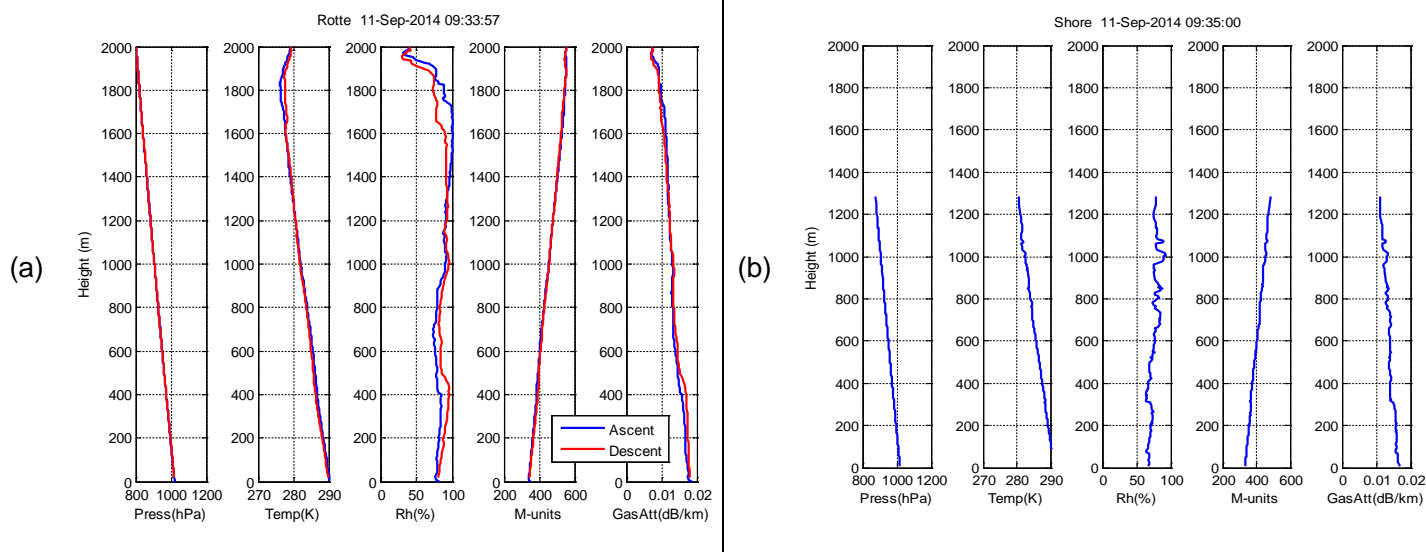

Figure A-13. 11 Sep 2014 radiosonde profiles of pressure, temperature, humidity, M-units, and gaseous attenuation rates from (a) the Rotte tug at 08:31:34 UTC, and (b) onshore at 08:29:00 UTC.

Figure A-14. 11 Sep 2014 radiosonde profiles of pressure, temperature, humidity, M-units, and gaseous attenuation rates from (a) the Rotte tug at 09:33:57 UTC, and (b) onshore at 09:35:00 UTC.
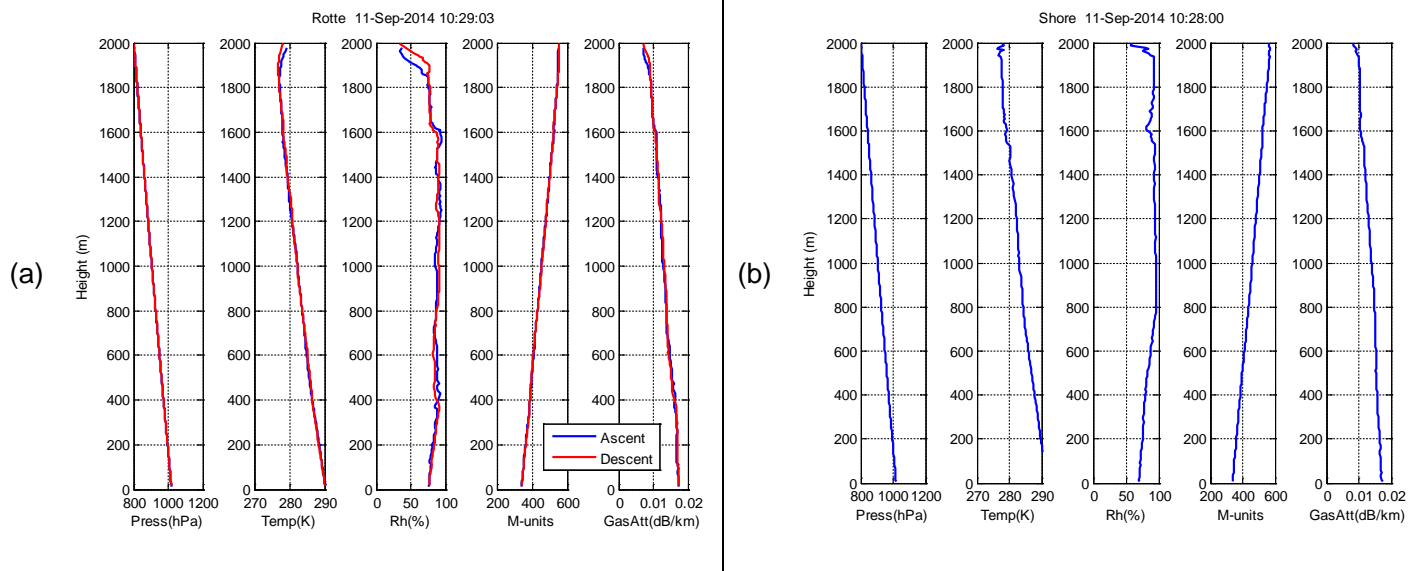

Figure A-15. 11 Sep 2014 radiosonde profiles of pressure, temperature, humidity, M-units, and gaseous attenuation rates from (a) the Rotte tug at 10:29:03 UTC, and (b) onshore at 10:28:00 UTC.
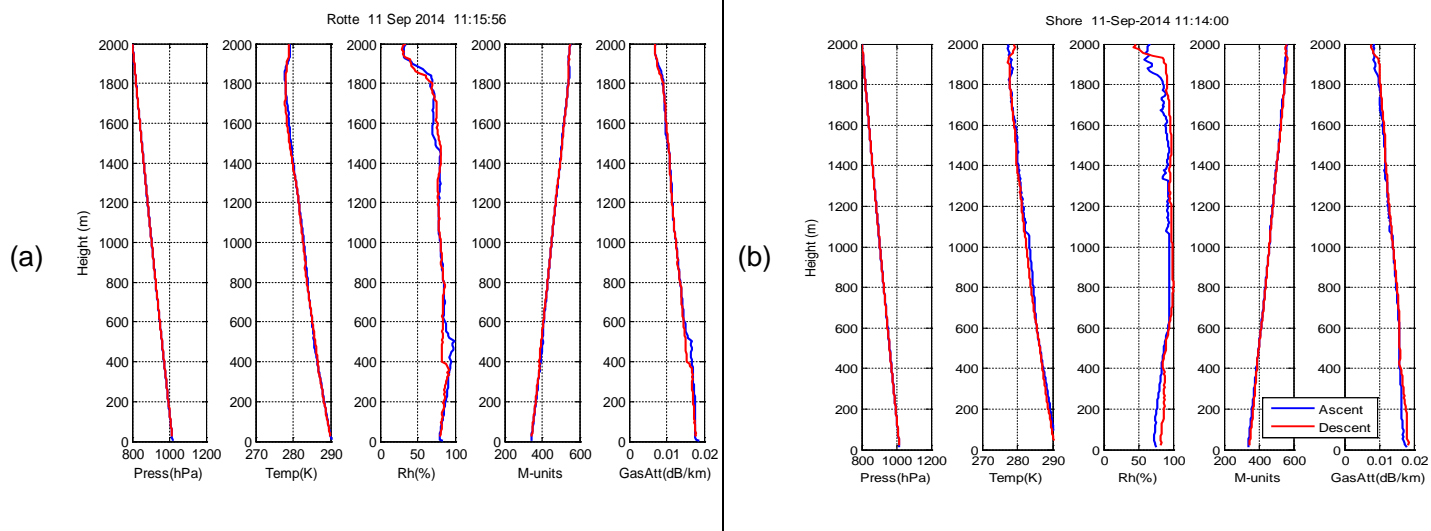
Figure A-16. 11 Sep 2014 radiosonde profiles of pressure, temperature, humidity, M-units, and gaseous attenuation rates from (a) the Rotte tug at 11:15:56 UTC, and (b) onshore at 11:14:00 UTC.
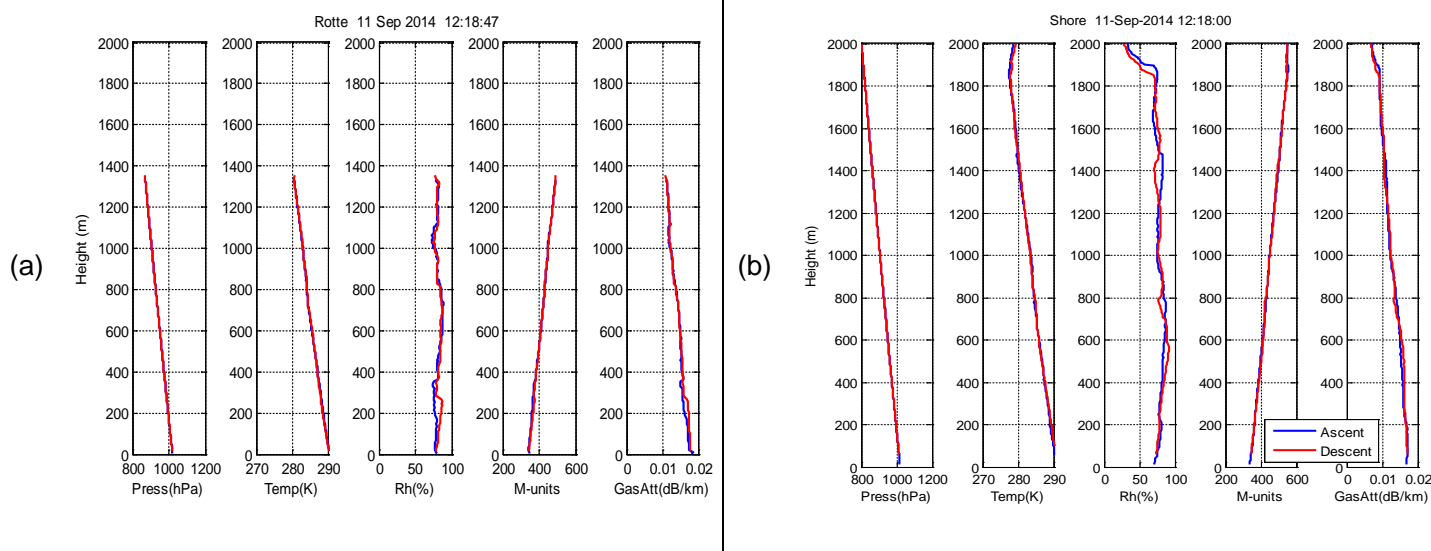

Figure A-17. 11 Sep 2014 radiosonde profiles of pressure, temperature, humidity, M-units, and gaseous attenuation rates from (a) the Rotte tug at 12:18:47 UTC, and (b) onshore at 12:18:00 UTC.
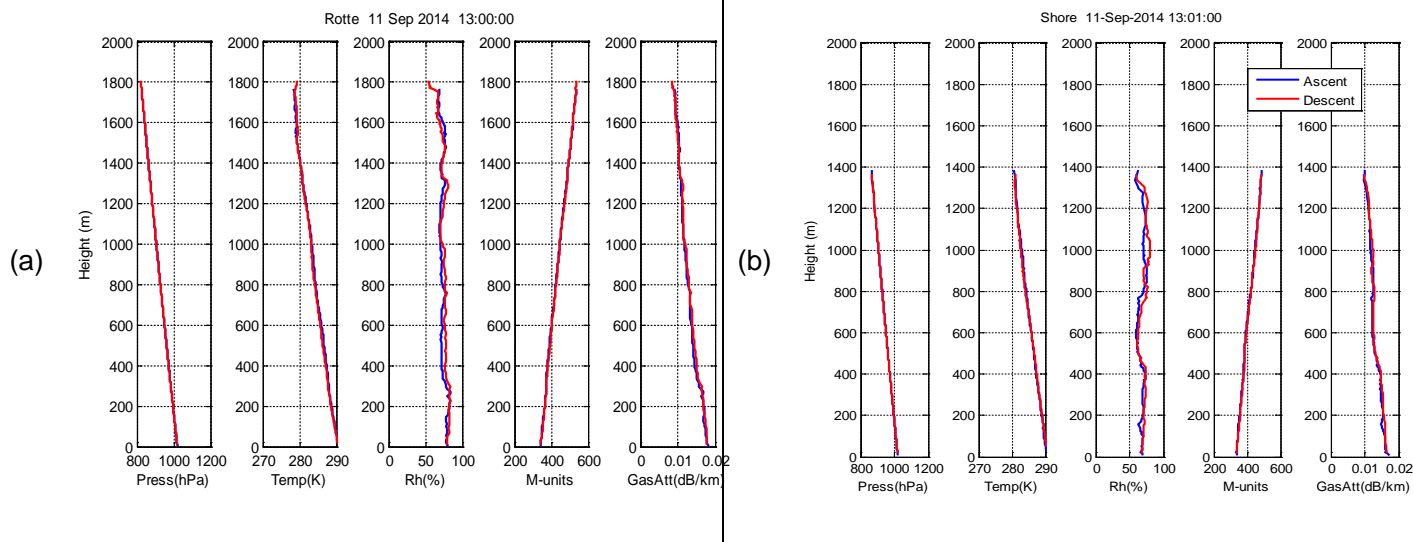
Figure A-18. 11 Sep 2014 radiosonde profiles of pressure, temperature, humidity, M-units, and gaseous attenuation rates from (a) the Rotte tug at 13:00:00 UTC, and (b) onshore at 13:01:00 UTC.
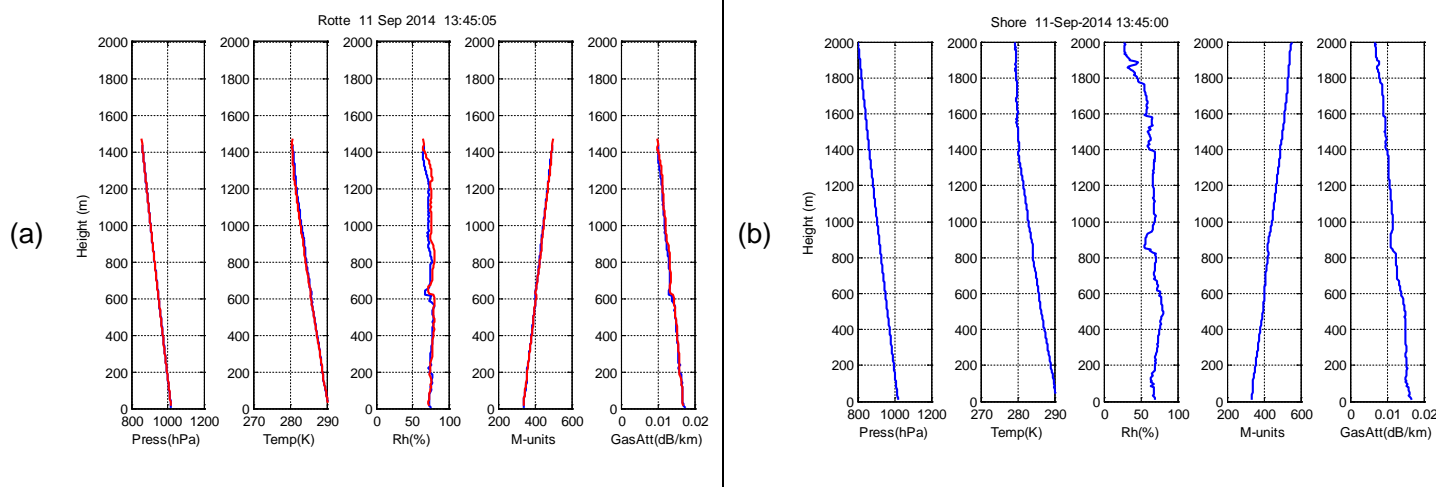

Figure A-19. 11 Sep 2014 radiosonde profiles of pressure, temperature, humidity, M-units, and gaseous attenuation rates from (a) the Rotte tug at 13:45:05 UTC, and (b) onshore at 13:45:00 UTC.
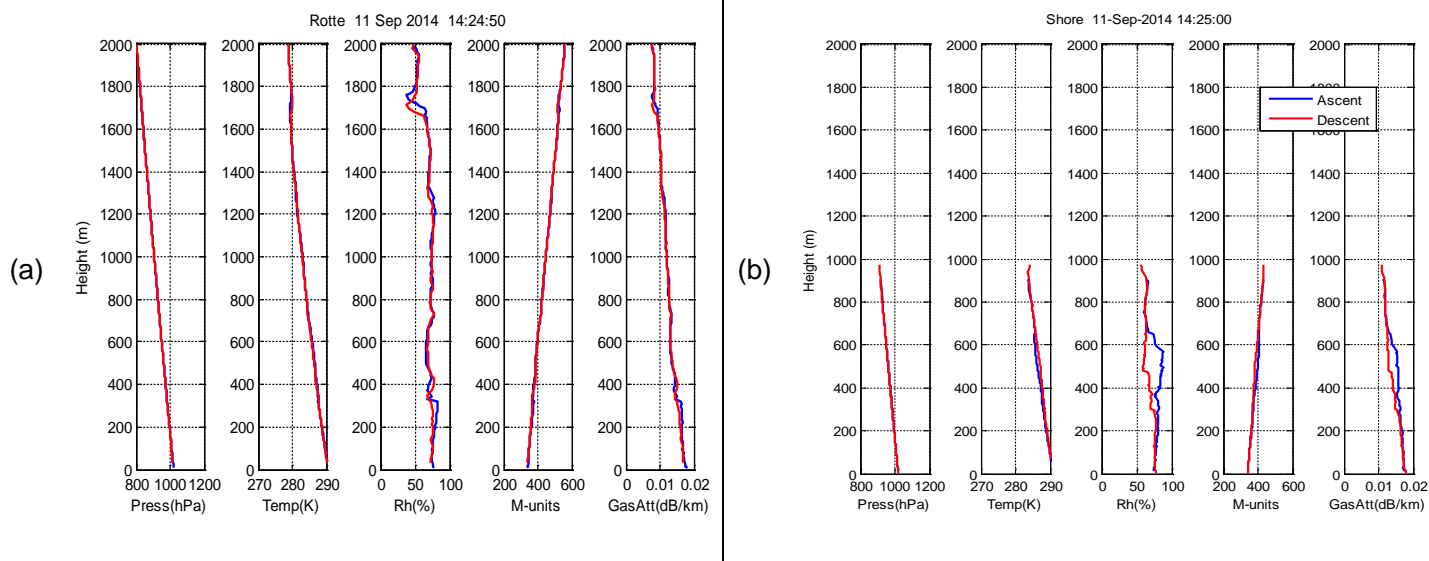
Figure A-20. 11 Sep 2014 radiosonde profiles of pressure, temperature, humidity, M-units, and gaseous attenuation rates from (a) the Rotte tug at 14:24:50 UTC, and (b) onshore at 14:25:00 UTC.

Figure A-21. 11 Sep 2014 radiosonde profiles of pressure, temperature, humidity, M-units, and gaseous attenuation rates from (a) the Rotte tug at 15:15:49 UTC, and (b) onshore at 15:17:00 UTC.
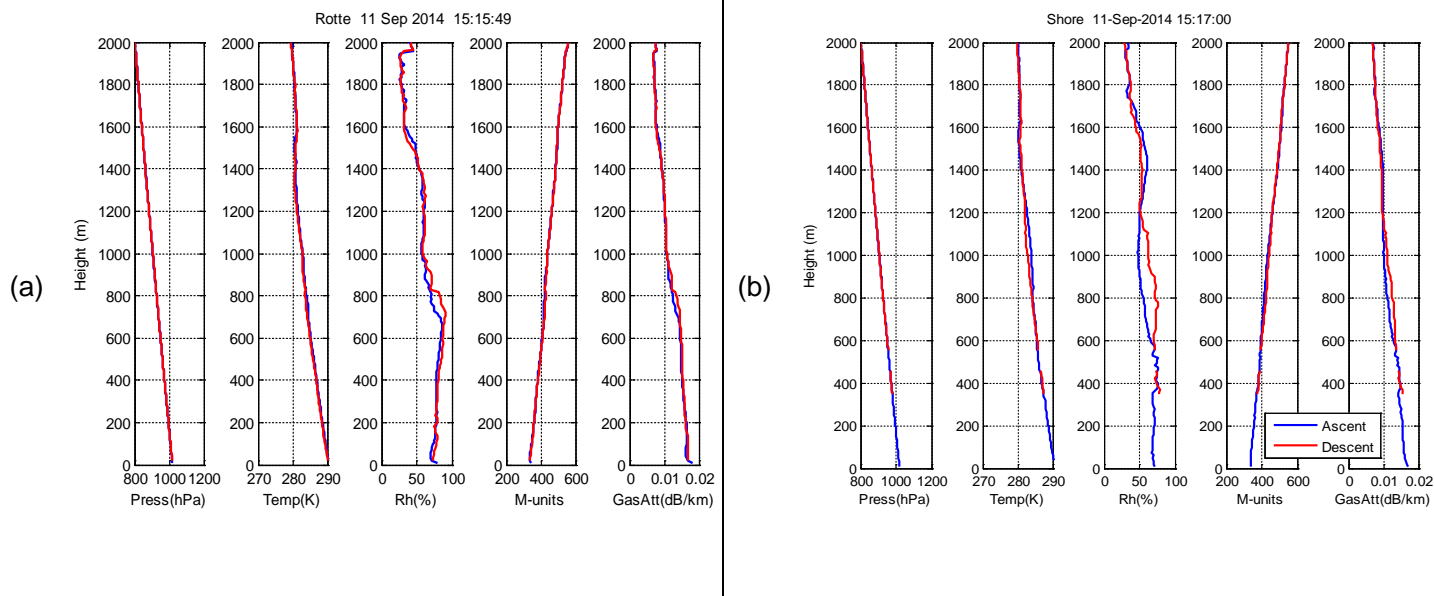
Figure A-22. 11 Sep 2014 radiosonde profiles of pressure, temperature, humidity, M-units, and gaseous attenuation rates from (a) the Rotte tug at 16:12:15 UTC, and (b) onshore at 16:13:00 UTC.
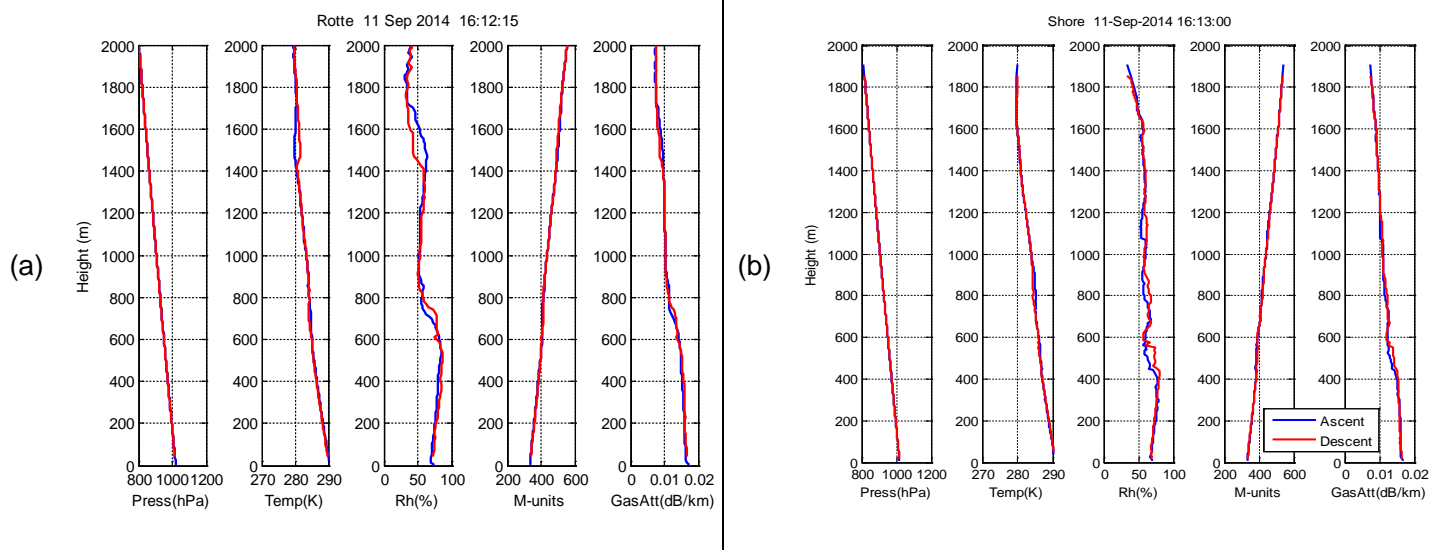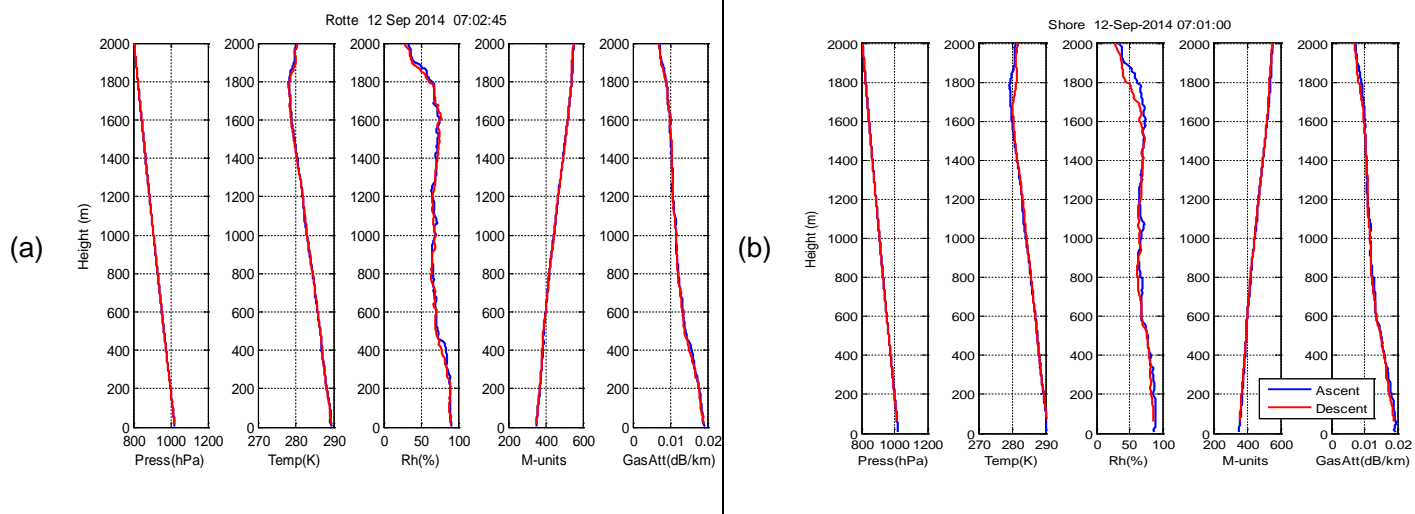

Figure A-23. 12 Sep 2014 radiosonde profiles of pressure, temperature, humidity, M-units, and gaseous attenuation rates from (a) the Rotte tug at 07:02:45 UTC, and (b) onshore at 07:01:00 UTC.

Figure A-24. 12 Sep 2014 radiosonde profiles of pressure, temperature, humidity, M-units, and gaseous attenuation rates from (a) the Rotte tug at 08:03:20 UTC, and (b) onshore 08:03:00 UTC.
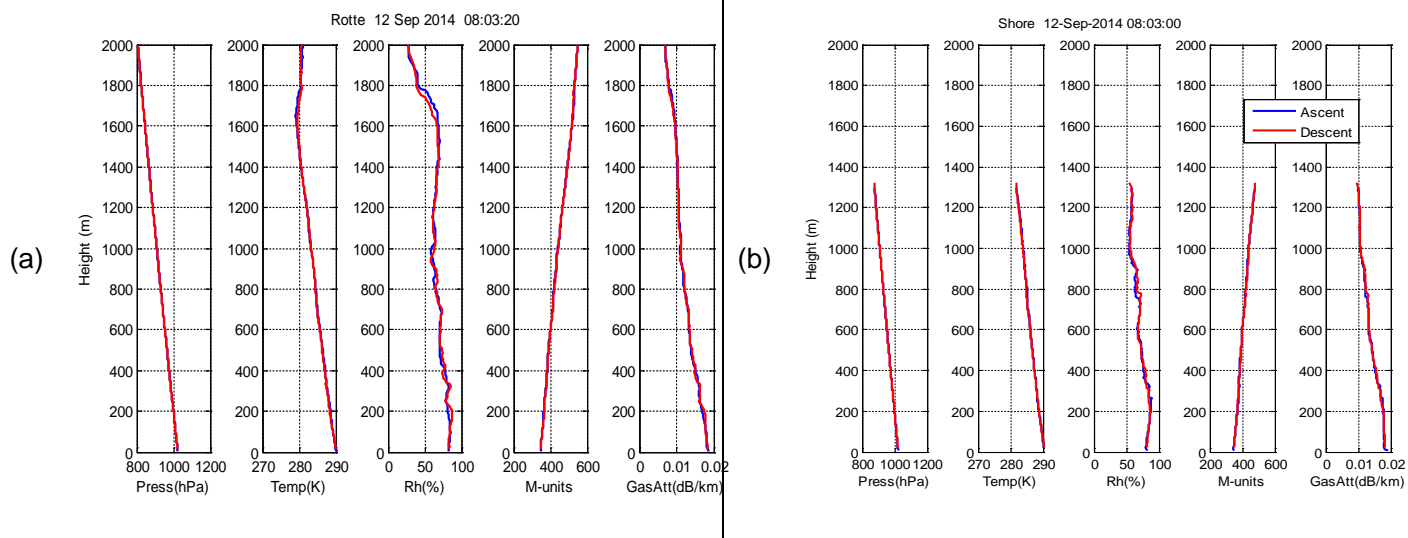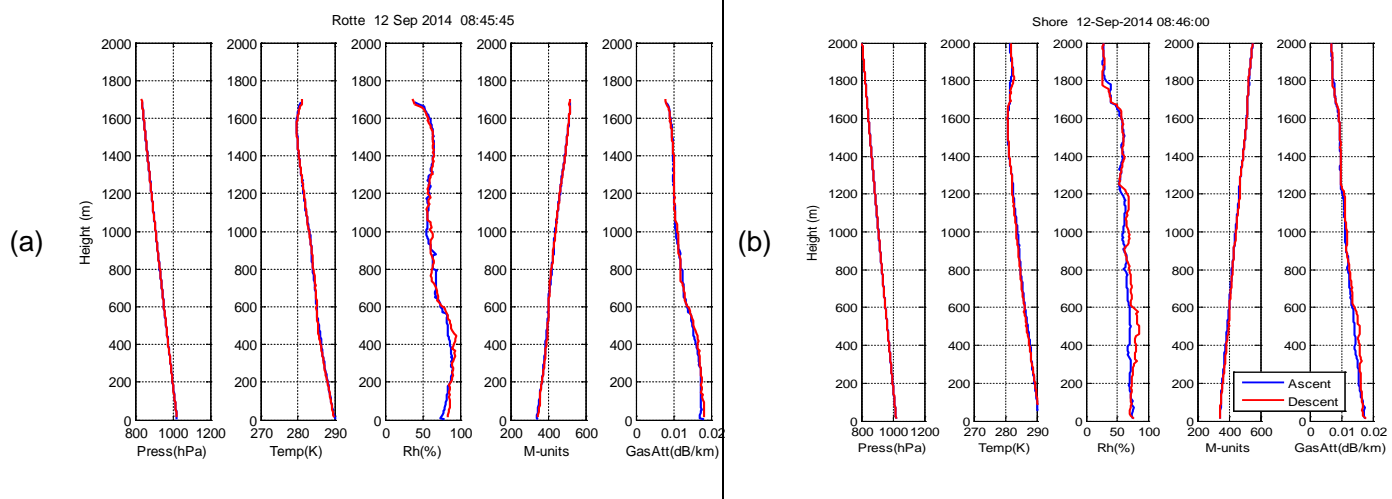

Figure A-25. 12 Sep 2014 radiosonde profiles of pressure, temperature, humidity, M-units, and gaseous attenuation rates from (a) the Rotte tug at 08:45:45 UTC, and (b) onshore at 08:46:00 UTC.
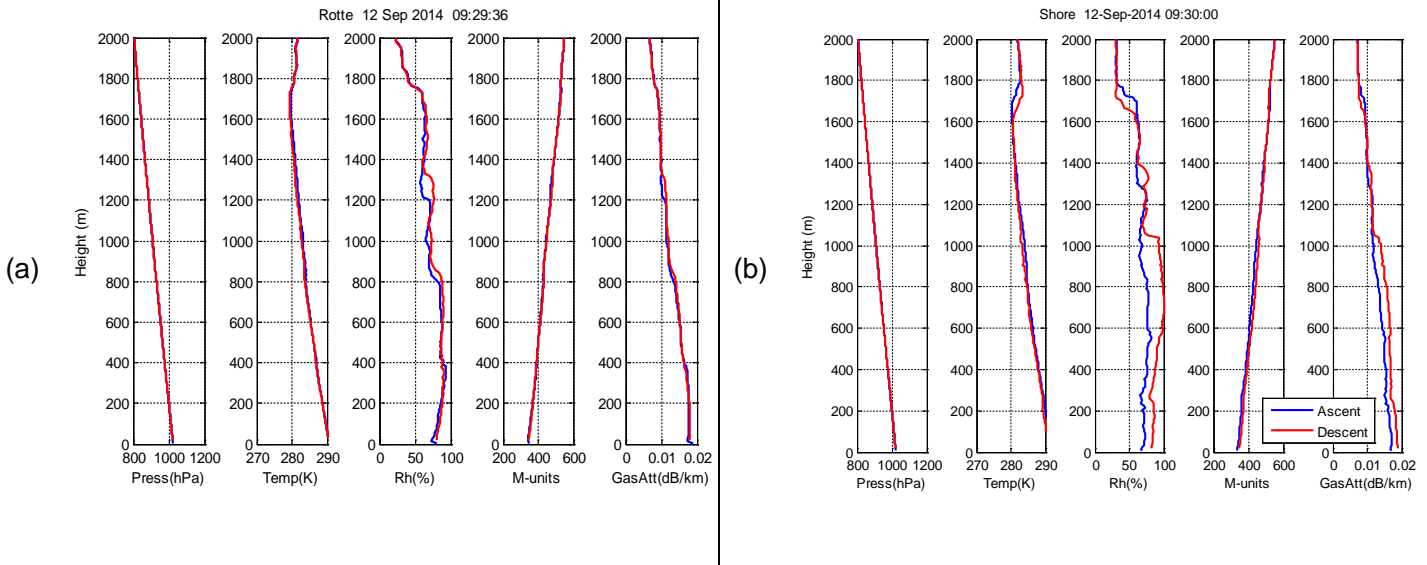
Figure A-26. 12 Sep 2014 radiosonde profiles of pressure, temperature, humidity, M-units, and gaseous attenuation rates from (a) the Rotte tug at 09:29:36 UTC, and (b) onshore 09:30:00 UTC.

A.3 SHORE AND TUG EVAPORATION DUCT REFRACTIVITY PROFILES

Figures A-27 to A-32 show line charts of NAVSLaM shore and tug evaporation duct refractivity profiles computed for times corresponding to inbound and outbound runs.

Figure A-27. Shore and tug evaporation duct refractivity profiles computed for all outbound runs on 9 Sep 2014.

Figure A-28. Shore and tug evaporation duct refractivity profiles computed for all inbound runs on 9 Sep 2014.

Figure A-29. Shore and tug evaporation duct refractivity profiles computed for all outbound runs on 10 Sep 2014.

Figure A-30. Shore and tug evaporation duct refractivity profiles computed for all inbound runs on 10 Sep 2014.
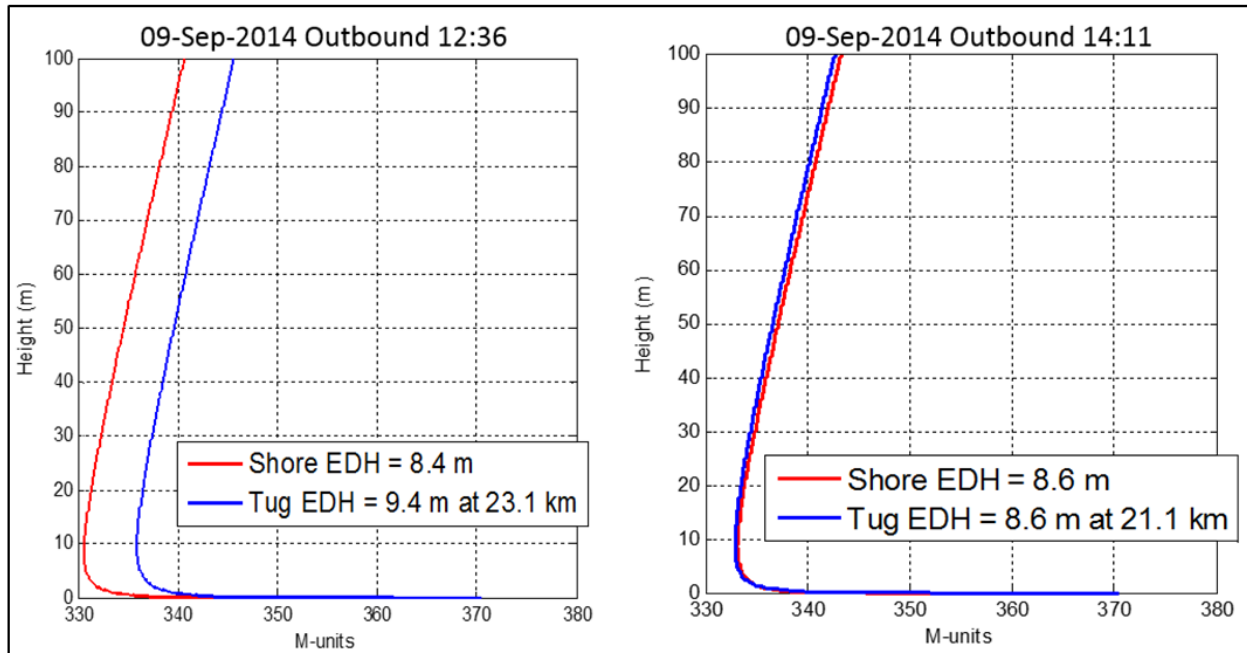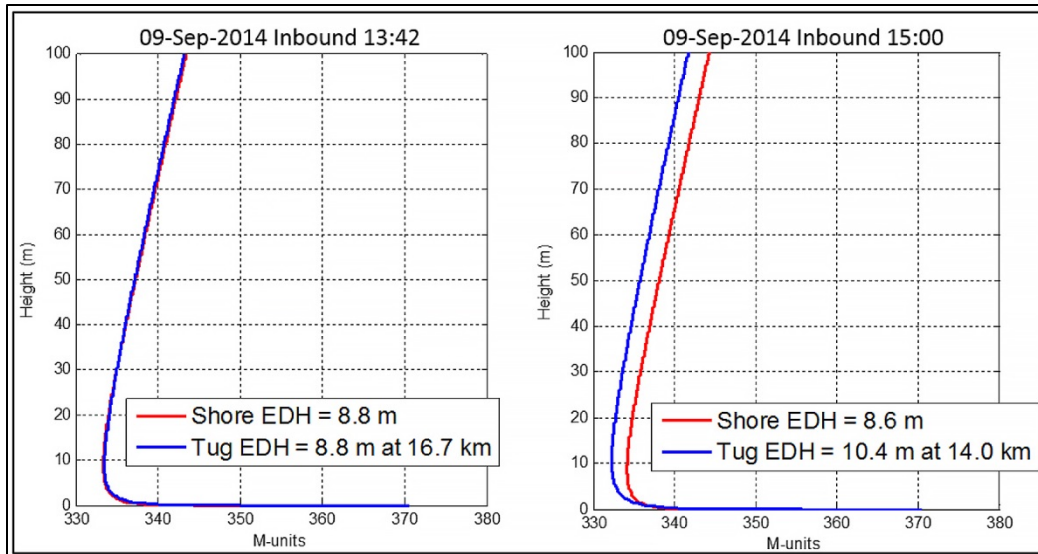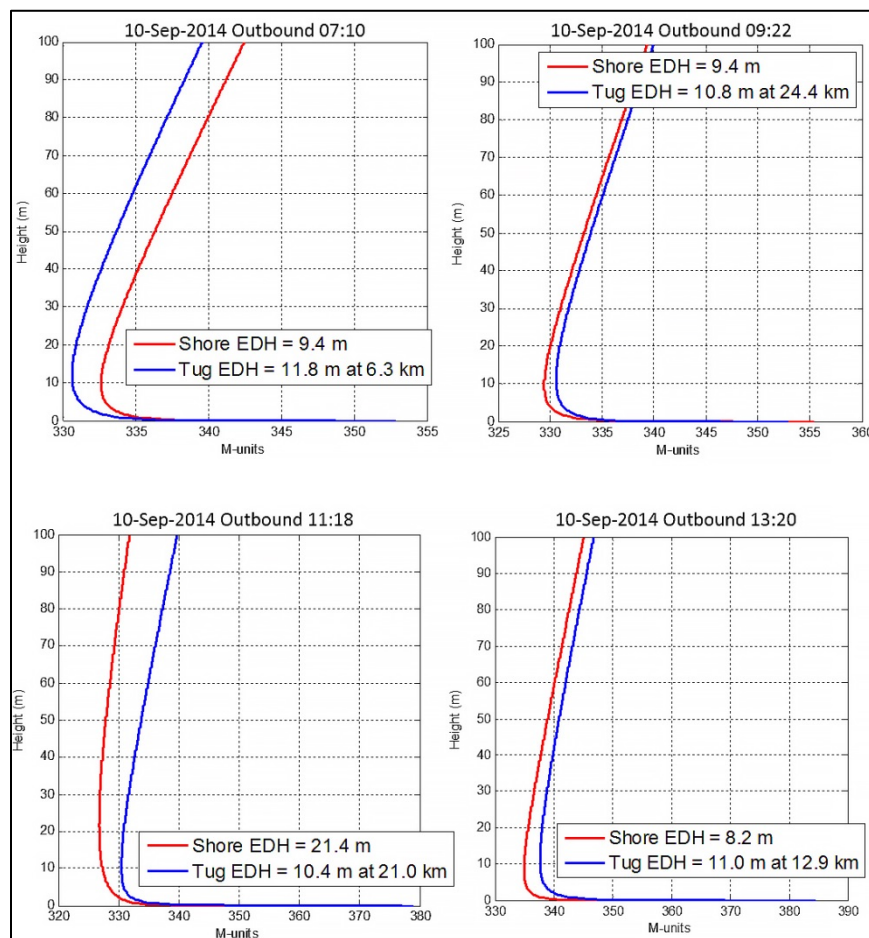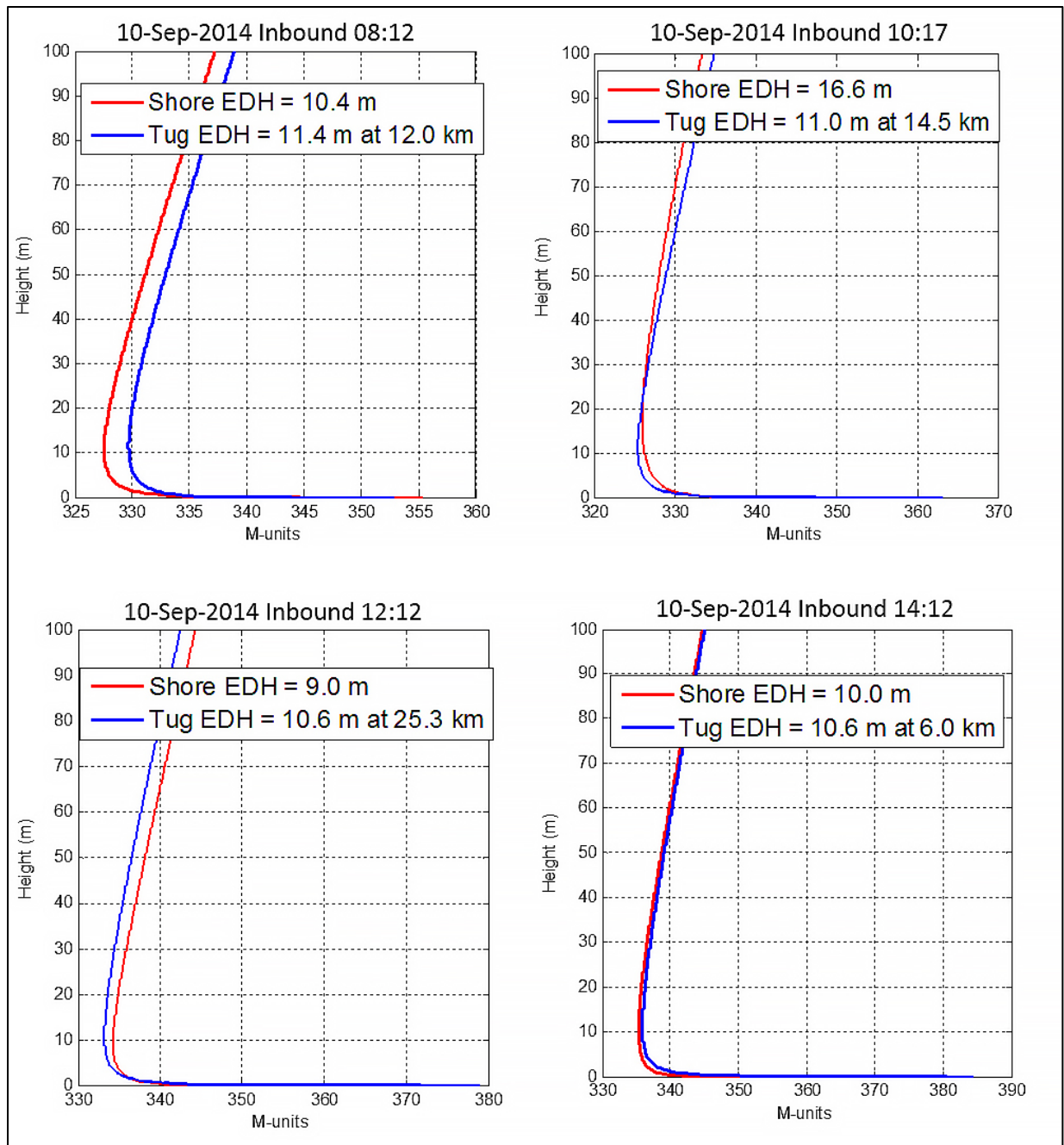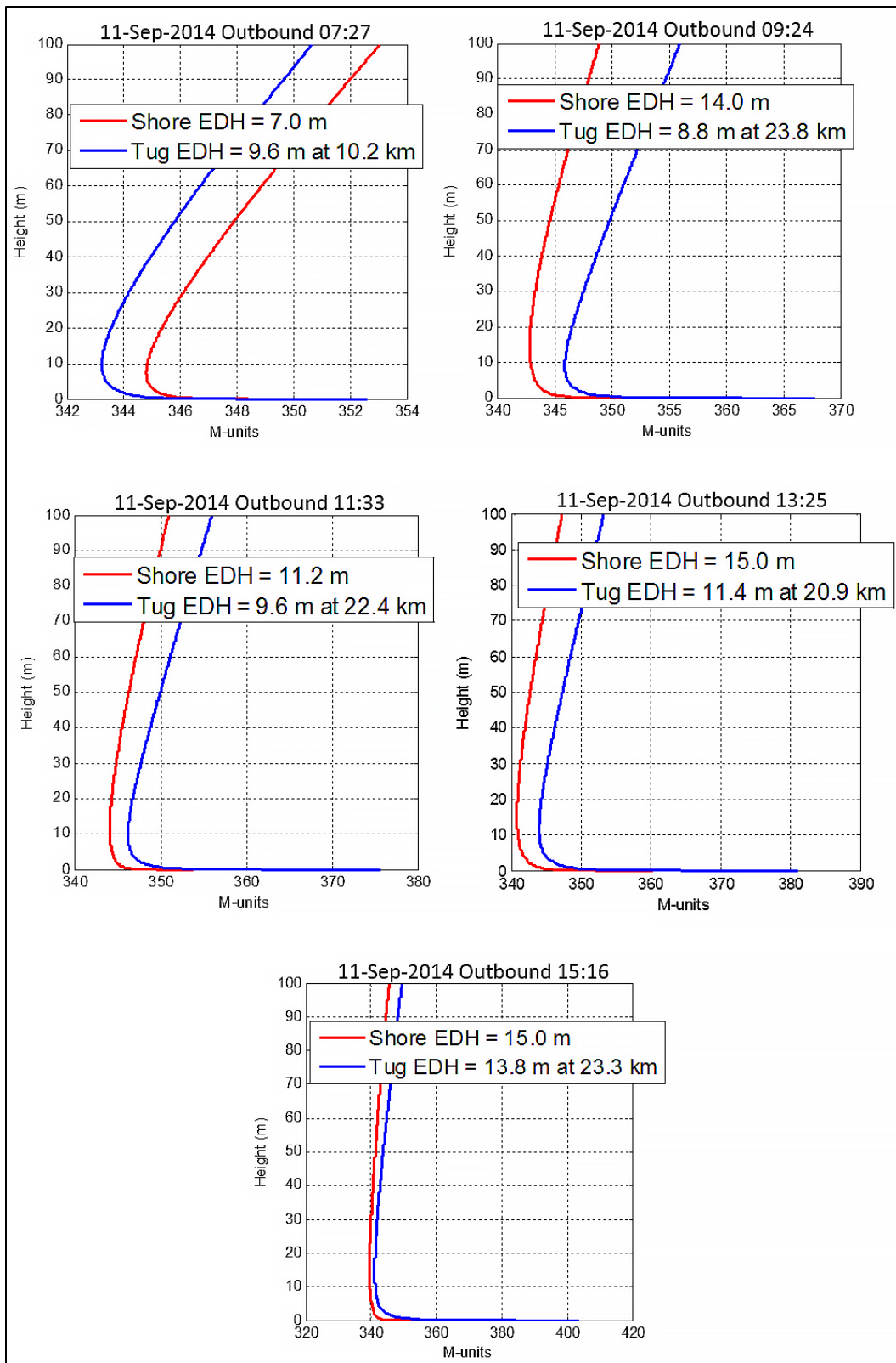
Figure A-31 Shore and tug evaporation duct refractivity profiles computed for all outbound runs on 11 Sep 2014.
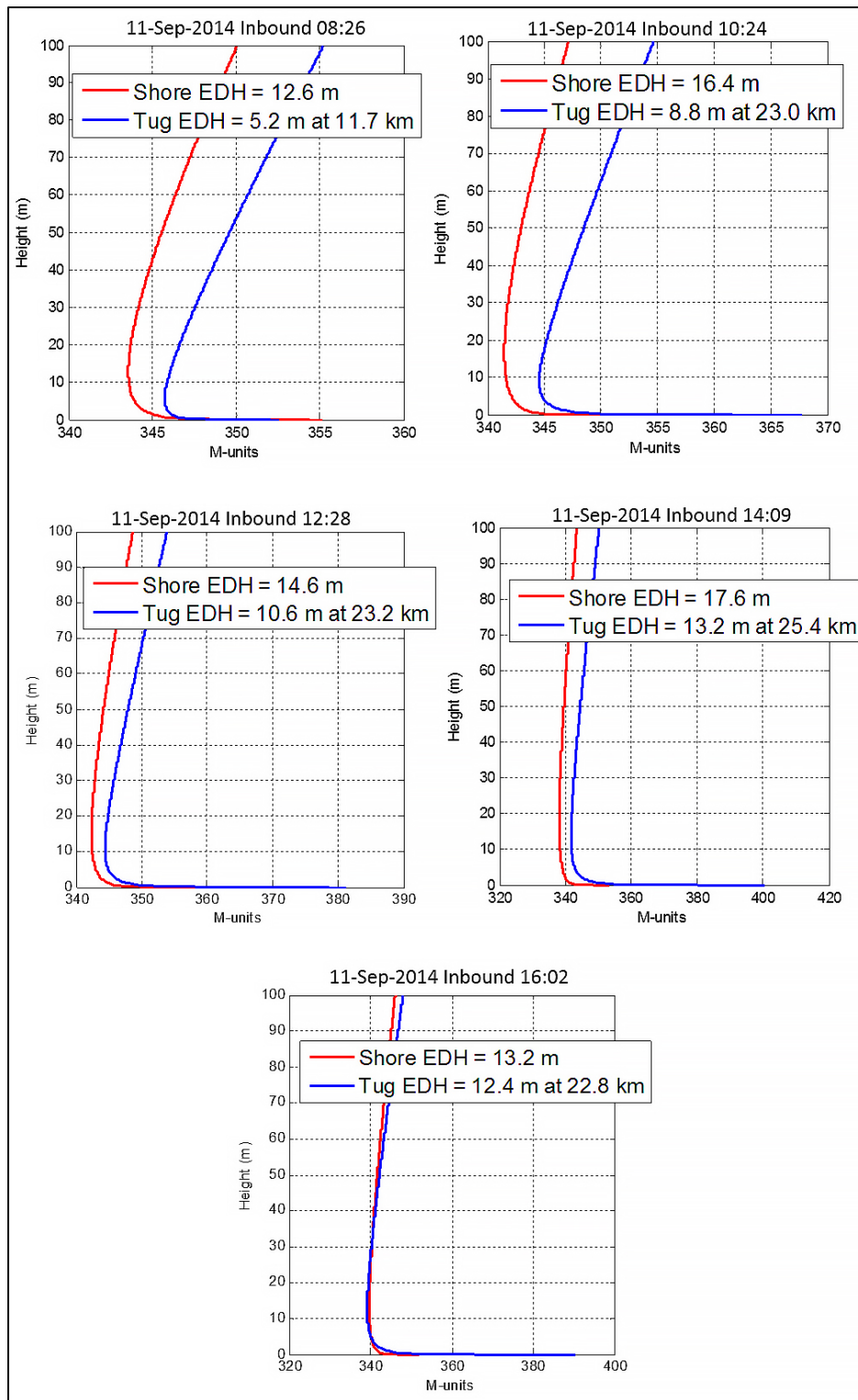
Figure A-32. Shore and tug evaporation duct refractivity profiles computed for all inbound runs on 11 Sep 2014.

A.4 EVAPORATION DUCT REFRACTIVITY PROFILE BASED ON TUG TACMET DATA

Figures A-33 and A-34 show line charts of evaporation duct refractivity profiles based on the tug TACMET data, computed for all times corresponding to mid-path of the FRISC inbound and outbound runs.

Figure A-33. Evaporation duct refractivity profile, based on the tug TACMET data, computed for all outbound runs on 12 Sep 2014.

Figure A-34. Evaporation duct refractivity profile, based on the tug TACMET data, computed for all inbound runs on 12 Sep 2014.
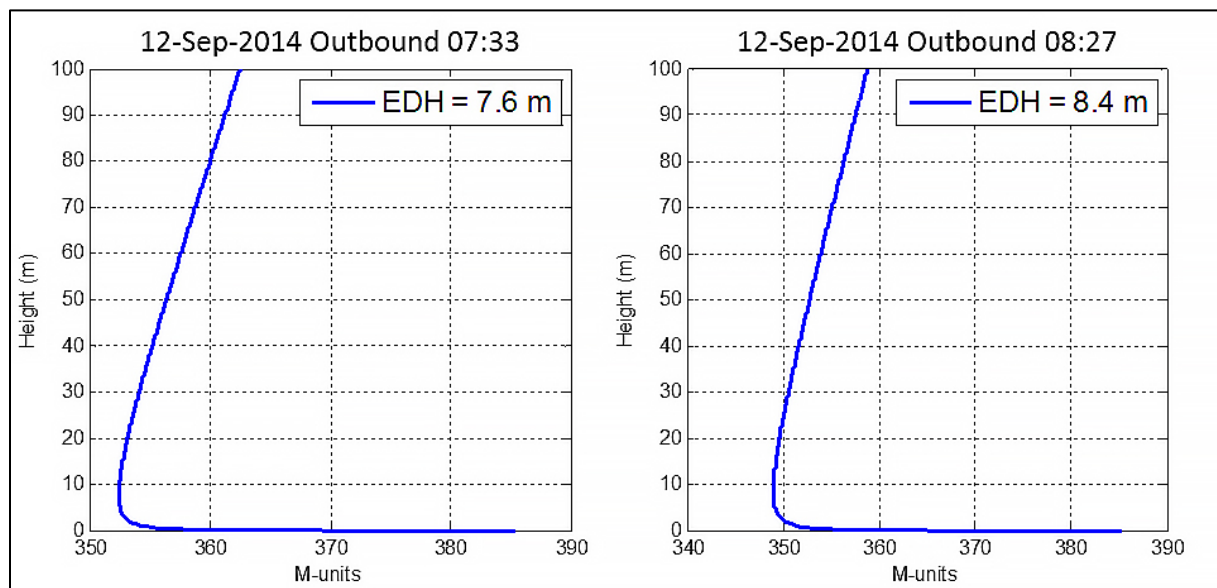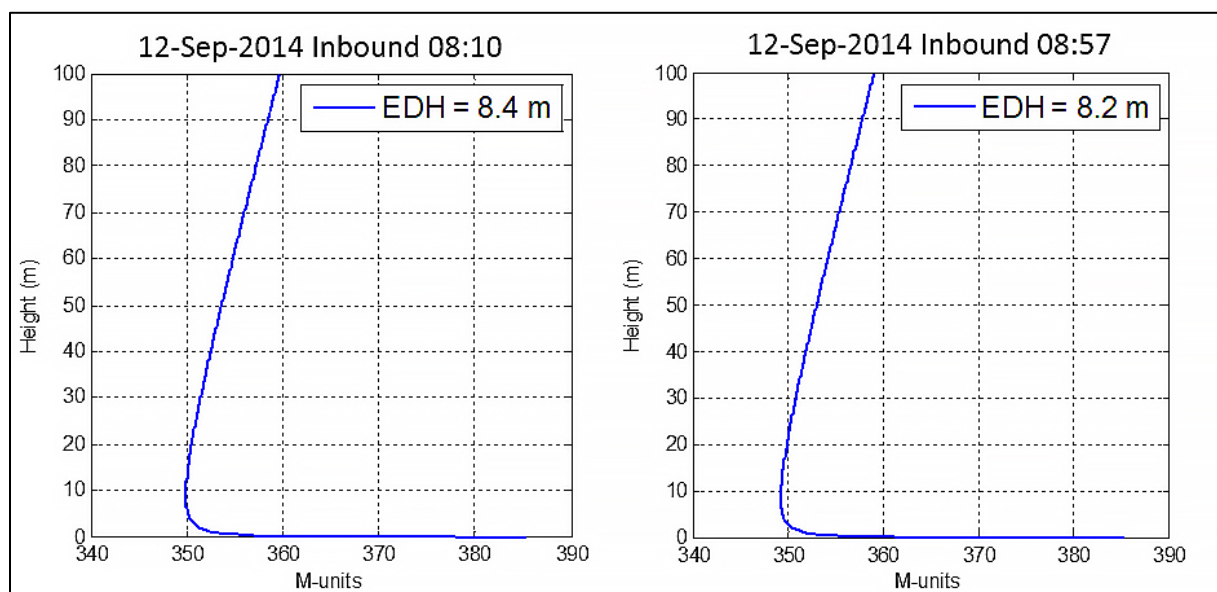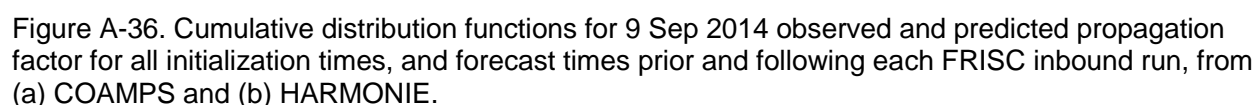
A.5 CUMULATIVE DISTRIBUTION FUNCTIONS OBSERVED AND PREDICTED PROPAGATION PROPAGATION FACTOR FOR ALL INITIALIZATION TIMES, AND FORECAST TIMES PRIOR AND FOLLOWING EACH FRISC OUTBOUND RUN, FROM COAMPS AND HARMONIE

Figures A-35 and A-42 show line charts of test results cumulative distribution functions observed and predicted propagation factor for all initialization times, and forecast times prior and following each FRISC outbound run, from COAMPS and HARMONIE.

Figure A-35. Cumulative distribution functions for 9 Sep 2014 observed and predicted propagation factor for all initialization times, and forecast times prior and following each FRISC outbound run, from (a) COAMPS and (b) HARMONIE.

Figure A-36. Cumulative distribution functions for 9 Sep 2014 observed and predicted propagation factor for all initialization times, and forecast times prior and following each FRISC inbound run, from (a) COAMPS and (b) HARMONIE.
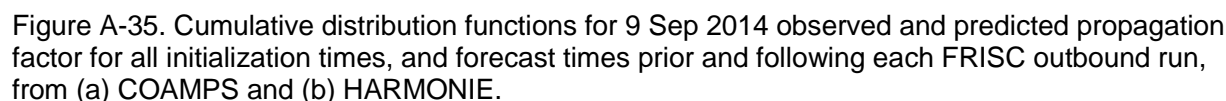
Figure A-37. Cumulative distribution functions for 10 Sep 2014 observed and predicted propagation factor for all initialization times, and forecast times prior and following each FRISC outbound run, from (a) COAMPS and (b) HARMONIE.

Figure A-38. Cumulative distribution functions for 10 Sep 2014 observed and predicted propagation factor for all initialization times, and forecast times prior and following each FRISC inbound run, from (a) COAMPS and (b) HARMONIE.
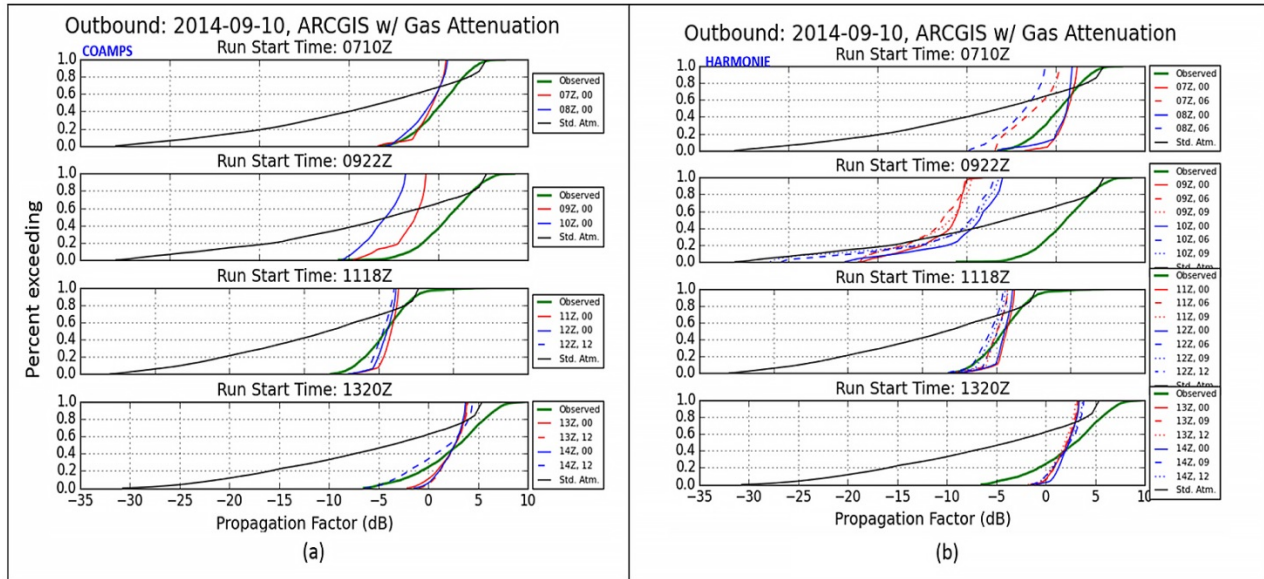
Figure A-39. Cumulative distribution functions for 11 Sep 2014 observed and predicted propagation factor for all initialization times, and forecast times prior and following each FRISC outbound run, from (a) COAMPS and (b) HARMONIE.

Figure A-40. Cumulative distribution functions for 11 Sep 2014 observed and predicted propagation factor for all initialization times, and forecast times prior and following each FRISC inbound run, from (a) COAMPS and (b) HARMONIE.
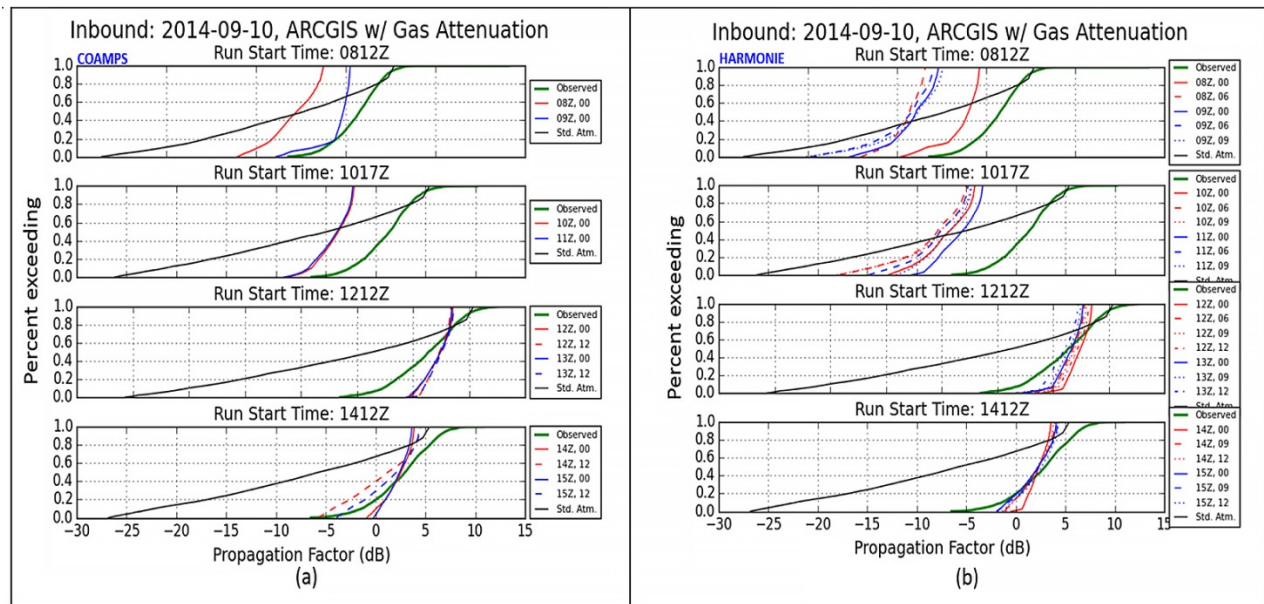
Figure A-41. Cumulative distribution functions for 12 Sep 2014 observed and predicted propagation factor for all initialization times, and forecast times prior and following each FRISC outbound run, from (a) COAMPS and (b) HARMONIE.
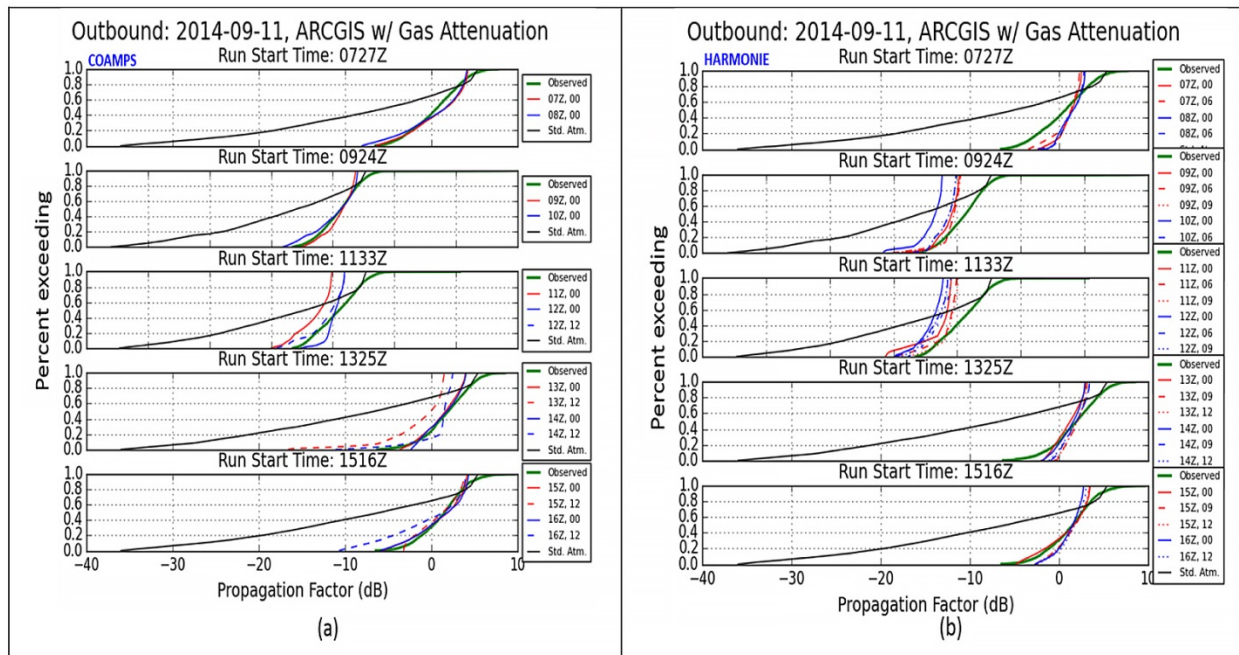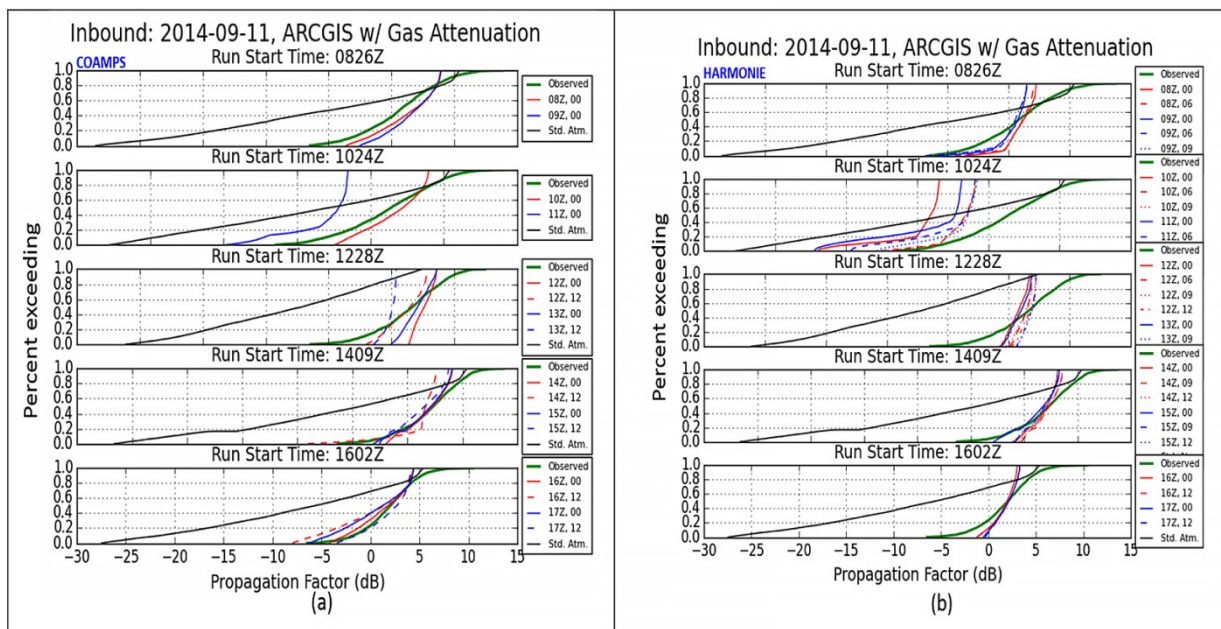

Figure A-42. Cumulative distribution functions for 12 Sep 2014 observed and predicted propagation factor for all initialization times, and forecast times prior and following each FRISC inbound run, from (a) COAMPS and (b) HARMONIE.
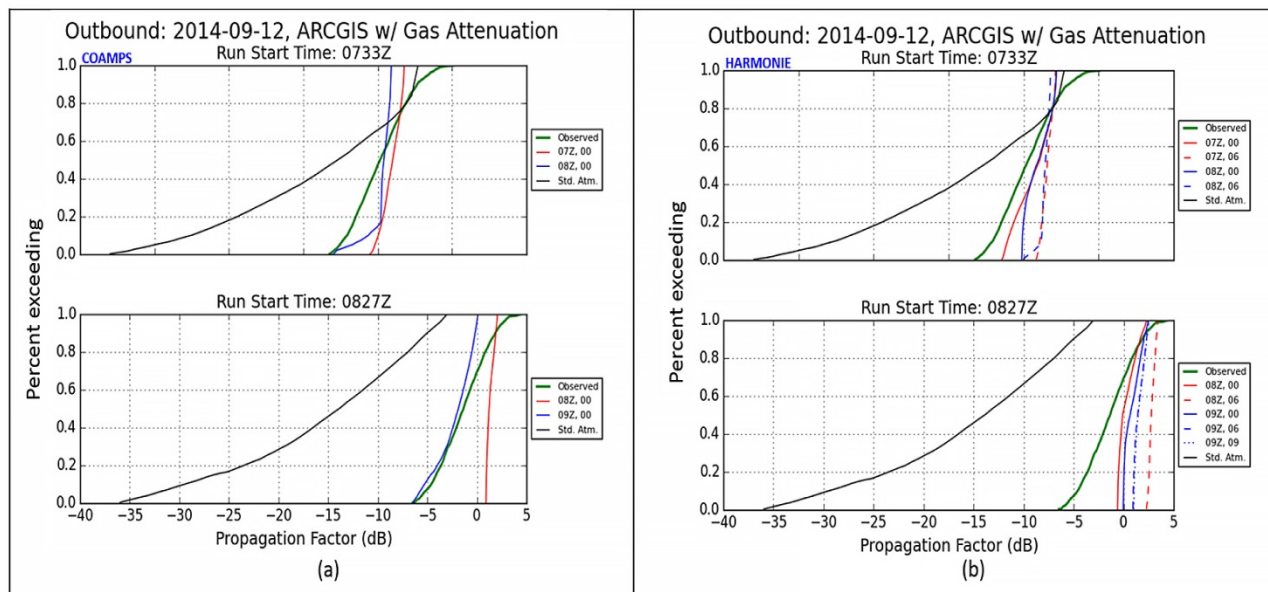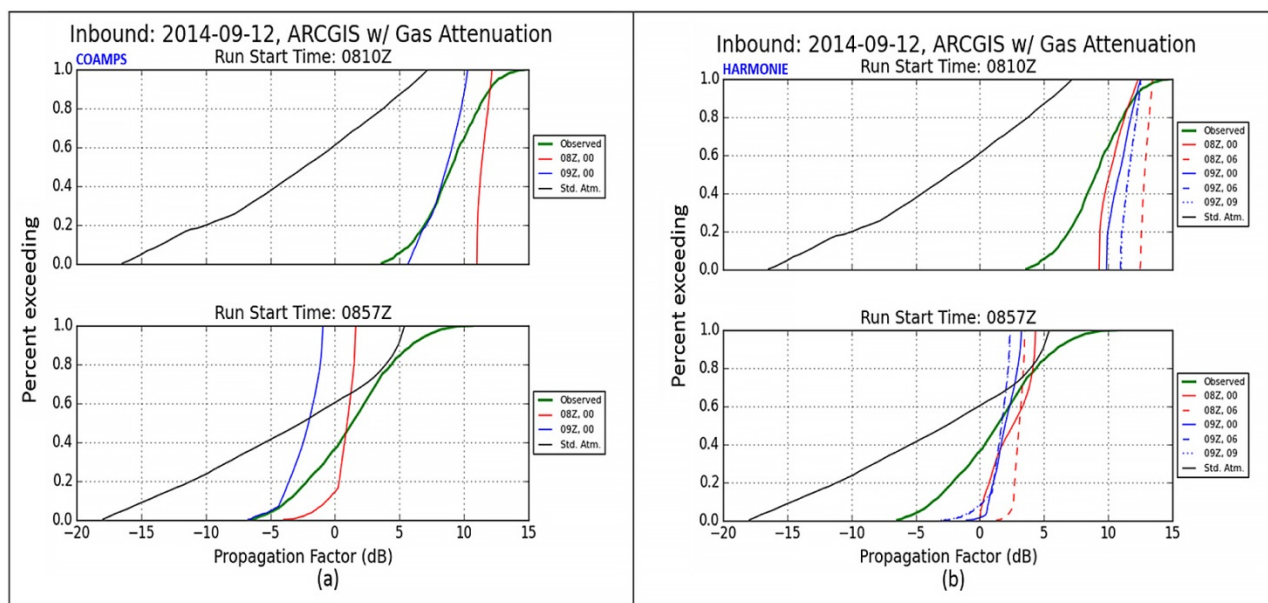
A.6 DETAILS A NWP FORECAST AND INITIALIZATION TIMES, PRIOR AND AFTER FRISC START TIMES

Table A-1 lists the NWP forecast and initialization times prior and after the FRISC start times. COAMPs and HARMONIE times are compared.

Table A-1. NWP forecast and initialization times used in Figures 71 to 74, immediately prior and after the FRISC start times.

Day	Start Time (UTC)	COAMPS Forecast / Initialization (UTC)		HARMONIE Forecast / Initialization (UTC)	
		Prior	After	Prior	After
9 Sep	1236	1200/1200,	1300 / 1200	1200 / 1200	1300 / 1200
	1342	1300/1200	1400 / 1200	1300 / 1200	1400 / 1200
	1411	1400/1200	1500 / 1200	1400 / 1200	1500 / 1200
	1500	1500/1200	1600 / 1200	1500 / 1200	1600 / 1200
10 Sep	0710	0700/0000	0800 / 0000	0700 / 0600	0800 / 0600
	0812	0800/0000	0900 / 0000	0800 / 0600	0900 / 0900
	0922	0900/0000	1000 / 0000	0900 / 0900	1000 / 0900
	1017	1000/0000	1100 / 0000	1000 / 0900	1100 / 0900
	1118	1100/0000	1200 / 1200	1100 / 0900	1200 / 1200
	1212	1200/1200	1300 / 1200	1200 / 1200	1300 / 1200
	1320	1300/1200	1400 / 1200	1300 / 1200	1400 / 1200
	1412	1400/1200	1500 / 1200	1400 / 1200	1500 / 1200
11 Sep	0727	0700/0000	0800 / 0000	0700 / 0600	0800 / 0600
	0826	0800/0000	0900 / 0000	0800 / 0600	0900 / 0900
	0924	0900/0000	1000 / 0000	0900 / 0900	1000 / 0900
	1024	1000/0000	1100 / 0000	1000 / 0900	1100 / 0900
	1133	1100/0000	1200 / 1200	1100 / 0900	1200 / 1200
	1228	1200/1200	1300 / 1200	1200 / 1200	1300 / 1200
	1325	1300/1200	1400 / 1200	1300 / 1200	1400 / 1200
	1409	1400/1200	1500 / 1200	1400 / 1200	1500 / 1200
	1516	1500/1200	1600 / 1200	1500 / 1200	1600 / 1200
	1602	1600/1200	1700 / 1200	1600 / 1200	1700 / 1200
12 Sep	0733	0700/0000	0800 / 0000	0700 / 0600	0800 / 0600
	0810	0800/0000	0900 / 0000	0800 / 0600	0900 / 0900
	0827	0900/0000	1000 / 0000	0800 / 0600	0900 / 0900
	0857	0800/0000	0900 / 0000	0800 / 0600	0900 / 0900

REPORT DOCUMENTATION PAGE

1. REPORT DATE *(DD-MM-YYYY)*	2. REPORT TYPE	3. DATES COVERED *(From - To)*
September 2016	Final	

4. TITLE AND SUBTITLE

Radio Frequency Performance Prediction in the North Sea
Analysis of the U.S.-NL Phase 1 Campaign

5a. CONTRACT NUMBER

5b. GRANT NUMBER

5c. PROGRAM ELEMENT NUMBER

6. AUTHORS

Amalia Barrios   Katherine Horgan   Vincent Van Leijen
Ted Rogers   Victor Wiss   Tjarda Wilbrink
Rick Navarro   Stephanie Billingsley   **DMO**
SSC Pacific   **NSWC Dahlgren Division**

Fok Bolderheij
Earl Williams   Robert Marshall   Joris Derksen
SSC Atlantic   **Mt. Pleasant Metrology**   **NDL**

5d. PROJECT NUMBER

5e. TASK NUMBER

5f. WORK UNIT NUMBER

7. PERFORMING ORGANIZATION NAME(S) AND ADDRESS(ES)

SSC Pacific
53560 Hull Street
San Diego, CA 92152–5001

8. PERFORMING ORGANIZATION REPORT NUMBER

TR 3028

9. SPONSORING/MONITORING AGENCY NAME(S) AND ADDRESS(ES)

SPAWAR   Office of the Secretary of Defense   Netherlands Ministry of Defense
PEO C4I/PMW 120)   The Pentagon   Plein 44
4303 Pacific Hwy   2 N. Rotary Road   2511 CR The Hague
San Diego, CA 92110   Arlington, VA 22202   The Netherlands

10. SPONSOR/MONITOR'S ACRONYM(S)
PEO C4I/PMW-120; OSD; Netherlands MOD

11. SPONSOR/MONITOR'S REPORT NUMBER(S)

12. DISTRIBUTION/AVAILABILITY STATEMENT
Approved for public release.

13. SUPPLEMENTARY NOTES

14. ABSTRACT

This report presents a summary of the technical analysis of meteorological and radio-frequency (RF) propagation data collected during the Phase 1 field trial conducted as part of a joint U.S.-Netherlands (NL) project of the Coalition Warfare Program (CWP). The CWP effort is jointly funded by the U.S. (PEO C4I/PMW-120 and the Office of the Secretary of Defense (OSD)) and the Netherlands Ministry of Defense (MoD). The objective of the CWP effort is to enhance radar modeling to enable improved situational awareness of the detection capability of phased array radars, as affected by current meteorological and oceanographic (METOC) conditions.

15. SUBJECT TERMS
meteorological; radio frequency; radar modeling; phased array radars; COAMPS; HARMONIE surface layer forecasts; high-resolution limited area model; cumulative distribution function; advanced phased array radar; cumulative distribution function; effective radiated power; fast raiding interceptor; special forces craft; global data assimilation system; electronic warfare

16. SECURITY CLASSIFICATION OF:			17. LIMITATION OF ABSTRACT	18. NUMBER OF PAGES	19a. NAME OF RESPONSIBLE PERSON
a. REPORT	b. ABSTRACT	c. THIS PAGE			Amalia Barrios
U	U	U	U	131	19B. TELEPHONE NUMBER *(Include area code)* (619)-553-1429

INITIAL DISTRIBUTION

SSC Pacific
San Diego, CA 92152-5001